The Audible Human Project: Geometric and Acoustic Modeling in The Airways, Lungs and Torso

BY

BRIAN HENRY

B.S. University of Illinois at Chicago, Chicago, IL, 2011

THESIS

Submitted as partial fulfillment of the requirements

for the degree of Doctor of Philosophy in Bioengineering

in the Graduate College of

the University of Illinois at Chicago, 2018

Chicago, Illinois

Defense Committee

Dr. Thomas Royston, Chair and Advisor

Dr. Dieter Klatt

Dr. Christian Luciano

Dr. Robert Molokie, Medicine

Dr. Hansen Mansy, University of Central Florida

DEDICATION

To my family, friends, and birds for the unwavering support and encouragement over the years.

ACKNOWLEDGEMENTS

I would first and foremost like to thank Dr. Royston, for his support and guidance as I started, progressed and am ultimately finishing in this research.

I would also like to thank the members of my graduate committee, Dr. Mansy, Dr. Klatt, Dr. Luciano and Dr. Molokie, as well as Dr. Magin and Dr. Valdez-Jasso for their support during my preliminary examination. The financial aid given by the National Institute of Health (Grant No. EB012142) is also acknowledged.

I would also like to thank Cierra Hall, for her support throughout my graduate studies, without which I would not have finished.

I would finally like to express my thanks to my colleagues in the Acoustics and Vibrations Laboratory, specifically Ying Peng and Zoujun Dai, who worked on the Audible Human Project alongside me. I would also like to thank my other lab colleagues, specifically Altaf Khan, Temel Yasar, Yifei Liu and Harish Palnitkar for their support and guidance. Last, but not least, I would also like to thank my family for the encouragement throughout this endeavor.

BRIAN HENRY

TABLE OF CONTENTS

LIST OF TABLES

LIST OF FIGURES

SUMMARY

The Audible Human Project (AHP) is a long-standing project at the Acoustics and Vibrations Laboratory with the aim to develop a series of acoustic models that can accurately measure sound generation, transmission and noninvasive measurement. The focus of the AHP has been in the pulmonary system. The basis of this dissertation is built as an extension of previous work dedicated to the analysis of tissue viscoelasticity and thoracic cavity acoustic models with simple airway structures. The goals of this dissertation, in line with the scope of the AHP, are to develop a better understanding of sound propagation in the lungs and airways, using improved analytical and numerical methods.

This dissertation is directed along the following research objectives: (1) expand on the current 1D waveguide used to model sound propagation in an airway tree so that full conducting airway models can be mapped acoustically; (2) further expand on the 1D waveguide so that breathsound analysis in small airways can be modeled; (3) develop more nuanced numerical techniques through boundary element analysis to model responses on the surface of the lung based on 1D waveguide input, and adopt sound localization strategies to predict sound source locations; and (4) develop improved visualization technologies for big acoustic data and expand the current set of case studies to include animal subjects.

1D Waveguide Analysis. A methodology to develop complex human 3D conducting airway trees is proposed, along with improvements to the 1D waveguide to address limitations in the current 1D waveguide algorithm. The hybrid segmentation method is adopted to generate airway trees based on a combination of image segmentation and algorithmic airway generation. The modified 1D waveguide is then applied to a full conducting 3D airway model to model sound propagation in a tracheal insonification model with healthy and pathologic states. Expanding the 1D waveguide allowed for acoustic mapping of complex 3D conducting airway models generated algorithmically, and was validated numerically and experimentally. Quantitative differences in

acoustic radial velocities in the 3D conducting airway tree were established in healthy versus pathologic models.

Breathsound Analysis. Pathophysiology of several adventitious breathsounds are explained and developed for analysis. Pulmonary models for crackles and wheezes are developed using geometrical, material and boundary condition changes to establish physiological relevance to pathology. The 1D waveguide is further developed to accommodate analytical analysis of models of wheezes. Time-history reconstruction of the acoustic pulse is then achieved through use of impulse response functions to develop sound localization strategies for crackles. The 1D waveguide expansion allows for acoustic mapping of a complex human 3D conducting airway tree with more options for sound source placement, which can be determined based on the mechanism and location of generated adventitious sounds. Quantitative differences in acoustic radial velocities of airway segments of healthy versus pathologic cases are established.

Boundary Element, Incident Field and Source Localization. Numerical algorithms using boundary element analysis are adopted to model acoustic velocities on the lung surface as a result of monopole sources approximating the breath sound field with geometric placement determined through generated 3D conducting airway geometries and acoustic strengths determined using the 1D waveguide. Cases are established for insonification and breathsound models with healthy and pathologic states. Source localization strategies are then performed based on boundary element analysis to predict acoustic source locations. Acoustic predictions were performed in silico based on sensor placement per boundary element centroid in the lung models, as well as using reduced sensor placements to predict acoustic sources with more clinically realistic sensor numbers. Sound localization strategies for boundary element analysis proved to be more time consuming, but predicted the acoustic source more accurately compared to incident field analysis, both in full sensor and reduced sensor grids.

CHAPTER 1

INTRODUCTION

1.1 BACKGROUND AND MOTIVATION

The lungs are a unique organ, with an inhomogeneous multiphase and multiscale structure. Like any other organ in the human body, the lungs exhibit macroscopic properties that can be quantified to be indicative of disease, but due to the lungs structure medical imaging technologies have had difficulty contrasting these pathophysiologic and structural changes. Multiple pulmonary pathologies, such as inflammation, pulmonary fibrosis or lung consolidation, are resultant in significant changes in material properties, including lung stiffness, density and viscosity, over localized or over large regions of the lung volume. However, these pathological conditions can be difficult to diagnose using current imaging technology.

Creating an acoustic map of the thoracic region will allow for possible acoustic diagnosis of multiple pathologies. Moreover, knowledge of how the material properties of the body changes over the course of a disease can lead to acoustic analysis that can not only determine disease severity, but also location through acoustic source localization algorithms. One mode of dynamic elastography, magnetic resonance elastography (MRE), is capable of noninvasive 3D mapping of material properties via image processing of shear wave motion. It is difficult to apply MRE in the lung region because of the inhomogeneity of lung structure: low proton count due to the high air and low tissue volume. Better interpretation of MRE processing therefore can be done by further investigation of pulmonary (lung and airway) sound propagation.

Under the Audible Human Project (AHP), a series of vibroacoustic studies involving airway insonification and percussion thoracic models have been created to model sound propagation in the thoracic cavity, with their results available [1, 2, 3, 4]. Relatively less attention however has been given to the airways since development of a robust airway tree down to alveolar diameters is nontrivial.

1.2 LITERATURE REVIEW

Lung Physiology and Function. The lungs and airways provide an important function in the human body: oxygen transportation into the body and carbon dioxide release. This is accomplished by a series of inter-organ actions, from the diaphragm shrinking, causing the lungs to expand and take in air, to the diaphragm expanding, causing the lungs to retract. As oxygen is taken into the lungs, it is funneled throughout an airway structure before it is absorbed into the body and exchanged for carbon dioxide: it first passes through gas conducting airway segments, where the air is conducted from the trachea into the voluminous expanse of the lung, and finally through the gas exchange segments, where the gas exchange happens. In addition, the alveoli in the gas exchange segments act as a filter to remove pathogens and dust, as well as maintain proper heat and humidity to keep the lungs in perfect condition. The airways are a site of immune defense in the body, as well as a medium of gas exchange. The lungs and airways in this aspect are unique in the body; no other human organ has such a large amount of inhomogeneity in terms of composition, and because of the vast airway network which provide an efficient means of introducing and conducting sound, is of great interest acoustically.

To provide a maximum surface area for gas exchange, the airways are branched into a hierarchical branching structure. The conducting airways are tubular in nature, with an inner hollow diameter where gas is conducted and an outer diameter divided between cartilage and soft tissue, providing the airway network with a great amount of elasticity. The conducting airways include parent segments branching into two daughter segments that (typically) reduce in radial (inner and outer) diameter and length, in a manner that greatly increases surface area as the distance from the larger airways increases. As oxygen is conducted through the airways, the flow rate of the oxygen is further divided in parallel, slowing the speed and increasing the volume in the lung where it’s diffused, until the gas reaches the alveoli where gas transport is predominately driven by molecular diffusion. In this aspect, it can be concluded that the airways are multiscale

in origin, from centimeter internal diameters in the trachea to millimeter internal diameters in the terminal bronchioles finally to hundreds of micrometers in the alveoli, effectively spanning three orders of magnitude. As a result, airways have been very difficult to tackle experimentally from gas concentration measurements to medical imaging, without disturbing the normal function of the airways. To remedy this void in modern science, mathematical modeling has been applied on idealized and digitized lung and airway structures over the past few decades.

Lung, Airway and Pulmonary Acoustics Modeling. The modeling of sound transmission throughout the pulmonary system and chest region can be categorized into a system with three main components:

(1) Transmission of sound through the conducting airway tree, and

(2) Coupling of the acoustic waveguide theory of wave transmission through the conducting airway tree to the surrounding airway geometry, and

(3) Coupling of the airway acoustics to the lung parenchyma (which includes air in the case of a pneumothorax, or water and/or blood in the case of a hydro/hemothorax), the ribcage, sternum and scapula, and the torso body volume.

Historically, acoustic studies have been limited in terms of airway integration: the geometric complexity of the airways was difficult to capture accurately and model accordingly. This has limited the scope of the AHP's acoustic simulations where the airways played a major role in sound excitation (via insonification and breathsound) and lung geometric modeling, where the lung was viewed as a homogenous viscoelastic or poroviscoelastic material. In order to integrate a full conducting airway tree model into our acoustic studies, which include airways extending from the trachea to the terminal bronchioles, a hybrid method of airway segmentation and algorithmic generation was adopted in order to (1) capture a physiologically accurate base

airway tree structure, with patient specific relevance, and (2) extend the limits of the base airway tree to the limits of the conducting airways, which adhere to a quasi-fractal geometric structure.

There have been multiple methodologies proposed for generating airways [5, 6]. Two major divergent methodologies, developed by Dr. Hiroko Kitaoka and Dr. Merryn Tawhai, use a system of airway generation rules relating airway perfusion volume to optimal airway volume and fractal volume-splitting method, respectively. Dr. Kitaoka was able through use of a deterministic algorithm to develop a three-dimensional model of the human airways based on a power law relationship between airway diameter and flow. Dr. Tawhai's volume-splitting method focuses on filling a volume defined by a uniform grid of points, and generating new segments by extending a defined fractional distance towards a center of mass defined by a splitting plane, checking for branching angles, lengths, and volume inclusion. Historically, airway conducting models were developed using via the Airway Growth Algorithm (AGA), which was a combination of the Constrained Constructive Optimization (CCO) algorithm [7, 8, 9, 10] and adaptation of Dr. Kitaoka's power law method. The algorithm used in this dissertation to grow conducting airway trees is an adaptation of Dr. Tawhai's volume-splitting method after validation of increased downstream geometric property accuracy (segment length, radii and bifurcation angles) [11] and decreased algorithm runtime.

In addition, this dissertation introduces a slightly modified method of calculating the acoustic properties for a complex 3D conducting airway tree, without the need for a self-consistent Horsfield model [12, 13]. We introduce a modified set of acoustic equations via Henry et al [14, 15, 16, 17] that relies on parent/daughter relationships, instead of Horsfield order number and delta relationships. Studies have proven that the calculations provide an identical acoustic map over all measured frequencies, and that the new method produces identical results in a published ecoflex model [1].

While there have been many vibroacoustic studies conducted on thoracic models [2, 3, 4], airway specific diseases have received less attention because of the difficulty in creating models complex enough to capture airway complexity down to the alveolar level. MRI and CT resolution cannot capture bronchiole to alveolar segments accurately because of the limits on resolution, which limits accurate segmentation to several airway generations. Conducting tree algorithmic generation on an anatomically accurate base structure then allows for an anatomically relevant continuation of the airway tree down to the bronchiole level. With the creation of these anatomically consistent models, a sufficiently robust airway tree was created to perform analytical and numerical studies on healthy versus pathologic states.

Lung and Airway Viscoelasticity. The lungs are a highly viscoelastic organ exhibiting creep and stress relaxation phenomenon in response to bodily stimuli. Due to lung viscoelasticity, the lungs also exhibit frequency specific changes in elastic parameters. There have been many studies done to measure these frequency dependent parameters using various auscultation measures [18, 19, 20, 21, 22] along with other mathematical modeling to model sound propagation and attenuation in a cylindrical medium [23]. While the lung compression wave speed doesn't change significantly with frequency, the shear wave speed and attenuation change according to frequency because of lung viscoelasticity. As an example, comparing muscle with fat, the X-ray attenuation coefficient doubles [24] while MR relaxation times triple [25]. However, the shear moduli can change more than a factor of ten, which is useful because of the much higher distinguished contrast in medical imaging [26, 27, 28]. As a result, it is of interest to characterize the lung viscoelastic properties. Improving our understanding of lung surface (Rayleigh) wave motion can assist in understand lung shear viscoelastic properties. In addition, alterations in soft tissue function, whether it is a result of natural or pathological reasons, can alter shear wave behavior (phase speed and attenuation rate) [29, 30, 31].

A range of rheological models have been used in previous studies to aid in interpreting shear and surface wave measurements. These models do so by modeling soft tissue viscoelasticity as a system of its elastic and damping components, both of which are frequency dependent. A Voigt model was used commonplace historically, but more recently Voigt models have been shown to have limitations in their ability to capture a systems elasticity and damping accurately over wide time scales and/or with large frequency ranges. These discrepancies are more pronounced in biological tissues and phantoms with tissue mimicking materials. As a result, other rheological models have been used [32, 33, 34, 35, 36]. Fractional order viscoelastic models, such as the fractional Voigt model, have shown much greater accuracy, and thus have a greater potential to aid in more advanced medical diagnostics with tissues with viscoelastic properties, especialy with pathologies that over time exhibit changes in viscoelastic properties such as liver cirrhosis and breast cancer.

1.3 RESEARCH OBJECTIVE

The long-term goal of the AHP is to develop a complex acoustic simulation capable of accurately modeling acoustic generation and transmission throughout a coupled thoracic cavity model including a full model of the conducting airways. These acoustic simulations will include noninvasive measurement of sound and vibration caused by both external (e.g. percussion) and internal (e.g. respiratory function) sources. In addition, these models have wide potential uses in enhanced medical education and training, and can possibly aid in more advanced diagnostic techniques. The goals of this dissertation research are to combine the earlier efforts in lung viscoelastic modeling and pulmonary acoustic simulations with airway waveguide techniques, with the aim to develop an integrated thoracic cavity pulmonary model including a complex airway tree, in order to capture airways specific contributions to the acoustic profile. To achieve these goals, the following **specific aims** are undertaken:

1. Develop/adapt a means of building a full conducting airway tree model, and modify the previous 1D waveguide mathematical model to accurately model wave transmission;

2. Develop a modified mathematical model via the 1D waveguide to model breathsounds via pathological airway conditions;
3. Improve existing Boundary Element (BE) and Incident Field (IF) algorithms to integrate modified 1D waveguide models in a thoracic cavity model;
4. Expand waveguide studies to porcine and other animal subjects, and develop advanced visualization techniques for viewing complex big acoustic data.

1.4 DISSERTATION OVERVIEW

In this dissertation, the research background, motivation and objectives are presented in Chapter 1. This includes a summary of the current state of the art in pulmonary modeling research and related topics. The four aims presented in section 1.3 are presented in Chapters 2-5. Chapter 2 focuses on improved airway physiological and acoustic mathematical modeling, to calculate an acoustic profile of a physiologically relevant 3D conducting airway structure. This is then expanded to include non-trachea acoustic sources to model airway-specific pathologies, including wavefront time-history reconstruction in Chapter 3. The generated airways are then integrated into a full thoracic cavity model, including volumes for the ribcage, scapula and torso. Simulations are carried out via non-coupled Boundary Element (BE) between several healthy and pathological states in Chapter 4. An acoustic detection is performed in Chapter 4 in an attempt to localize acoustic sources based on surface velocity measurements produced via BE simulation. In Chapter 5 other animal studies are provided, in addition to improved visualization methodologies for visualizing complex acoustic profile data. Chapter 6 summarizes the accomplishments in this dissertation, and provides further topics for consideration and research.

REFERENCES

[1] Z. Dai, Y. Peng, H. Mansy and T. Royston, "Comparison of Poroviscoelastic Models for Sound and Vibration in the Lungs," *J. Vib. Acoust.,* vol. 136, pp. 051012-1 - 051012-11, 2014.

[2] Z. Dai, H. Mansy, R. Balk and T. Royston, "Sound transmission in the chest under surface excitation: an experimental and computational study with diagnostic applications," *Med. Biol. Eng. Comput.,* vol. 52, pp. 695-706, 2014.

[3] Z. Dai, Y. Peng, B. Henry, H. Mansy, R. Sandler and T. Royston, "A comprehensive computational model of sound transmission through the porcine lung," *J. Acoust. Soc. Am.,* vol. 136, pp. 1419-1429, 2014.

[4] H. Mansy, R. Balk, W. Warren, T. Royston, Z. Dai, Y. Peng and R. Sandler, "Pneumothorax effects on pulmonary acoustic transmission," *J. Appl. Physiol.,* vol. 119, pp. 250-257, 2015.

[5] H. Kitaoka, Takaki R and B. Suki, "A three-dimensional model of the human airway tree," *J. Appl. Physiol.,* vol. 87, pp. 2207-2217, 1999.

[6] M. Tawhai, A. Pullan and P. Hunter, "Generation of an anatomically based three-dimensional model of the conducting airways," *Annals of Biomed. Eng.,* vol. 24, pp. 793-802, 2000.

[7] W. Schreiner , M. Neumann and F. Neumann, "The Branching Angles in computer-generated Optimized Models of Arterial Trees," *J. Gen. Physiol.,* vol. 103, pp. 975-989, 1994.

[8] W. Schreiner, F. Neumann and M. Neumann, "Structural Quantification and Bifurcation Symmetry in Arterial Tree Models generated by Constrained Constructive Optimization," *J. Theor. Biol.,* vol. 180, pp. 161-174, 1995.

[9] W. Schreiner, "Computer generation of complex arterial tree models," *J. Biomed. Eng.,* vol. 15, pp. 148-150, 1992.

[10] R. Karch, F. Neumann, M. Neumann and W. Schreiner, "A three-dimensnional model for arterial tree representation, generated by Constrained Constructive Optimization," *Comp. Biol. Med.,* vol. 29, pp. 19-38, 1998.

[11] M. Tawhai, P. Hunter, J. Tschirren, J. Reinhardt, G. McLennan and E. Hoffman, "CT-based geometry analysis and finite element models of the human and ovine bronchial tree," *J. Appl. Physiol.,* vol. 97, no. 6, pp. 2310-2321, 2004.

[12] K. Horsfield and G. Cumming, "Morphology of the bronchial tree in man," *J. Appl. Physiol.,* vol. 52, pp. 373-83, 1968.

[13] K. Horsfield, W. Kemp and S. Phillips, "An asymmetrical model of the airway of the dog lung," *J. Appl. Physiol.,* vol. 52, pp. 21-26, 1982.

[14] B. Henry and T. Royston, "A multiscale analytical model of bronchial airway acoustics," *J. Acoust. Soc. Am.,* vol. 142, no. 4, pp. 1774-1783, 2017.

[15] R. Habib, R. Chalker, B. Suki and A. Jackson, "Airway geometry and wall mechanical properties estimated from subglottal input impedance in humans," *J. Appl. Physiol.,* vol. 77, pp. 441-51, 1994.

[16] R. Habib, B. Suki, J. Bates and A. Jackson, "Serial distribution of airway mechanical properties in dogs: effects of histamine," *J. Appl. Physiol.,* vol. 77, pp. 554-566, 1994.

[17] A. Benade, "On the propagation of sound waves in a cylindrical conduit," *J. Acoust. Soc. Am.,* vol. 44, pp. 616-623, 1968.

[18] H. Pasterkamp, R. Consunji-Araneta, Y. Oh and J. Holbrow, "Chest surface mapping of lung sounds during methacholine challenge," *Pediatric Pulmonology,* vol. 23, pp. 21-30, 1997.

[19] G. Benedetto, F. Dalmasso and R. Spagnolo, "Surface distribution of crackling sounds," *IEEE Trans. Biomed. Eng.,* vol. 35, pp. 406-412, 1988.

[20] S. Charelston-Villalobos, S. Cortes-Rubiano and R. Gonzalez-Camarena, "Respiratory acoustic thoracic imaging (RATHI): assessing deterministic interpolation techniques," *Med. & Biol. Eng. & Comput.,* vol. 42, pp. 618-626, 2004.

[21] T. Bergstresser, D. Ofengeim, A. Vyshedskiy, J. Shane and R. Murphy, "Sound transmission in the lung as a function of lung volume," *J. Appl. Physiol.,* vol. 93, pp. 667-674, 2002.

[22] R. Paciej, A. Vyshedskiy, J. Shane and R. Murphy, "Transpulmonary speed of sound input into the supraclavicular space," *J. Appl. Physiol.,* vol. 94, pp. 604-611, 2003.

[23] M. Kompis, H. Pasterkamp and G. Wodicka, "Acoustic imaging of the human chest," *Chest,* vol. 120, pp. 1309-1321, 2001.

[24] F. Duck, Physical properties of tissue: a comprehensive reference book, NY: Academic Press, New York, 1990.

[25] V. Kuperman, Magnetic resonance imaging: physical principles and applications, NY: Academic Press, New York, 2000.

[26] K. Hoyt, T. Kneezel, B. Castaneda and K. Parker, "Quantitative sonoelastography for the in vivo assessment of skeletal muscle viscoelasticity," *Phys. Med. Biol.,* vol. 53, pp. 4063-4080, 2008.

[27] Y. Fung, Biomechanics: mechanical properties of living tissues, NY: 2nd Ed., Springer-Verlag, New York, 1993.

[28] A. Saravazyan, O. Rudenko, S. Swanson, J. Fowlkes and S. Emelianov, "Shear wave elasticity imaging: a new ultrasonic technology of medical diagnostics," *Ultrasound in Med. & Biol.,* vol. 24, pp. 1419-1453, 1998.

[29] Y. Yamakoshi, J. Sato and T. Sato, "Ultrasonic imaging of itnernal vibration of soft tissue under forced vibration," *IEEE Trans. Ultrason. Ferroelectr. Freq. Contr.,* vol. 37, pp. 45-53, 1990.

[30] R. Muthupillai, D. Lomas, P. Rossman, J. Greenleaf, A. Manduca and R. Ehman, "Magnetic resonance elastography by direct visualization of propagating acoustic strain waves," *Science,* vol. 269, pp. 1854-1857, 1995.

[31] X. Zhang and J. Greenleaf, "Estiamtion of tissue's elasticity with surface wave speed," *J. Acoust. Soc. Am.,* vol. 2007, pp. 2522-2525, 2007.

[32] R. Chan and I. Titze, "Effect of postmortem changes and freezing on the viscoelastic properties of vocal fold tissues," *Ann. Biomed. Eng.,* vol. 31, pp. 482-491, 2003.

[33] D. Craiem and R. Armentano, "A fractional derivative model to describe arterial viscoelasticity," *Biorheol.,* vol. 44, pp. 251-263, 2007.

[34] M. Kiss, T. Varghese and T. Hall, "Viscoelastic characterization of in vitro canine tissue," *Phys. Med. Biol.,* vol. 49, pp. 4207-4218, 2004.

[35] D. Klatt, U. Hamhaber, P. Asbach, J. Braun and I. Sack, "Noninvasive assessment of the rheological behavior of human organs using multigrequency MR elastogrpahy: a study of brain and liver viscoelasticity," *Phys. Med. Biol.,* vol. 52, pp. 7281-7294, 2007.

[36] K. Riek, D. Klatt, H. Nuzha, S. Mueller, U. Neumann, I. Sack and J. Braun, "Wide-range dynamic magnetic resonance elastography," *J. Biomech. Eng.,* vol. 44, pp. 1380-1386, 2011.

CHAPTER 2

AIRWAY PHYSIOLOGY, GEOMETRY AND ACOUSTICS

2.1 INTRODUCTION

Like most other soft tissue, the lungs exhibit stress relaxation, creep and hysteresis, giving it both elastic and viscous linear and nonlinear properties. As sound in the airways propagates away from a source, the sound will cause the airway walls to expand and contract according to the lungs viscoelastic properties. There have been a multitude of non-invasive diagnostic [1-3] and therapeutic tools [4] that exist based on this acoustic theory of energy propagation and dispersion, creating motion that can be detected and measured noninvasively using contact (stethoscope) or non-contacting (optical) methods. More recently, with the emergence and marriage of elastography and MRI imaging, a new MRI modality called Magnetic Resonance Elastography (MRE) can visualize oscillatory motion initiated from sound sources noninvasively [5, 6] , giving rise to new experimental methodologies to measure internal motion without the need for biopsy or invasive techniques. However, due to the inhomogeneity in lung structure, measuring motion in the lungs via MRE has proven to be difficult.

While experimental methods have proven to have a varying degree of success in measuring internal sound propagation, numerical simulation of the thoracic region [7-10] is computationally expensive, and integration of an airway tree historically has been limited to simple subglottal model [11, 12]. In addition, many airway diseases are small-airway specific (wheeze, ronchi), meaning that a full thoracic FE simulation can miss important details in the acoustic map of the airway region. In terms of modeling of the human airways, segmentation is limited by the quality of the MRI/CT images and resolution of the machine. Bronchiole to alveolar sized airways cannot be accurately segmented, if seen at all, on current imaging modalities. In order to create a sufficiently detailed acoustic model of the airways, you need to first capture a detailed airway tree that is (1) reasonably physiologically relevant, and (2) can be married together with a

mathematical model of wave propagation that includes all the phenomena of gas and airway wall viscoelasticity considered to be significant. To remedy this, a hybrid airway generation method was adapted and put to use on a constructed segmentation model based on Dr. Tawhai's quasi volume-halving fractal algorithm [13, 14]. Using a segmentation model ensures that patient-specific geometry up to the limit of the resolution of the MRI/CT image is preserved, and algorithmically generated segments filling the rest of the conducting tree provides a means of developing anatomically relevant airway vessels beyond the resolution of the MRI/CT image.

Developing a sufficiently detailed airway structure provides a geometrical backbone to accompany a mathematical model that can describe wave propagation. Analytical models of acoustic propagation in the conducting airway tree are created by attributing a 1D waveguide onto a geometrical backbone. Historically, the waveguide was limited to Horsfield models [1, 15, 16], the geometry described as an idealized subglottal airway geometry. While the Horsfield model provides an efficient way of ordering the airways, there are limitations on the accuracy of the mathematical modeling: the models are 2D and contain a self-consistent structure between order number and geometrical properties. Dai et al. [15] built on the 1D waveguide, producing an efficient analytical approach to acoustically mapping a simple airway structure insonified through a tracheal segment, comparing the map versus a FE model and a simple ecoflex phantom with comparable geometry for validation. More recently, the 1D waveguide has been expanded to include 3D models and non-Horsfield compliant geometries [18], enabling fast and efficient acoustical mapping of conducting airway trees produced in a hybrid segmentation approach.

Pulmonary fibrosis (PF) causes global stiffening of the lung parenchyma and by relation the airway walls. PF is a secondary chronic effect of several possible conditions including cystic fibrosis or exposure to sources of radiation or environmental hazards. Because of the invasive nature of diagnosis, PF has a poor prognosis. PF is also often idiopathic [28, 29]. The prevalence of PF in the US in 2000 was recorded at 132,000 people, with the possibility of it being even higher

due to under or misdiagnosis. The incidence of idiopathic PF increasing dramatically with the age of the patient (most patients diagnosed are in their forties or fifties). Evidence indicates a direct relationship between the lung's parenchyma regional mechanical properties and disease progression and stage of PF [29]. As the current means of diagnosing idiopathic PF involves a dangerous invasive biopsy procedure, a noninvasive means of assessing regional stiffness via acoustic means gives possibilities to new and improved diagnosis methods, including means of calculating directly with spatially resolved intrinsic mechanical properties of the lung parenchyma such as lung resistance, compliance and hysteresis. Such noninvasive and reproducible means of quantifying and qualifying lung parenchyma fibrosis could lead to improved evaluation and management of patients suffering from PF and other interstitial lung diseases. Moreover, 1D waveguide analytical analysis can be paired with another emerging medical imaging technology: magnetic resonance elastography (MRE) to add airway-specific elastographic details where conventional elastography lacks the means to image small airways accurately [5, 6]. Pairing 1D waveguide analytical models, which also incorporate patient-specificity, can also aid in the qualification of ultrasonic or noninvasive hyperpolarized gas MRE methods, which do have sufficient sensitivity down to the micron level needed to quantify smaller conducting and gas exchange airway health deterioration caused by PF.

Bronchoconstriction can be classified as a narrowing of the airways in the lower conducting and gas exchange airways, and may result from a spasmodic state of the airway soft tissue wall muscles. Bronchoconstriction can also result from inflammation of the airway soft tissue middle layers, excessive mucus along the airway walls in the lumen or inflammation via obstructive diseases (asthma or emphysema). 1 in 13 Americans have asthma, making it one of the most expensive health conditions in the US [30]. However, despite its high prevalence the pathogenesis of asthma is not fully understood, in part due to partial symptom quantifiability (airways smaller than 2mm suffer inflammatory bronchoconstrictive responses). During bronchoconstriction, the

airway walls thicken, causing the inner diameter of airways to shrink, and mucous made up of glycoproteins plug and clog the airways, which in turn gives rise to adventitious breathsounds such as severe wheezing which can be potentially deadly. Understanding how bronchoconstriction affects sound propagation and generation may lead to an improved understanding of bronchoconstriction disease stages and progression.

Pulmonary infiltrate is classified as an obstructive airway pathology, commonly affecting the smaller airways by occluding airways and reducing lung capacity. Pulmonary infiltrate affects 50 million people worldwide [31]. Like many lung pathologies, it shares common symptoms and can stem from other lung pathologies, such as acute chest syndrome (ACS), and is a leading cause of death for people with sickle cell disease (SCD). Additionally, about half of patients with SCD will have one or more episodes of ACS during their lifetime. Typically, it is localized to one or a few lung lobes. Using auscultative techniques, acoustic crepitations are used as an indicator for ACS and severe wheezing episodes are a potential marker for the disease progression. In addition, lung consolidation can be detected for patients of SCD and AVS via acoustic means through increased sound coupling with the airway wall [32]. Thoracic acoustic measurements can be altered during ACS, which can provide a quantitative backbone to providing a means to detect onset earlier.

2.2 THEORY

2.2.1 MODELING AND STRUCTURING CONDUCTING AIRWAY TREES

The conducting trees used in this study were obtained from Miyakawi et al. [19], which were developed according to a hybrid segmentation approach involving image segmentation to develop an anatomically relevant airway skeleton model along with algorithmic generation of airway segments to fill in the conducting tree [20]. The conducting airway tree model consisted of about 60,000 segments, from a radius of 20mm for the trachea to a ~1mm average radius to the terminal bronchioles. Although the human geometry in this study was obtained from Ref. 19, the hybrid

segmentation method was adapted and utilized in other animal subjects, and can be seen later in Chapter 5 of this dissertation.

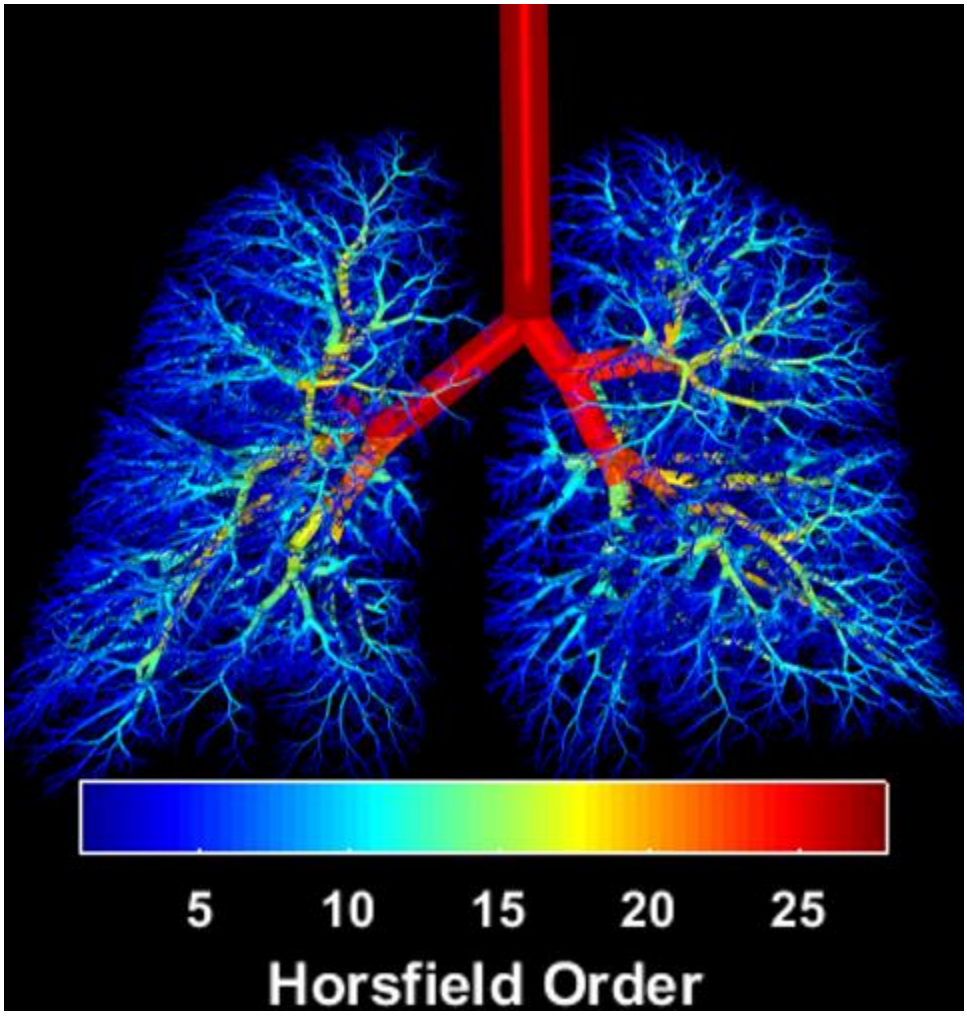

Figure 2.1. The conducting airway tree used in this study, colored by its approximate Horsfield order number.

The first step of the image segmentation process involves capturing the lung geometry. Segmentation of the lung volume was done via automatic CT imaging via Jahani et al. [21] on one of five healthy human subjects. The CT image output consisted of 13 different images at 13 timepoints within the respiratory cycle; in this study the lung geometry at total lung capacity (TLC) was used to develop the airway model. The CT image had the five lobes differentiated by contrast.

The lung was used as a host volume for algorithmic generation by subdividing the lung volume into a 3D grid. The volume of the lung (4.17 liters in this study, with the airways occupying 0.571 liters) was used in conjunction with the expected number of terminal segments (26,000 to 32,000) via Haefeli-Bleuer & Weibel [22]. 29,000 terminal segments were used as a midpoint number of terminal segments. Using this in conjunction with the lung volume yielded a mean respiratory unit of 124.1mm^{3,} providing a sensible estimate of the points for grid spacing. The segmented airways were obtained via skeletonization to yield a centerline airway tree with radii information parsed from the image.

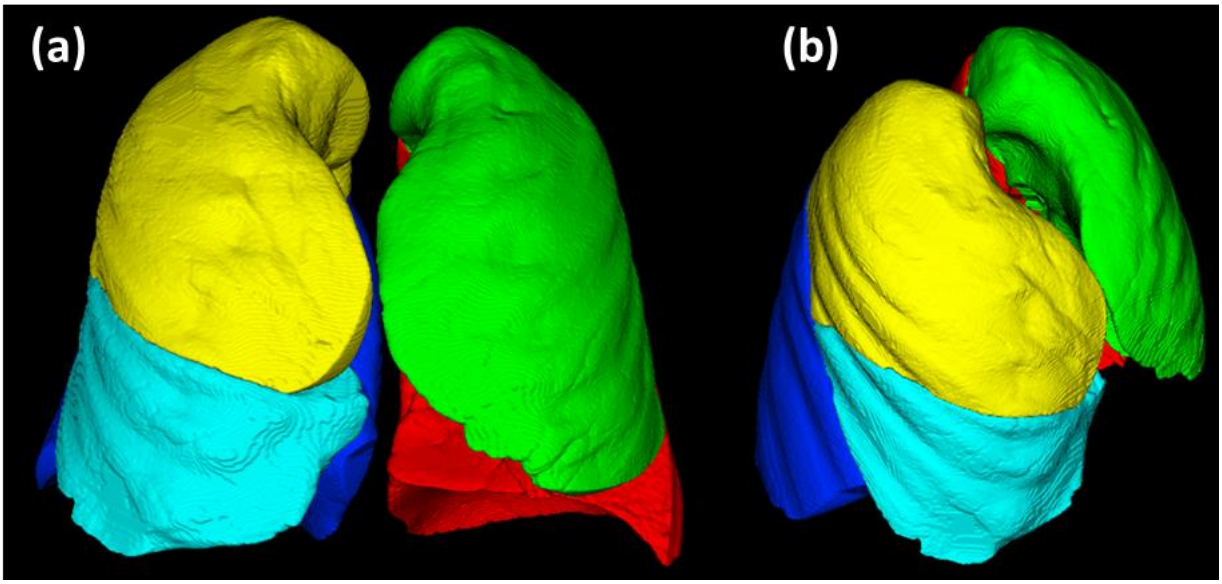

Figure 2.2. The lung volume used in this study, color differentiating each lobe. Color code: Yellow: right superior; light blue: right middle; dark blue: right inferior; green: left superior; red: left inferior. (a) shows a frontal view of the lungs (cranial pointing upwards posterior into the page), and (b) shows a isometric view of the lungs (cranial pointing upwards, anterior into the page).

The airway skeleton provides a conducting airway model with airway segments down to the limit of CT resolution. A volume halving algorithm via Tawhai et al. was then used to fill in the rest of the conducting tree model in a physiologically relevant manner. The volume-halving algorithm used was as a development of a 2D area halving algorithm developed by Wang et al. [23], aiming

to supply each grid point of a host area with a terminal branch. With the 3D adaptation, the algorithm halves volume with each iteration. The algorithm works in four main iterative stages: center of mass (COM) calculation, volume subdivision, subvolume COM calculation and segment generation. The full conducting trees can be ordered by Strahler order number or by an approximate Horsfield order number. The approximate Horsfield order number is assigned based on the parent segment radius and radii ratio between parent and daughter segments.

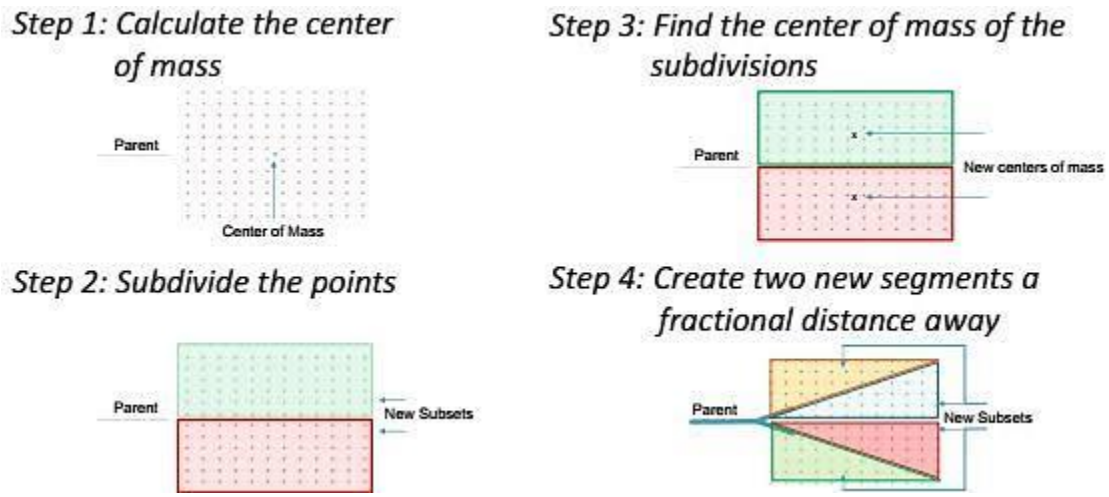

Figure 2.3. Depiction of the four step process in algorithmic generation.

This process starts with the terminal segments of the CT-generated centerline airway model as the parent segments. First, the lobe-differentiated volumes are divided according to each segment based on segment proximity (Fig 2.3, top left). Next, the volume is halved into subvolumes based on connection of the distal point of the parent segment to the COM of the volume: the volume is split along a dividing plane perpendicular to the branching plane created from the two points of the parent segment and the COM. Once the volume is divided into subvolumes, the COMs of the subvolumes is calculated, and from the distal point of the parent segment two branching segments are created by creating connections at a fractional distance to the COMs of the subvolumes. This fractional distance was calculated to be 0.4 using the method

described in Ref. 13 as it had the largest volume of generated airways compared to other fractional values from 0 to 1. In order to keep the airways physiologically relevant, there were other limits in terms of segment length, bifurcation angles and other geometrical properties via Ref. 13.

2.2.2 MODELING SOUND PROPAGATION IN A BIFURCATING AIRWAY NETWORK

Per the Horsfield model, the conducting airway tree is divided into 35 orders of consistent geometrical properties (length, radii, length, cartilage fraction, airway wall thickness and recursion index), with the trachea as order 35 and the terminal bronchioles as order 1, which themselves bifurcates into two alveoli each. The airways designed in this manner are a system of bifurcating tubes; the outer diameter describing the airway wall thickness and the inner diameter describing the hollow space used for air conduction. Conducting tree asymmetry comes from use of a recursion index (Δ): parent segments of order n will bifurcate into segments $n-1$ and $n-1-\Delta^{(n)}$. In this manner, the tree is self-consistent because for a given airway order n, the geometrical properties are consistent throughout the lung. These bronchial models were later modified by Habib [1, 17] to account for terminal respiratory tissue and non-rigid airway walls.

The 1D waveguide relies on this geometrical assumption as it calculated impedances and pressures. This self-consistency creates an incredibly efficient calculation: for 35 orders of airways, depending on the level of asymmetry, there can be around 6 million segments, but only 35 iterations of calculations need to be accounted for. This is accomplished by solving for the impedance of the terminal $n = 1$ segments, and then iteratively solving upward in the recursion ladder up to $n = 35$, the trachea.

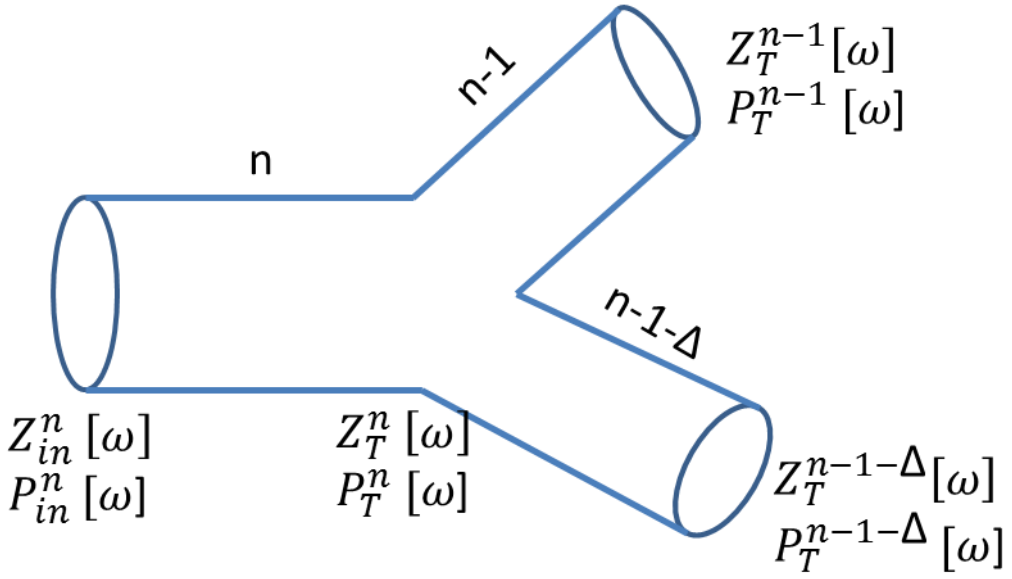

Figure 2.4. An airway model with a single bifurcation.

The terminal and input impedances, $Z_T^n[\omega]$ and $Z_{in}^n[\omega]$, are solved iteratively as follows:

$$Z_T^n[\omega] = \begin{cases} \dfrac{N_T}{j\omega C_g + 1/[R_t + j(\omega I_t - 1/[\omega C_t])]} & n=1 \\ \dfrac{1}{1/Z_T^{n-1}[\omega] + 1/Z_T^{n-1-\Delta}[\omega]} & otherwise \end{cases}, \quad (2.1)$$

$$Z_{in}^n[\omega] = \frac{Z_T^n[\omega] + Z_0^n[\omega]\tanh[\gamma_0^n[\omega]l^n]}{1 + (Z_T^n[\omega]/Z_0^n[\omega])\tanh[\gamma_0^n[\omega]l^n]}, \quad for\ n = 1, \dots, 35 \quad (2.2)$$

Where ω is the circular frequency, C_g is the alveolar gas compression compliance based on the Dubois six-element airway model [18], R_t, $I_t and\ C_t$ are the Dubois model resistance, inertiance and compliance, and airway segments $n-1$ and $n-1-\Delta$ are the two daughters to the current parent segment. $Z_0^n[\omega]$ and $\gamma_0^n[\omega]$ denote the characteristic impedance and propagation coefficient of the *n*th airway segment, and can be calculated via:

$$Z_0^n[\omega] = \sqrt{\frac{Z^n[\omega]}{Y^n[\omega]}}, \quad (2.3)$$

$$\gamma_0^n[\omega] = \sqrt{Z^n[\omega]Y^n[\omega]}, \tag{2.4}$$

$$Z^n[\omega] = \frac{j\omega\rho_g}{A^n(1 - F_v^n[\omega]}, \tag{2.5}$$

$$Y^n[\omega] = \frac{j\omega A^n}{\rho_g c_g^2}(1 + 0.402F_t^n[\omega]) + \frac{1}{Z_w^n[\omega]l^n}, \tag{2.6}$$

$$F_v^n[\omega] = \frac{2}{a^n\sqrt{-j\omega\,\rho_g/\eta_g}}\frac{J_1\left[a^n\sqrt{-j\omega\,\rho_g/\eta_g}\right]}{J_0\left[a^n\sqrt{-j\omega\,\rho_g/\eta_g}\right]}, \tag{2.7}$$

$$F_t^n[\omega] = \frac{2}{a^n\sqrt{-j\omega\,C_g/\kappa_g}}\frac{J_1\left[a^n\sqrt{-j\omega\,C_g/\kappa_g}\right]}{J_0\left[a^n\sqrt{-j\omega\,C_g/\kappa_g}\right]}, \tag{2.8}$$

$$Z_w^n[\omega] = \frac{c^n}{Z_{w,c}^n[\omega]} + \frac{1 - c^n}{Z_{w,s}^n[\omega]}, \tag{2.9}$$

Here, $Z^n[\omega]$ and $Y^n[\omega]$ are the series impedance and shunt capacitance for the given *n*th order segment, ρ_g is the air density, η_g is the air viscosity and c_g is the speed of sound in air. C_g denotes the air specific heat and κ_g the thermal conductivity. A^n is the cross-sectional area of the inner diameter of the tubular segment, with l^n the length of the segment. The two terms $F_v^n[\omega]$ and $F_t^n[\omega]$, account for attenuation of sound via air viscosity and thermal dissipation. The last term, $Z_w^n[\omega]$, is the effective volumetric compliance of the *n*th order segment. The wall is composed of soft tissue ($Z_{w,s}^n[\omega]$ being the soft tissue compliance) and cartilage components ($Z_{w,c}^n[\omega]$ being the cartilage compliance) the cartilage fraction of which is given by c^n. From the trachea (n=35), cartilage is typically present down to n=17. The soft tissue and cartilage compliance is calculated using the series resistance (R_w), intertiance (I_w) and compliance (C_w) via

$$Z_{w,c\ or\ s}^n[\omega] = R_w^n + j(\omega I_w^n + 1/\omega C_w^n), \tag{2.10}$$

$$R_w^n = \frac{4h^n v_{c\ or\ s}}{\pi(d^n)^3 l^n}, \tag{2.11}$$

$$I_w^n = \frac{h^n \rho_{c\ or\ s}}{\pi d^n l^n}, \tag{2.12}$$

$$C_w^n = \frac{\pi(d^n)\text{^}3 l^n}{4h^n E_{c\ or\ s}}, \tag{2.13}$$

Where h^n is the thickness of the *n*th segment, $v, \rho_{c\ or\ s}$ is the viscosity and density, respectively, and $E_{c\ or\ s}$ denotes Young's modulus of the cartilage and soft tissue.

With equations (2.1-13), the impedances of the trees can be solved iteratively. Once all of the impedances are known, the pressures can be solved iteratively through calculating the pressure ratio of each segment ($P_{rat}^n[\omega]$) via:

$$P_{rat}^n[\omega] = \frac{P_T^n[\omega]}{P_{in}^n[\omega]} = Z_T^n[\omega]\left\{\frac{\cosh\left[\gamma_0^n[\omega]l^n\right]}{Z_{in}^n[\omega]} - \frac{\sinh\left[\gamma_0^n[\omega]l^n\right]}{Z_T^n[\omega]}\right\} \tag{2.14}$$

Once the pressure ratios for each segment are known, the inlet pressures can be calculated via an iterative calculation from the trachea down to the bronchioles, following the path of the downstream segments as follows:

$$P_{in}^{n-1}[\omega] = P_{in}^n[\omega] * P_{rat}^{n-1}[\omega] \tag{2.15}$$

There is commonly a $P_{in}^n[\omega]$ of 1 Pa input as a boundary condition in the 1D waveguide analytical models. Using this relationship to solve for input pressures, the pressure from $x = 0$ at the inlet of the segment to $x = l$ at the distal end of the segment can be solved via:

$$P^n[\omega, x] = \frac{Z_0^n[\omega]}{\sinh\left[\gamma_0^n[\omega]l^n\right]}\left\{\frac{P_{in}^n[\omega]}{Z_{in}^n[\omega]}\cosh\left[\gamma_0^n[\omega](x - l^n)\right] - \frac{P_T^n[\omega]}{Z_T^n[\omega]}\cosh\left[\gamma_0^n[\omega]x\right]\right\} \tag{2.16}$$

Which asserts that the terminal pressure $P_T^n[\omega]$ can be solved using $x = l$, reducing equation (2.16) to:

$$P_T^n[\omega] = \frac{Z_0^n[\omega]}{\sinh\left[\gamma_0^n[\omega]l^n\right]}\left\{-\frac{P_T^n[\omega]}{Z_T^n[\omega]}\cosh\left[\gamma_0^n[\omega]l^n\right]\right\} \quad (2.17)$$

2.2.3 1D MODIFIED WAVEGUIDE THEORY

Modifications were applied to the 1D waveguide to account for non-Horsfield compliant airway geometries. As explained in section 2.2.1, the geometry used in this study was a physiologically relevant airway conducting tree model, seen in Figure 2.1. Although the tree has an approximate Horsfield order, the geometric properties of each segment is unique with the exception of airway segment thickness, which is assigned via its approximate Horsfield number's thickness via Horsfield 1968 [24].

The modifications to the 1D waveguide are limited to two regions. For once, each calculation is done on a segment to segment basis. This means each equation is not a function of Horsfield order, but of segment number. Each segments geometrical properties are solved in a geometry structure, and referenced as necessary. As such, modifications are done on equations (2.1-17) to not calculate based on Horsfield order number, but instead the segment number (also called its face index). Additionally, equation 2.1 was modified to the following for non terminal segments:

$$Z_T^{parent}[\omega] = \frac{1}{1/Z_{in}^{daughter\ 1}[\omega] + 1/Z_{in}^{daughter\ 2}[\omega]} \quad (2.18)$$

Because of each segments unique geometry properties, the 1D waveguide's premise that for each iteration of the algorithm the acoustic properties would be solved for a sequential Horsfield number is inapplicable. This calls for a modified 1D waveguide that can accommodate these geometrical changes. Not only for geometrical reasons, but the parent-daughter connectivity is vastly different from ordered asymmetry. Because of this, the algorithm was changed to run recursively per bifurcation: each iteration of the algorithm instead of solving for a Horsfield order would run per bifurcation instead of solving for by Horsfield order, and go up and down the tree recursively, solving for acoustic parameters. The algorithm runs in 4 steps: first it initializes the

geometry, initial conditions, boundary conditions and material properties. Second, it solves for the characteristic impedance of each segment, as this calculation does not have any connectivity-related importance. Next, it solves for the impedances of the terminal bronchioles, which are assigned via assignment of impedances per frequency per closest Horsfield order number according to the original 1D waveguide. In this step, the algorithm takes the radii of the segment and relates it per the Horsfield table to the closest Horsfield order. An original 1D waveguide solution is loaded for reference, and per frequency, the results of the 1D waveguide from order number 1 to the order number assigned is assigned to the terminal impedance of the segment in question. This is taken to be an approximation in this regard, because in actuality there is no method (experimental or otherwise) to calculate the terminal impedance of those terminal segments otherwise. At the last stage of the algorithm, the algorithm runs recursively from a chosen terminal segment upwards, solving first for the input impedance via a modified eqn (2.2), not based on Horsfield numbers, and then solving for the pressure ratio using the input and terminal impedance via a modified eqn. (2.14). Once the segment's acoustic properties are calculated, it marches upwards, first attempting to solve for the parents terminal impedance. If both daughters input impedances are calculated, it solves for the terminal impedance of the parent via eqn (2.18). If one of the daughters input impedance is not calculated, it marches downwards to that unsolved daughter segment, repeating the calculation for the daughter (or perhaps marching further downwards). As the algorithm marches upwards and downwards, the algorithm will terminate when the trachea's input impedance is solved. Once all of the impedances and pressure ratios are calculated, the algorithm will initiate a trachea to bronchiole calculation, solving for pressures throughout the tree via modified eqns. (2.15-16). One important distinction to note here is that while the original 1D waveguide calculates acoustic properties per order, the modified 1D waveguide calculates acoustic properties on a segment to segment basis because each segment is unique.

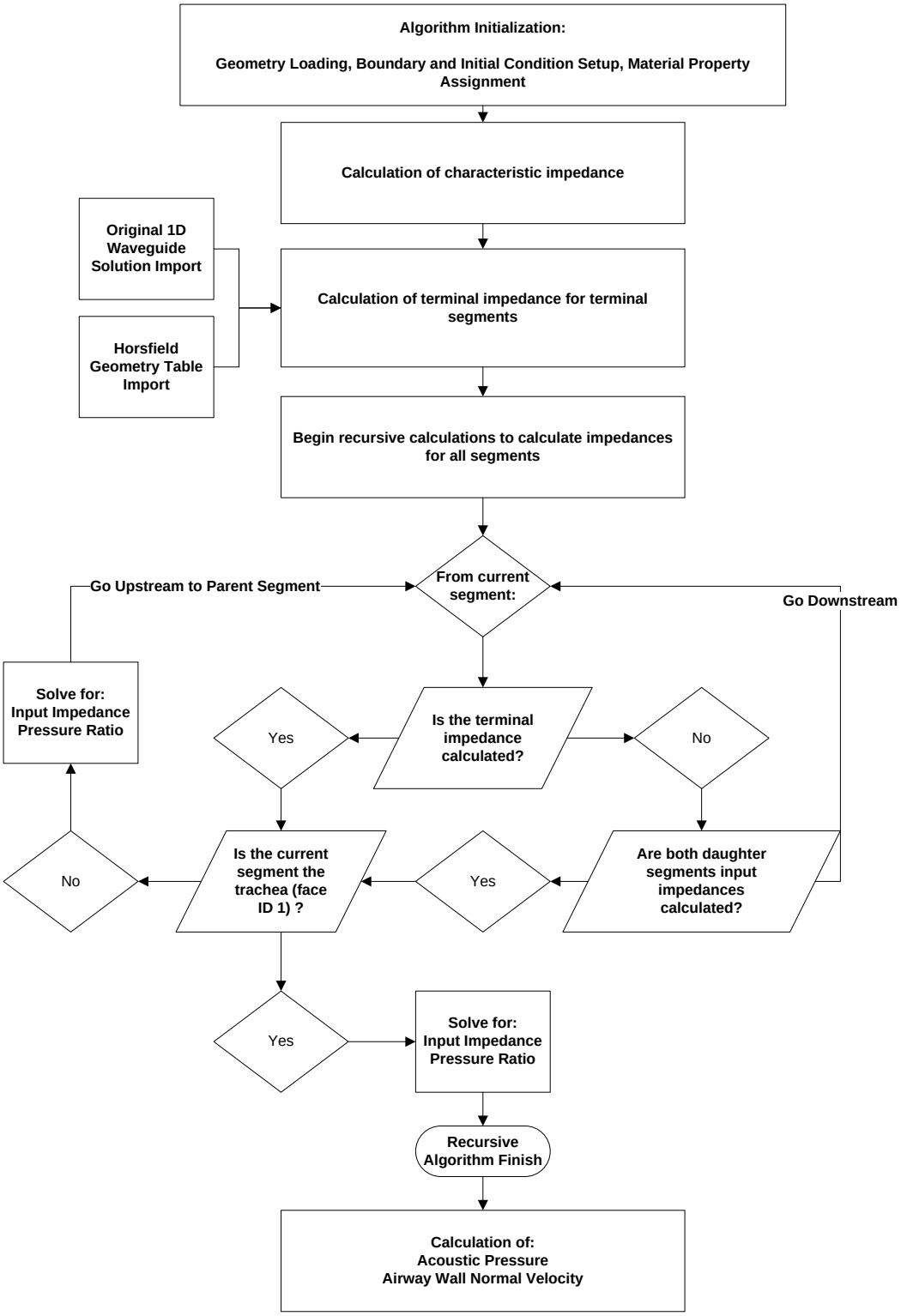

Figure 2.5. Modified 1D waveguide algorithm flowchart.

The modification of the 1D waveguide is also not limited to the models presented in this dissertation. The algorithm is designed to input any valid 3D geometry created by the hybrid segmentation method, and calculate the acoustic profile in addition to visualizing the results. This is important as a part of the algorithms evolution because as patient-specific modeling becomes more commonplace, specifically in terms of modeling pathological cases relative to healthy cases, the modified 1D waveguide is developed to accommodate the geometries if the information is parsed correctly. Not only does this give the modified 1D waveguide a heavily dynamic use range relative to the original 1D waveguide, but further developments to the algorithm are easier to make because the recursion involved with calculating of acoustic properties won't change: only the calculations around it. This dynamic use is similar to the hybrid generation technique intentionally to make the algorithm useful in further cases beyond the scope of this dissertation.

2.3 AIRWAY ACOUSTICS IN A HUMAN AIRWAY GEOMETRY

2.4.1 MODIFIED 1D WAVEGUIDE VALIDATION

***Validation by comparison to previous waveguide and experimental study*.** In Section 2.2.3, a modified 1D waveguide was outlined with the ability to acoustically map a non-compliant Horsfield conducting airway tree. In Ref. 15, the 1D waveguide was validated by comparison to experimental and numerical finite element (FE) simulations of an ecoflex airway phantom with similar geometry. In this section, the modified 1D waveguide presented in this dissertation was compared to the 1D waveguide used on an identical airway geometry in Ref. 15. The boundary conditions, initial conditions and material properties were identical compared to those in Ref. 15.

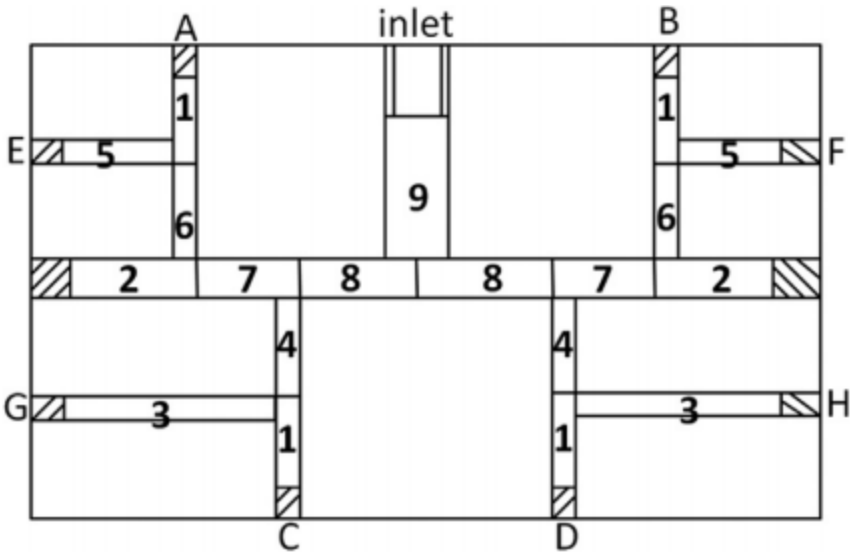

Figure 2.6. Airway phantom schematic with locations A-H labeled.

In the comparison study, the terminal acoustic pressures were measured at locations A, C, E and G (and thus B, D, F and H by the model's half-symmetry) via equation (2.17).

In the case of the original waveguide simulation, the airway tree preserved its original Horsfield ordering and no algorithmic changes were made. Impedances and pressures were solved via equations (2.1-17). In the modified 1D waveguide simulation, the tree was decoupled from its Horsfield ordering and restructured into a connectivity matrix, and calculations of the impedances and pressures followed the methodology presented in Section 2.2.3.

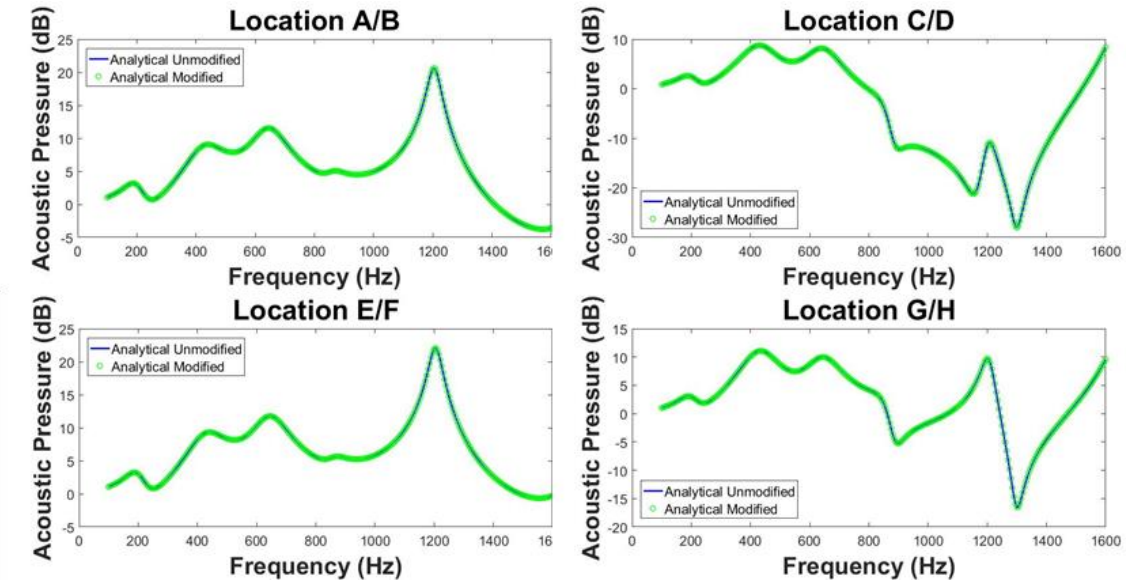

Figure 2.7. Acoustic pressures at locations A-H (see Figure 2.6), reference to inlet acoustic pressure.

Acoustic pressures calculated via the 1D waveguide with Horsfield-ordered geometry and modified 1D waveguide with non-Horsfield-ordered geometry were identical at all locations across all frequencies. In addition, calculations of Z_T, Z_{in}, P_{rat} via equation (2.1, 2 and 18) for the original and modified 1D waveguide respectively were identical across every cylindrical segment. Per Ref. 15, while there is some discrepancy with the waveguide accuracy at lower frequencies relative to the experimental results (at lower frequencies, wall compliance is a larger contributing factor, and the phantom model does not have uniform thickness), the waveguide solution and experimental measurements had a good match over 600 Hz.

Validation by comparison to numerical FE involving a partial large segment airway tree. Using the same conducting airway tree geometry presented in Section 2.2.1, a partial tree was constructed using the airways included in Horsfield order 20 to 28. This included the trachea, mainstem bronchi, and several downstream generations. In addition, an identical geometry was volume meshed and prepared for numerical FE analysis. In order to further validate the modified

1D waveguide approach, the numerical FE analysis was compared versus the 1D modified waveguide solution.

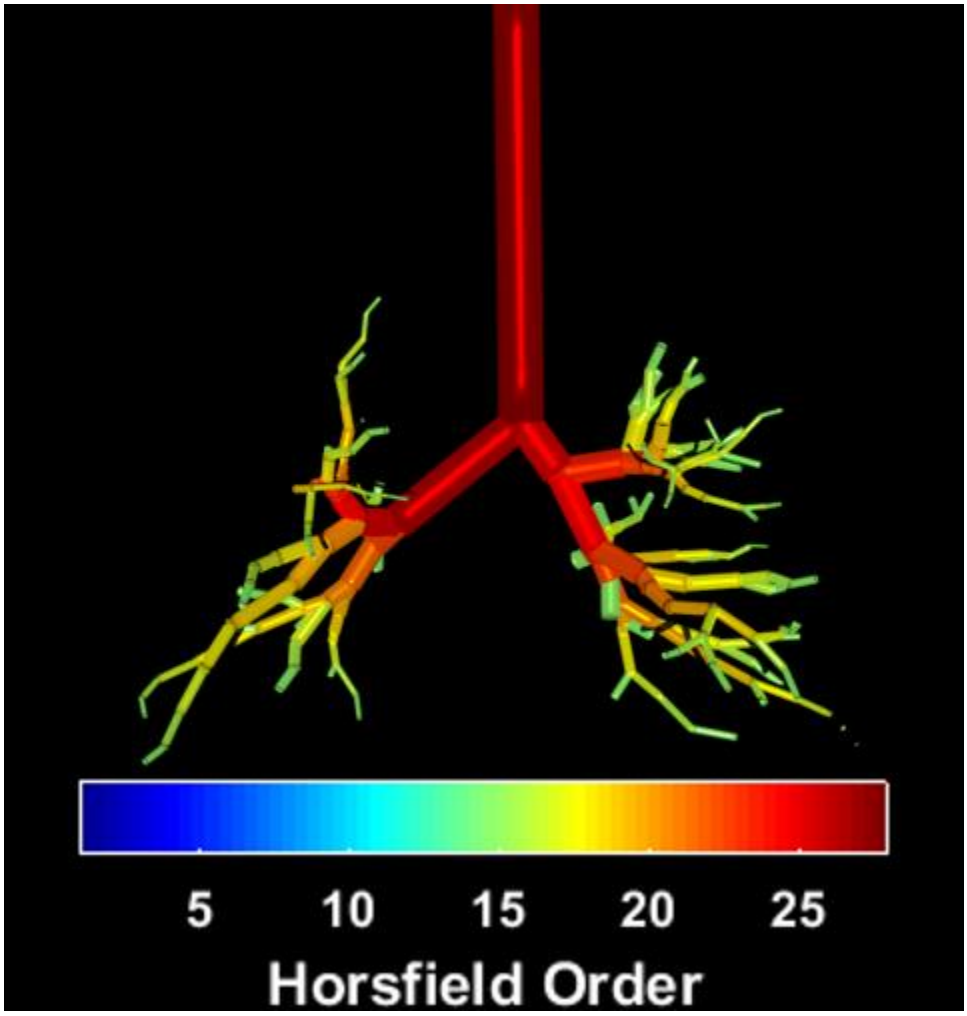

Figure 2.8. The partial airway geometry used in the numerical FE validation study.

The FE model was prepared in ANSYS ICEM CFD [25] through use of tcl (tool command) script files. A hollow tube geometry was constructed in four parts: geometry was first scripted to generate the inner tube geometry up to the terminal segments, incorporating spheres at junctions to smooth the transitions, then another script built on the terminal segments using primitive cylinders. An identical process was used to generate the outer cylinders, and the two mesh files were merged to create the bifurcating tubular network with two volumes (for the wall thickness

and air). The scripts were generated using MATLAB 2016a [26]. The numerical FE analysis was performed in COMSOL Multiphysics [27]. Shown below in Table 2.1 are the material properties used in this study. The material properties were obtained from literature and represent physiological values [1,-11-12].

Variable	Units	Value
Air Density	$\rho_g \left(\frac{kg}{m^3}\right)$	1.14
Air Viscosity	$\eta_g (Pa\ s)$	1.86 x 10^{-5}
Speed of Sound in Air	$c_g \left(\frac{m}{s}\right)$	343.0
Airway Wall Elastic Modulus	$E_w (Pa)$	5.81 x 10^4 soft tissue 3.92 x 10^5 cartilage
Airway Wall Viscosity	$\eta_w (Pa\ s)$	102.0 soft tissue 688.0 cartilage
Airway Wall Poisson's Ratio		0.4995

Table 2.1. Viscoelastic properties used in experimental, numerical and analytical cases

Lung parenchyma material property values were used for the airway wall soft tissue component. Within COMSOL, in order to measure the response on the airway wall accurately, the elastic material was defined by its complex Young's modulus, Poisson's ratio and lung density. In both analytical and numerical FE models, the airways were insonified at the top of the trachea with a sinusoidal acoustic source at 1 Pa pressure, with spectral content from 100 to 800 Hz in 100 Hz increments.

The post processing was handled in MATLAB, on a 64-bit Windows computer with two 4-core processors at 2.7 GHz and 16 GB RAM. The acoustic pressures solved in COMSOL were

exported at points defined in the analytical model. The analytical simulations relative to the numerical FE simulations took 0.0857 s and 3261 s respectively for one frequency with the partial tree, and 0.1180 s and 32,640 s respectively for 10 frequencies. For each segment, there were 9 interpolated pressures solved for via eqn (2.18) using linearly spaced values from $x = 0$ to $x = l$ in 12.5% increments of the length value. The x, y and z coordinates at these points were calculated and used as the point measurement locations in COMSOL to export. The acoustic pressures for the analytical and numerical FE simulations can be seen below in Figure 2.9.

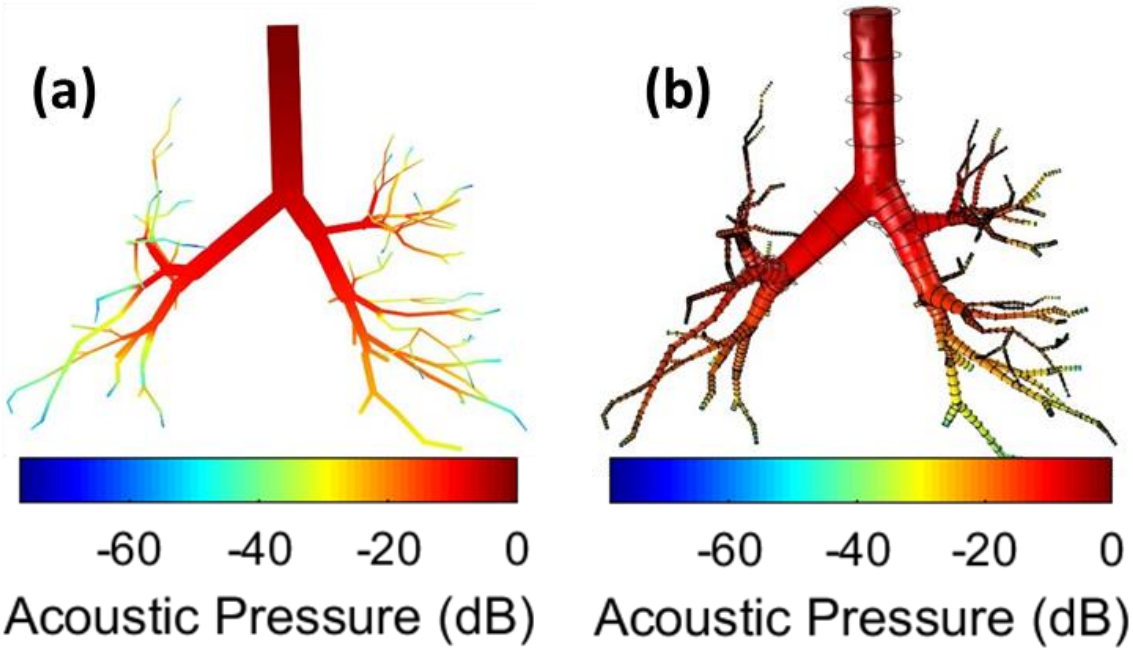

Figure 2.9. Acoustic pressures of (a) analytical and (b) numerical FE simulations in dB, ref 1 Pa.

The difference between the analytical and numerical FE values can be seen below Figure 2.10. The error was calculated via the following expression:

$$\% \, Error = \frac{dB \; Pressure_{FE} - dB \; Pressure_{analytical}}{dB \; Pressure_{analytical}} * 100 \tag{2.19}$$

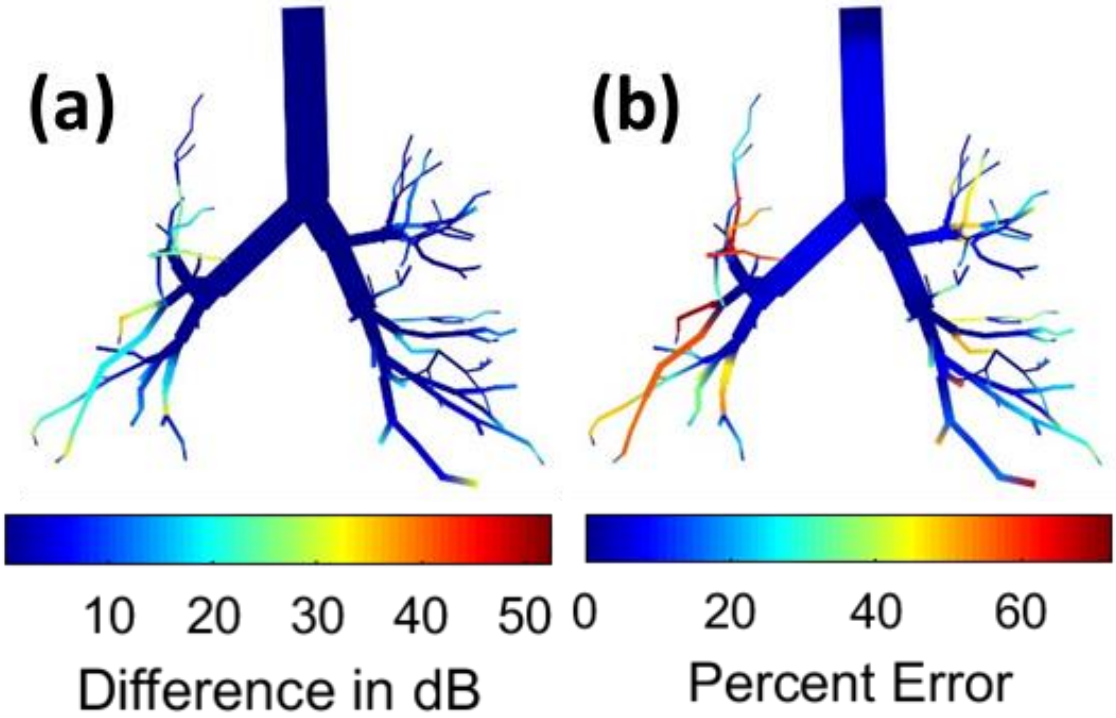

Figure 2.10. Comparison of analytical (0.35 s runtime) versus numerical FE (3861 s runtime) acoustic pressures. (a) Magnitude of the difference in dB (ref. 1 Pa) between analytical and numerical FE acoustic pressures. (b) % Error between the analytical and numerical FE acoustic pressures.

Figure 2.9 shows a good match in the pressure distribution between the analytical and numerical FE simulation results at 400 Hz. This is validated by the difference in dB and low error values in Figure 2.10. The error in the trachea, mainstem bronchi and next generation is minimal, ranging from 0-10%, with the error rising as the Horsfield number decreases downstream. One possible reason for this is the 1D waveguide's inability to model tortuous segments: in the conducting airway model, tortuosity is captured by connecting multiple airway segments without bifurcation. In the partial airway tree shown in Figure 2.8, the downstream airway segments were excluded from the model as they were not within the Horsfield range of inclusion (Horsfield order 20 to 28), leading multiple downstream segments to lose their bifurcations, increasing segment tortuosity. In context of the 1D waveguide, the 1D waveguide treats these as single straight segments, whereas in the numerical FE model, the tortuosity can lead to turbulent acoustical flow

along the twists of these segments. This is not a concern in the full conducting tree model, however, as the number of non-bifurcating segments is minimal (3 within 59,834 segments). One possible avenue for research in the future would be to numerically simulate the full conducting tree and perform a similar validation study, but currently it is impossible to transform the full conducting tree into a comparable FE model, as the number of degrees of freedom would be enormous.

2.4.2 1D WAVEGUIDE SIMULATION IN A HUMAN AIRWAY TREE

Using the geometry presented in Section 2.2.1 and the modified waveguide analytical method presented in Section 2.2.3, four analytical models representing a healthy human male subject were created, and three modified were modified to represent three pathological conditions: PF, bronchoconstriction, and pulmonary infiltrate. Using the material properties in Table 2.1, shown below in Figure 2.11 is a graphical depiction of the wall radial velocity in dB (ref. 1 m/s) of the conducting airway tree model. While a broad range of frequencies were calculated, for brevity 400 Hz was chosen to be presented, because of its relevance in respiratory sounds and applicability in dynamic elastography test methods.

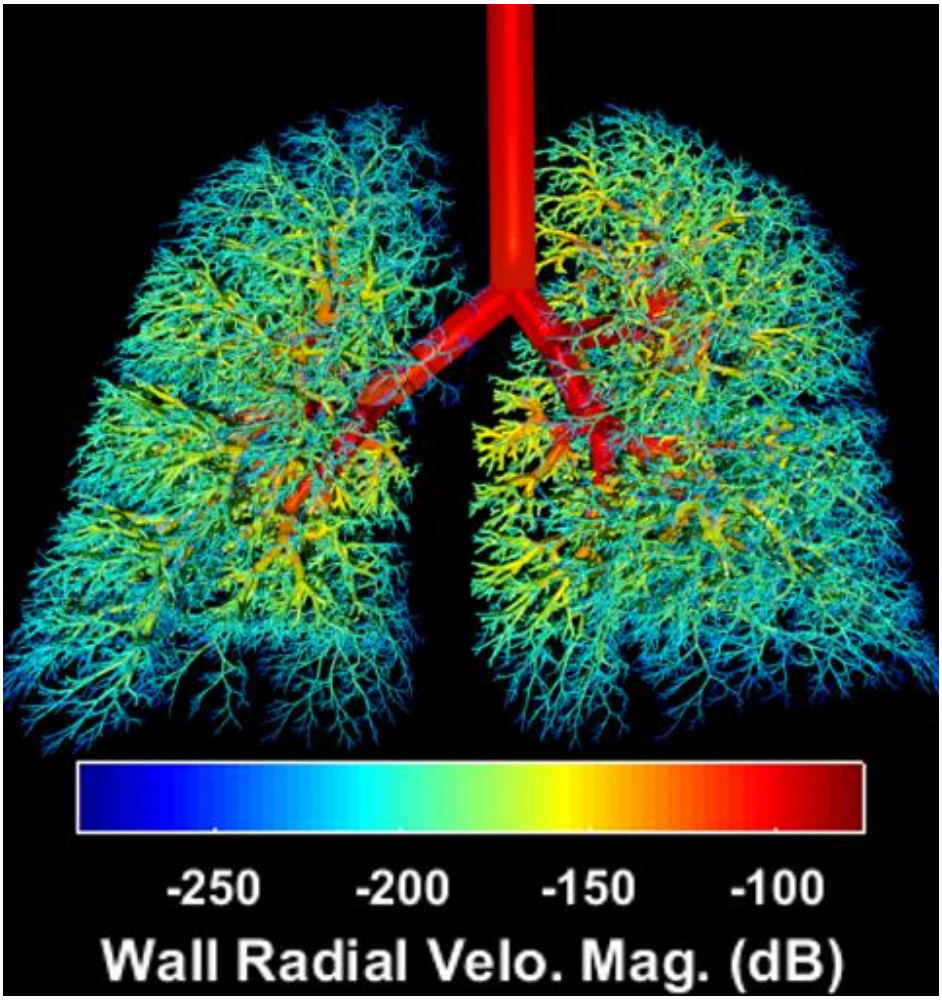

Figure 2.11. Airway wall normal velocity in dB (ref. 1 m/s) of a full conducting tree model.

2.4.3 PATHOLOGIC CASE GENERATION AND SIMULATION

To simulate PF, the airway wall stiffness was changed globally to be five times its original value as a material property [33, 34]. This was accomplished in the Algorithm Initialization step in Figure 2.5, by increasing the real part of Young's modulus by 500%. In the PF model there was no change to geometry. The generated bronchoconstriction model to simulate asthma had several geometric changes per Ionescu et al. [35]: in airways smaller than 2mm the soft tissue thickness in the airway wall was increased by 150%, and the inner tubular radius was reduced by 50% of the soft tissue fraction of the airway wall outer diameter. The change in inner and outer tubular

radius was done to model airway remodeling present in asthma, and also to account for the presence of mucous. In the PI model, no material or geometric changes were made, but the terminal impedance of segments in the afflicted lobe was modified to account for a hard sound boundary introduced to mimic airway occlusion: Z_T of the terminal segments in the left inferior lobe was set to infinite to mimic a sound hard boundary. All other lobes had no change in boundary conditions.

Shown below in Figure 2.12 are graphical depictions of the wall radial velocity in dB (ref. 1 m/s) of the conducting airway tree models for PF, bronchoconstriction and PI.

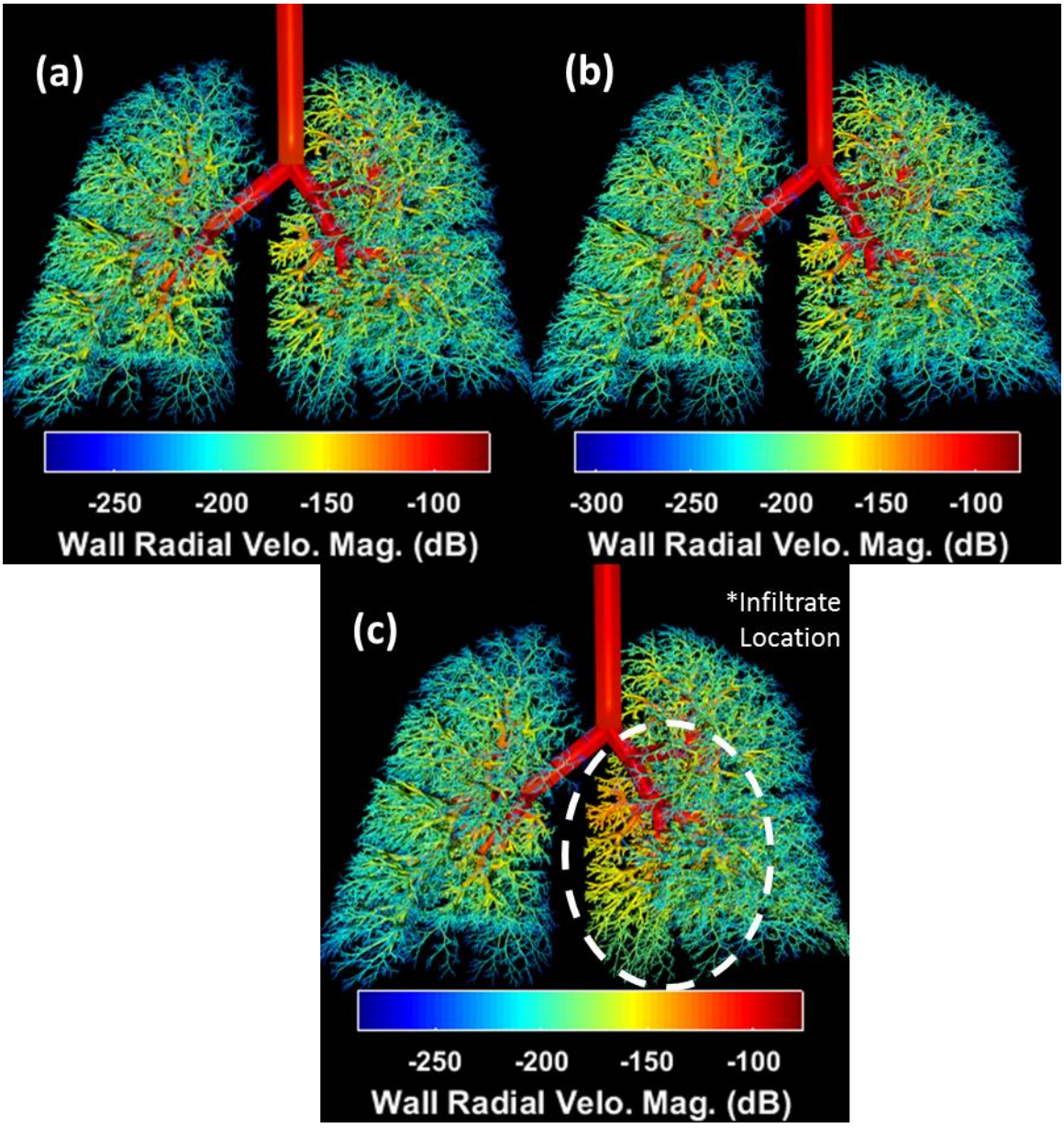

Figure 2.12. Airway wall normal velocity in dB (ref. 1 m/s) for (a) PF model, (b) bronchoconstriction model, and (c) PI model.

Below in Figure 2.13 show airway velocity from 10 Hz to 1600 Hz in 10 Hz increments for healthy and pathologic cases at different locations in the conducting tree. Each of these models were insonified via the top of the trachea (8.39 cm in length). For a rigid tube of this length with the distal end closed and proximal end open, there will be resonance in the excitation source wavelength at four times the length of the trachea. Using a speed of sound of 343 ms, the speed

of sound in air, this corresponds to 1 and 2 KHz, respectively. Seen below in Figure 2.13, this peak has shifted to 1.2 KHz, which is consistent with previous literature where the resonant peak was shifted 1.2 times the predicted resonance [36]. Of note, the introduction of a PF model did not cause a shift in this resonant frequency, and can be seen at both inlet and outlet locations in the conducting tree model.

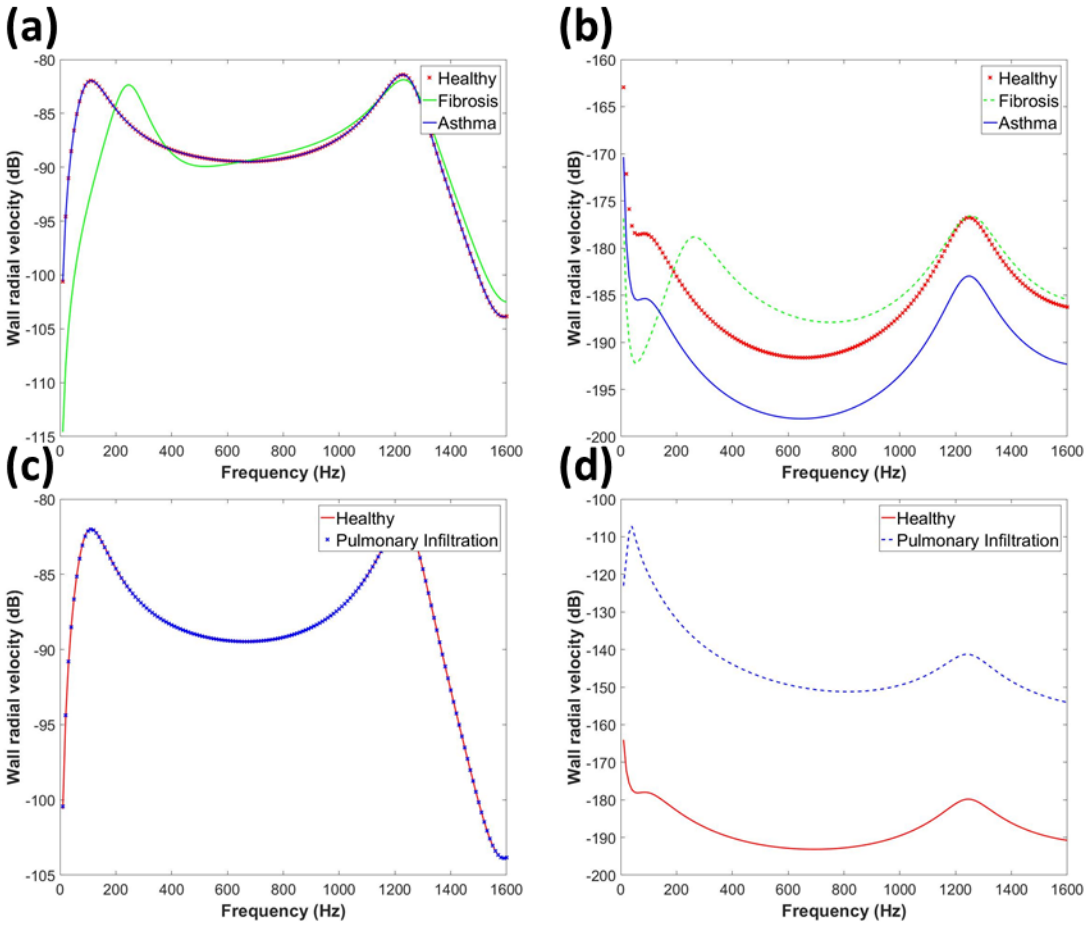

Figure 2.13. Airway wall normal velocity (ref. 1 m/s) at (a), (c) midpoint of the trachea, and (b), (d) mean terminal segment. (a), (b) compare healthy, PF and bronchoconstriction cases, and (c), (d) compare healthy and PI cases.

2.4 DISCUSSION

Sound transmission over a complex 3D conducting airway tree was calculated using a modified 1D waveguide. The modified 1D waveguide was validated by comparison to previous

studies of a branching airway network in Ref. 15 in addition to numerical FE studies using a partial conducting tree incorporating the larger conducting airways. A single frequency model using the full conducting tree model solved using the modified 1D waveguide took 44.172 s to solve, with ten frequencies increasing the runtime to 70.833 s. In addition, a wideband frequency study from 10 to 1600 Hz, in 10 Hz increments averaged around 300 s to solve, and required 600 MB of memory during runtime. Increasing the number of frequencies further per study can be streamlined through parallel processing.

Previous analytical approaches incorporated limited use of the 1D waveguide on Horsfield geometric models. These models had several limitations: adherence to a self-similar geometry, 2D models and asymmetry based on a delta value that is lacking in physiological relevance. Through use of the hybrid segmentation approach, a complex physiologically relevant 3D human conducting airway tree was created and obtained from Ref. 19 to use in acoustic studies. Additionally, through restructure of the 1D waveguide, the application of the algorithm was expanded to incorporate geometries based on parent-daughter connectivity rather than Horsfield ordering. Additionally, the algorithm can also accommodate non-bifurcating segments to be included near the conducting tree terminals. Put in context, the modified 1D waveguide allows for acoustic mapping of complex 3D conducting trees generated automatically that have patient-specificity and physiological relevance. However, as a future aspect of study it would be of interest to test the sensitivity of the predictions to changes in algorithmically-generated conducting airway trees.

Acoustic maps of the airway wall normal velocity and acoustic pressure are of interest in developing new diagnostic techniques without the need for invasive methods. Each pathologic case exhibited quantitative differences, both locally and globally, in terms of acoustic pressure and airway wall normal velocity. The PF model predicted twice of what is suspected to be the Helmholtz resonant frequency to about 250 Hz (Fig. 2.13(a)) due to the increased wall stiffness,

and thus reduced airway wall compliance and increased impedance, throughout the system. Subjects with bronchoconstriction show a decrease in wall normal velocity in the mean terminal segment across all frequencies (Fig. 2.13(b)) possibly because of the significant increase in wall impedance, while fibrosis shows an increase in wall radial velocity at about 300 Hz and above due to the increased acoustic mismatch in the larger airway segments. A sudden decrease in mean terminal inner tubular radius also suggests less acoustic energy reaching the lumen of the terminal segments in the first place.

Introduction of a pulmonary infiltrate caused a significant increase of mean terminal segment airway wall normal velocity across all frequencies, but no change in the tracheal airway wall normal velocity (Fig. 2.13 (c-d)). Introduction of the hard sound boundary at the terminal segments of the afflicted lobe may be the cause. The hard sound boundary is created to simulate airways blockage, causing the gas exchange segments underneath to be inaccessible, also directly increasing acoustic impedance and thus the load on the surrounding airway walls. This is directly linked with an increased airway wall normal velocity at those terminals segments.

In all insonification cases, the sound attenuates rapidly (50 to 60 dB or 3 orders of magnitude) as it travels as low as 5 or 6 bifurcations: in the 3D conducting tree model, there were 28 approximate Horsfield orders. This suggests that the downstream airways contribute a negligible effect of energy that reaches the torso surface. Thus, for tracheal insonification models, fewer airway generations (5 or 6 generations) may be suitable for auscultation simulation. However, this is not the case in adventitious breathsound acoustic modeling, where the acoustic source may originate in the lower airways. In these models, complex 3D models may be necessary to calculate the spatial and spectral information contained in the acoustic profile.

2.5 CONCLUSION AND FUTURE WORK

Sound transmission in a 3D complex conducting airway tree, multiscale in terms of radial diameter from the trachea (cm) to bronchioles (hundreds of microns) is analytically modeled via use of a

modified 1D waveguide. The model is viscoelastic, accounting for complex phenomenon such as airway wall compliance and hysteresis, and performed on a patient-specific backbone exhibiting strong physiological relevance. The full conducting tree consists of ~60,000 airway segments. Validity of the fidelity of the modified 1D waveguide was shown via comparison to previous studies on a branching airway network, experimental studies, and in another study with numerical FE comparison. The existing airway model was modified to account for three pathological states: PF, bronchoconstriction and PI. Each case resulted in quantifiable differences in acoustic parameters that lay groundwork for potential advances in noninvasive diagnosis.

Future work includes expansion of the conducting tree model to a full airway tree and incorporating segments from the bronchioles to the alveoli. The geometry system can also be expanded to include not only the airways, but also the surrounding organs in the thoracic cavity (of note: the torso, ribcage, scapula and sternum) for a full thoracic cavity model. Such a model would prove useful in several ways: sound coupling from the airways can be radiated to the chest wall, potentially allowing existing surface auscultative and dynamic elastography techniques to be incorporated to possibly diagnose lung diseases and advancing further studies. More in-depth studies involving a wider array of pathologies, with more model adjustments, are needed to fully assess the system's capabilities in interpretation of diagnostic measurements.

REFERENCES

[1] R. H. Habib, R. B. Chalker, B. Suki, and A. C. Jackson, "Airway geometry and wall mechanical properties estimated from subglottal input impedance in humans," *J. Appl. Physiol.,* vol. 77, pp. 441–451, 1994.

[2] A. C. Jackson, J. P. Butler, E. J. Millet, F. G. Hoppin, Jr., and S. V. Dawson, "Airway geometry by analysis of acoustic pulse response measurements," *J. Appl. Physiol.,* vol. 43, pp. 523–536, 1977.

[3] A. C. Jackson, J. P. Butler, and R. W. Pyle, Jr., “Acoustic input impedance of excised dog lungs,” *J. Acoust. Soc. Am.,* vol. 64, pp. 1020–1026, 1978.

[4] S. Sethi, J. Yin, and P. Anderson, “Lung flute improves symptoms and health status in COPD with chronic bronchitis: A 26 week randomized controlled trial,” *Clin. Transact. Med.,* vol. 3, pp. 29, 2014.

[5] B. C. Goss, K. P. McGee, E. C. Ehman, A. Manduca, and R. L. Ehman, “Magnetic resonance elastography of the lung: Technical feasibility,” *Magn. Reson. Med.*, vol. 56, pp. 1060–1066, 2006.

[6] Y. K. Mariappan, K. J. Glaser, R. D. Hubmayr, A. Manduca, R. L. Ehman, and K. P. McGee, “MR elastography of human lung parenchyma: Technical development, theoretical modeling and in vivo validation,” *J. Magn. Reson. Imag.*, vol. 33, pp. 1351–1361, 2011.

[7] T. J. Royston, X. Zhang, H. A. Mansy, and R. H. Sandler, “Modeling sound transmission through the pulmonary system and chest with application to diagnosis of a collapsed lung,” *J. Acoust. Soc. Am.*, vol. 111, pp. 1931–1946. 2002.

[8] M. B. Ozer, S. Acikgoz, T. J. Royston, H. A. Mansy, and R. H. Sandler, “Boundary element model for simulating sound propagation and source localization within the lungs,” *J. Acoust. Soc. Am.,* vol. 122, pp. 657–671, 2007.

[9] S. Acikgoz, M. B. Ozer, T. J. Royston, H. A. Mansy, and R. H. Sandler, “Experimental and computational models for simulating sound propagation within the lungs,” *ASME J. Vib. Acoust.*, vol. 130, pp. 021010, 2008.

[10] Y. Peng, Z. Dai, H. A. Mansy, R. H. Sandler, R. A. Balk, and T. J. Royston, “Sound transmission in the chest under surface excitation: An experimental and computational study with diagnostic applications,” *Med. Biol. Eng. Comput.*, vol. 52, pp. 695–706, 2014.

[11] Z. Dai, Y. Peng, B. Henry, H. A. Mansy, and T. J. Royston, “A comprehensive computational model of sound transmission through the porcine lung,” *J. Acoust. Soc. Am.*, vol. 136, pp. 1419–1429, 2014.

[12] Y. Peng, Z. Dai, H. A. Mansy, B. H. Henry, R. H. Sandler, R. A. Balk, and T. J. Royston, “Sound transmission in porcine thorax through airway insonification,” *Med. Biol. Eng. Comput.*, vol. 54, pp. 675–689, 2015.

[13] M. Tawhai, A. Pullan and P. Hunter, "Generation of an anatomically based three-dimensional model of the conducting airways," *Annals of Biomed. Eng.*, vol. 24, pp. 793-802, 2000.

[14] M. Tawhai, P. Hunter, J. Tschirren, J. Reinhardt, G. McLennan and E. Hoffman, "CT-based geometry analysis and finite element models of the human and ovine bronchial tree," *J. Appl. Physiol.,* vol. 97, no. 6, pp. 2310-2321, 2004.

[15] Z. Dai, Y. Peng, H. A. Mansy, R. H. Sandler, and T. J. Royston, “Experimental and computational studies of sound transmission in a branching airway network embedded in a compliant viscoelastic medium,” *J. Sound Vib.*, vol. 339, pp. 215–229, 2015.

[16] B. Henry and T. Royston, "A multiscale analytical model of bronchial airway acoustics," *J. Acoust. Soc. Am.*, vol. 142, no. 4, pp. 1774-1783, 2017.

[17] Habib, R. H., Suki, B., Bates, J. H., and Jackson, A. C., “Serial Distribution of Airway Mechanical Properties in Dogs: Effects of Histamine,” *Journal of Applied Physiology*, vol. 77, pp. 554-566, 1994.

[18] A. Dubois, A. Brody, D. Lewis, and B. Burgess, Jr., “Oscillation mechanics of lungs and chest in man,” *J. Appl. Physiol.,* vol. 8, pp. 587–594, 1956.

[19] S. Miyawaki, S. Choi, E. Hoffman, and C.-L. Lin, “A 4DCT imaging-based breathing lung model with relative hysteresis,” *J. Comput. Phys.,* vol. 326, pp. 76–90, 2016.

[20] S. Miyawaki, M. Tawhai, E. Hoffman, S. Wenzel, and C.-L. Lin, 2016, “Automatic construction of subject-specific human airway geometry including trifurcations based on a CT-segmented airway skeleton and surface,” *Biomech. Model. Mechanobiol.*, vol. 16, pp. 583–596, 2016.

[21] Jahani N, Choi S, Choi J, Iyer K, Hoffman E, Lin C-L, “Assessment of Regional Ventilation and Deformation Using 4D-CT Imaging for Healthy Human Lungs during Tidal Breathing”. *J. Appl. Physiol.,* vol. 119, no. 10, pp. 1064-1074, 2015.

[22] Haefeli-Bleuer, B, Weibel, E.R., “Morphometry of the human pulmonary acinus”. *Anat. Rec.*, vol. 220, pp. 401-414, 1988.

[23] Wang, C. Y., Schuermans, D., van Muylem, A., Paiva, M., Noppen, M., Vincken, W., “Bifurcating distributive system using Monte Carlo method”. *Mathl. Comput. Modeling*, vol. 16, no. 3, pp. 91-98, 1992.

[24] K. Horsfield and G. Cumming, "Morphology of the bronchial tree in man," *J. Appl. Physiol.,* vol. 52, pp. 373-83, 1968.

[25] ANSYS ICEM CFD, Version 17.1 (ANSYS Inc., Canonsburg, PA, 2016).

[26] MATLAB, Version 9.0.1 (The MathWorks Inc., Natick, MA, 2016a).

[27] COMSOL, Version 5.2a (Comsol Inc., Burlington, MA, 2016).

[28] A. Cancellieri, G. Dalpiaz, M. Maffessanti, A. Pesci, R. Polverosi, and M. Zompatori, “Cystic diseases,” in Diffuse Lung Disease: Clinical Features, Pathology, HRCT (Springer, New York, 2007), Chap. 6, pp. 202–206.

[29] E. R. Fernandez Perez, C. E. Daniels, D. R. Schroeder, J. St. Sauver, T. E. Hartman, B. J. Bartholmai, E. S. Yi, and J. H. Ryu, “Incidence, prevalence, and clinical course of idiopathic pulmonary fibrosis: A population-based study,” *Chest,* vol. 137, pp. 129–137, 2010.

[30] S. Yim Yeh and R. Schwartzstein, “Asthma: Pathophysiology and diagnosis,” in Asthma, Health and Society: A Public Health Perspective (Springer, New York, 2010), Chap. 2, pp. 19–42.

[31] A. Siddiqui and S. Ahmed, “Pulmonary manifestations of sickle cell disease,” *Postgrad. Med. J.*, vol. 79, pp. 384–390, 2003.

[32] M. Kompis, H. Pasterkamp, and G. R. Wodicka, “Acoustic imaging of the human chest,” *Chest,* vol. 120, pp. 1309–1321, 2001.

[33] T. Ebihara, N. Venkatesan, R. Tanaka, and M. S. Ludwig, “Changes in extracellular matrix and tissue viscoelasticity in bleomycin-induced lung fibrosis: Temporal aspects,” *Am. J. Respir. Crit. Care Med.*, vol. 162, pp. 1569–1576, 2000.

[34] F. Liu, J. D. Mih, B. S. Shea, A. T. Kho, A. S. Sharif, A. M. Tager, and D. J. Tschumperlin, “Feedback amplification of fibrosis through matrix stiffening and COX-2 suppression,” *J. Cell. Biol.*, vol. 190, pp. 693–706, 2010.

[35] C. M. Ionescu, P. Segers, and R. De Keyser, “Mechanical properties of the respiratory system derived from morphologic insight,” *IEEE Trans. Biomed. Eng.*, vol. 56, pp. 949–959, 2009.

[36] A. C. Jackson, J. P. Butler, and R. W. Pyle, Jr., “Acoustic input impedance of excised dog lungs,” *J. Acoust. Soc. Am.*, vol. 64, pp. 1020–1026, 1978.

CHAPTER 3

BREATHSOUND PATHOPHYSIOLOGY AND ACOUSTICAL MODELING

3.1 INTRODUCTION

Sickle Cell Disease (SCD) is one of the most common autosomal recessive disorders in the world, with approximately 30 million people worldwide diagnosed. It has a higher prevalence in people of African descent: 0.15% of African-Americans are homozygous and 8% heterozygous for SCD in the US. More than 60% of the population in sub-Saharan Africa has the trait, and about 4% of children are born with SCD [1].

For people suffering from SCD, although over 90% of people with the condition are past twenty years of age, the median lifespan is less than fifty years old in the US [2,3]. Pain is the leading cause for hospitalization for patients with SCD[4], with acute chest syndrome (ACS)[5] being second. ACS is also a leading cause of death for patients with SCD. ACS is such a prevailing symptom for SCD patients that nearly 50% of patients will have at least one ACS episode in their lifetime [6, 7]. In addition, 10-20% of SCD hospitalized adult patients have ACS, usually occurring at one to three days after hospital admission. ACS related deaths are four times more prevalent in adults than children [6], but with advances in medical care in the past century more people live to adulthood, which is a concern in the future as it is currently impossible to predict future ACS episodes in patients [7]. There have been some recent advances in multi-predictive strategies aimed at using biological and clinical markers, but unfortunately time is needed to develop the statistical probabilities of their success, and the results often lag relative to clinical decision making [8]. Implementing better early stage diagnostic methods of ACS may be lifesaving and are urgently needed.

ACS is characterized as an acute lung injury syndrome. It is diagnosed via medical imaging of a new pulmonary infiltrate in conjunction with fever and adverse respiratory symptoms (cough, chest pain, tachypnea and hypoxia as examples), and can be characterized via chest radiographs

(CXR) using bedside chest radiographs although CT imaging has been found to diagnose ACS earlier than CXR. CT imaging however requires specialists to perform and interpret results, requires patient relocation and is very expensive. Repeated use of CT imaging is also correlated with higher exposure to radiation and carries potentially dangerous complications [9], although new advances in low-dose CT protocols show promise in reducing total radiation risk. The physical attributes of the airways are changed for patients with pulmonary infiltrate: alveolar consolidation occurs in at least one lobe in the lung, causing a cascade of additional complications in the patient from reduced lung volume to other airway pathologies. As a result, acute respiratory distress syndrome (ARDS) is considered to be similar to pulmonary infiltrate.

Given the difficulty in future ACS episode prediction and the difficulty of current diagnosis of SCD, adverse SCD reactions very commonly require hospitalization and emergency treatment. SCD is correlated with acute painful crisis resultant from inflammation, which often causes serious complications such as organ failure, multi-organ failure or death. More concerning is the fact that physiologic effects leading to adverse ACS episodes may start while the patient is at home pre-hospitalization, making predictions difficult to make without continual monitoring. Changes in pulmonary acoustics associated with ACS can be detected and analyzed, leading to potential diagnostic and predictive methods. Such diagnostic and predictive methods are cheaper, do not require specialist intervention and are more mobile.

Noninvasive acoustic methods to determine the material properties of various adverse breathsounds can be invaluable in the early prodromal phase of ACS, where accurate detection can lead to earlier treatment and thus less severe ACS episodes. Breathsounds often have unique acoustic properties that can be detected; acoustic crepitations (crackles) can be detected via chest auscultative methods in ACS [10]. In addition, the frequency of severe wheezes detected can be used as a measure of ACS and SCD progression [11]. For those patients with a detected recurrent high frequency of severe wheezes, the patients were recorded with having decreased

lung function, twice the rates of pain and higher risk of death relative to patients without a recurrent high frequency of severe wheezes. This metric was independent whether or not the patient had asthma. It has been further suggested that wheezing in conjunction with SCD can be an indicator of disease severity [11].

While there is potential in acoustical methods for noninvasive diagnosis and detection, there are several confounding conditions that diminish the specificity and sensitivity of acoustical approaches. For example, is there a quantifiable or detectable acoustic difference with ACS patients who do or do not have asthma? This distinction is important because treatment would differ depending on the patient's asthma condition. Put in context, systemic steroids are used in asthmatic cases to relieve symptoms, but in SCD patients they can lead to an increase in adverse reactions including cerebrovascular accidents and pain [12, 13]. There have been some differences reported between asthmatic and non-asthmatic subjects who have had recurrent high frequency wheezing and SCD. Nitric acid (NO) is exhaled in greater volumes in acute asthmatic patients. However, SCD is also correlated with reduced NO volume due to complexing with free intravascular Hb [14]. In relation wheezes and SCD, therapies for inflammation such as hydroxyurea are indicated [15]. As a result, it diagnostic methods are difficult to validate and other acoustic signatures to aid in wheeze differentiation may be necessary. However, due to new advances in computer-aided acoustical methods, namely the modified 1D waveguide presented in Chapter 2, used in conjunction with surface contact stethoscopic recordings together may be adapted to portable diagnostic devices that could be used to detect ACS more quickly than is currently possible, specifically predicting ACS at the onset of the prodromal phase.

3.2 THEORY

3.2.1 BREATHSOUND PATHOPHYSIOLOGY

Presented in chapter 2 are analytical models of sound propagation in 3D conducting airway trees insonified via the trachea. These models are categorized into one healthy and three pathological

states. While tracheal insonification is a good first step in modeling sound propagation, not all respiratory sounds are generated from the trachea downwards to the bronchioles, generating interest in expanding the current 1D waveguide model to accommodate non-trachea insonified acoustic sources. However, before the 1D waveguide can be modified, it is important to understand the physiology and pathophysiology of generated sounds in the airway tree.

Respiratory sounds have acoustic properties that are can be categorized between normal or abnormal (or adventitious). Normal breathsounds are defined by the sound generated in healthy airways and lungs by unenforced breathing. These breathsounds can be tracheobronchial (or airway breathsounds) or vesicular (in the thorax) [18], and the deficiency of healthy breathsounds (or manifestation of adventitious breathsounds) can be a hallmark of pulmonary disease. It is therefore of interest to understand the acoustics of how these breathsounds are generated and how the acoustics change under pathological states relative to healthy models; the analysis of acoustical properties of these patient sets can provide invaluable information in the pathophysiology of the lungs and airways [19].

Crackles. Crackles (or crepitations) are categorized with short, discontinuous, non-stationary sounds [19]. Crackles generate sound by the opening of closed airways; turbulent airflow effects caused by the re-equilibrium of pressure on a closed-off section of airways re-opening cause airway wall oscillatory motion, generating sound [20]. Although crackles generally happen in the inspiratory phase, they are known to occasionally occur during the expiratory phase [21]. Crackles are categorized into:

- Fine crackles, which include a shorter duration (5 ms), higher pitch (650 Hz), and are more stationary. Fine crackles originate in the basal part of the lung, are affected by body position change, but because of their origin in the basal part of the airways are not affected by coughing (long distance to the mouth);

- Coarse crackles, which include a longer duration (15 ms), lower pitch (350 Hz), and have no particular point of origin. The sound produced via coarse crackles is not affected by body position, but by coughing (suggesting it originates higher up in the airway tree);
- Biphasic crackles, which include elements of both fine and coarse crackles.

Crackles are associated with a variety of pathological lung and airway states, including chronic obstructive pulmonary disease (COPD), edema, bronchiectasis and fibrosis [19, 21-23].

Wheezes. Wheezes are continuous and adventitious breathsounds heard between the end of the inspiratory phase and start of the expiratory phase. Compared to crackles, which generate sound via sharp re-openings causing airway radial motion, wheezes are caused by the gradual re-opening (inspiration) and closing (expiration). This gradual opening and closure of airways (including 100-250 ms duration) creates a harmonic which generates wall radial motion. Wheezes can be heard from the mainstem bronchi (generation 2) down to 7 generations of airways [22]. The spectral content is wideband, from 100 Hz to 1 kHz, although some harmonics can go far beyond 1 kHz [24]. Theoretical models of wheezes incorporating flutter in flow-limited collapsible conduits show that the frequency of wheezing is affected by mechanical and geometrical properties including elasticity of the airways, thickness of the airway walls, and airway tension along (longitudinal) the airways [25].

Like crackles, wheezes can be high or low pitched. High pitched wheezes originate in the smaller airways, with coarse wheezes in the larger airways. In addition, wheezes can be monophonic (originating in one location) or polyphonic (originating in multiple locations at once). Whether the wheeze in low or high pitched, monophonic or polyphonic depends on the patient pathological state, and certain obstructive airway diseases including asthma and COPD are associated with certain types of wheezing [23-26].

Stidor. Stridor are continuous monophonic sounds that originate in the extra-thoracic airways, specifically the larynx and thoracic inlet, and are correlated with intense sounds occurring during the inspiratory phase due to airway collapse because of low internal lumen pressure. Although stethoscopic measurements can be used to identify stridor and localize its maximum intensity, stridor can be heard without any aid from instrumentation. Because of this, stridor are often considered to be an indication of upper airway obstruction. Signal analysis of stridor revealed a sinusodal waveform with a fundamental frequency typically higher than 500 Hz [19, 23].

Bronchial Breathsounds. Bronchial breathsounds are associated with blasting respiratory sounds audible throughout the respiratory cycle, resultant from a lack of air in lung tissue between the larger airways and chest wall likely a result of consolidated lung from pneumonia or pulmonary fibrosis. Bronchial breathsounds originate in the anterior section over the manubrium of the sternum and in the posterior section between the vertebrae T3 and C7. Bronchial breathsounds relative to normal bronchial respiratory sounds feature a higher spectral content due to airway consolidation causing a reduction in low-pass filtering of alveolar respiratory sounds. However, they are still difficult to diagnose due to their similarity to normal tracheal breathing respiratory sounds [23].

Pleural Rub. Pleural rubs include leathery, grating or creaking respiratory sounds, often localized over the posterior of the lung. They are stationary, often occurring in the same stage of the respiratory cycle during inspiration and expiration with the expiratory component specular to the inspiratory component with a duration of typically 200 ms and with spectral content around 200 Hz. Pleural rub is caused via friction between inflamed parietal and visceral surfaces of the pleura during breathing [23], and is considered an indicator of pleural inflammation or pleural tumors. If the pleural rub is limited to the inspiratory phase, it is almost indistinguishable to crackles.

Rochi. Ronchi are musical low-pitched sounds, with rapidly damping periodic waveforms with a duration greater than 100 ms and spectral content lower than 300 Hz. Ronchi are caused by

abnormal airway collapse via breaches of the mucous film covering the inner airway walls. Ronchi are clearly distinguishable when coughing, clinical studies indicating that mucous secretions in larger airways play a large role in the respiratory sounds, with ronchi on the whole being an indicator of thickening of the mucosa, bronchospasm and edema causing airway lumen constriction [23].

Squawks. Squawks are characterized by a crackle followed with a short musical respiratory sound resembling a wheeze, with a waveform consistent with wheezes preceded by a crackle with a mean duration of 90-320 ms [27]. Squawks are associated with pulmonary fibrosis and other related fibrotic disorders. Forgacs [28] suggested that the physiological events leading to a squawk include obstructed airways opening during inspiration, which then flutter during the respiratory cycle, which is physiologically consistent with a crackle and wheeze event happening in order [23, 27].

3.2.2 DIFFERENCES FROM INSONIFICATION TYPE MODELS

Presented in Chapter 2 section 2.2.3 is the groundwork and algorithmic rules for the modified 1D waveguide [16]. The 1D waveguide takes in a conducting tree model and outputs acoustic properties (typically) per segment. Interpolated measurements can be done to calculate the acoustic pressure up to the length of each segment via eqn 2.16.

With regards to breathsound simulation, there are two methods considered for modeling sound propagation in non-tracheal insonification sources. The first is arbitrary monopole placement, where a monopole source is approximated at any point in the tree. This simulation type has relevance with certain types of breathsounds, including wheezes and stridor where sound can propagate from a variety of sources from mucous coating the airways, causing airway flutter from turbulent effects of airflow. Another is terminal segment insonification, which approximates a crackle (or other similar breathsound), where sound is propagated from a terminal segment upwards mainly due to airway walls radial vibrations caused by rapid collapse and re-

opening of the airways due to airflow turbulence on inflamed airway walls, mimicking the physiological effects of breathsounds in lower airways. For the purposes of this dissertation, tracheal insonification models are referred to as insonification models and terminal segment insonification as breathsound models.

In insonification models, connectivity is ordered by a 2 point array of the proximal and distal point index (i.e. point 1 connecting to point 2 making a row element of [1 2]), with each face having a row element in the connectivity matrix with the number of rows corresponding to the number of segments in the conducting tree. In the recursive algorithmic step, where input impedances, terminal impedances and pressure ratios are calculated, this ordering of segments is important because when going upwards and downwards in the tree the order of proximal and distal points matters. If this order was reversed erroneously, the algorithm would either not run infinitely assuming a single segment was reversed, or if a series of connections were ordered incorrectly the algorithm would report acoustic properties for those segments from the distal to proximal end. Ordinarily, this would be an algorithmic input error in terms of the geometry and need to be corrected, but in monopole and breathsound models this can be used as an advantage.

The modified 1D waveguide was then modified further to incorporate breathsound analytical analysis. To do this, geometrical changes on top of algorithmic changes were made. The main problem originally inhibiting breathsound analysis via the 1D waveguide is that the algorithm runs on a recursive relationship between parent and daughter segments assuming that the acoustic inlet is a termination condition. There can be no sound propagation upstream as a result. It is possible to have up to three possible simulation cases for breathsounds including:

1. Monopole placement at a bifurcation, leading to two “downstream” trees and one “upstream” tree;
2. Monopole placement inside of a segment, leading to one “downstream” tree and one “upstream” tree;

3. Breathsound models, leading to no “downstream” trees and one “upstream” tree.

All changes outlined above can be defined as geometric changes and modifications to the 1D waveguide can be accomplished by 1) changing how the waveguide inputs geometry and 2) changing how the algorithm handles tree calculations.

To accomplish this, there were two changes to the modified 1D waveguide application. For clarity in this dissertation the further modified 1D waveguide will be called the 1D BS waveguide. The first deals with a change to the initialization step, and the second deals with breaking the recursive calculations into three, two or one step depending on the three possible simulation cases outlined above. In the initialization setup, acoustic inputs may be defined by either inputting a monopole location or by specifying a terminal segment for sound introduction. In either case, from that point up to the trachea, the connectivity of the segments will then be reversed via a new subroutine and saved into a new connectivity matrix. This geometric change is performed to “split” the way the 1D BS waveguide performs its calculations, which is captured in the next step. Per the three simulation cases outlined above, the 1D BS waveguide will then run independently three to two to one times. The 1D BS waveguide per iteration will treat the monopole simulation as a monopole approximation by treating the two (or one) downstream and upstream tree independently, using a planar wave input whose amplitude is defined by the user. In this manner, the acoustic properties of the full tree are divided into two or three partial subtrees with the iterative recursive calculations, which at algorithm finish are then stitched together so that every segment has its unique acoustic properties as per the modified 1D waveguide in Chapter 2. In this manner the model does not fully simulate a monopole source, but over a full conducting tree this is considered to be an adequate approximation as acoustic properties for the tree have such extensive dependence on a large number of segments. The BS simulation models do not require this step as the tree is solved identically to an insonification simulation case, with the changed

reversed geometry upstream to the trachea. Seen in Figure 3.1, is a depiction of the algorithmic process.

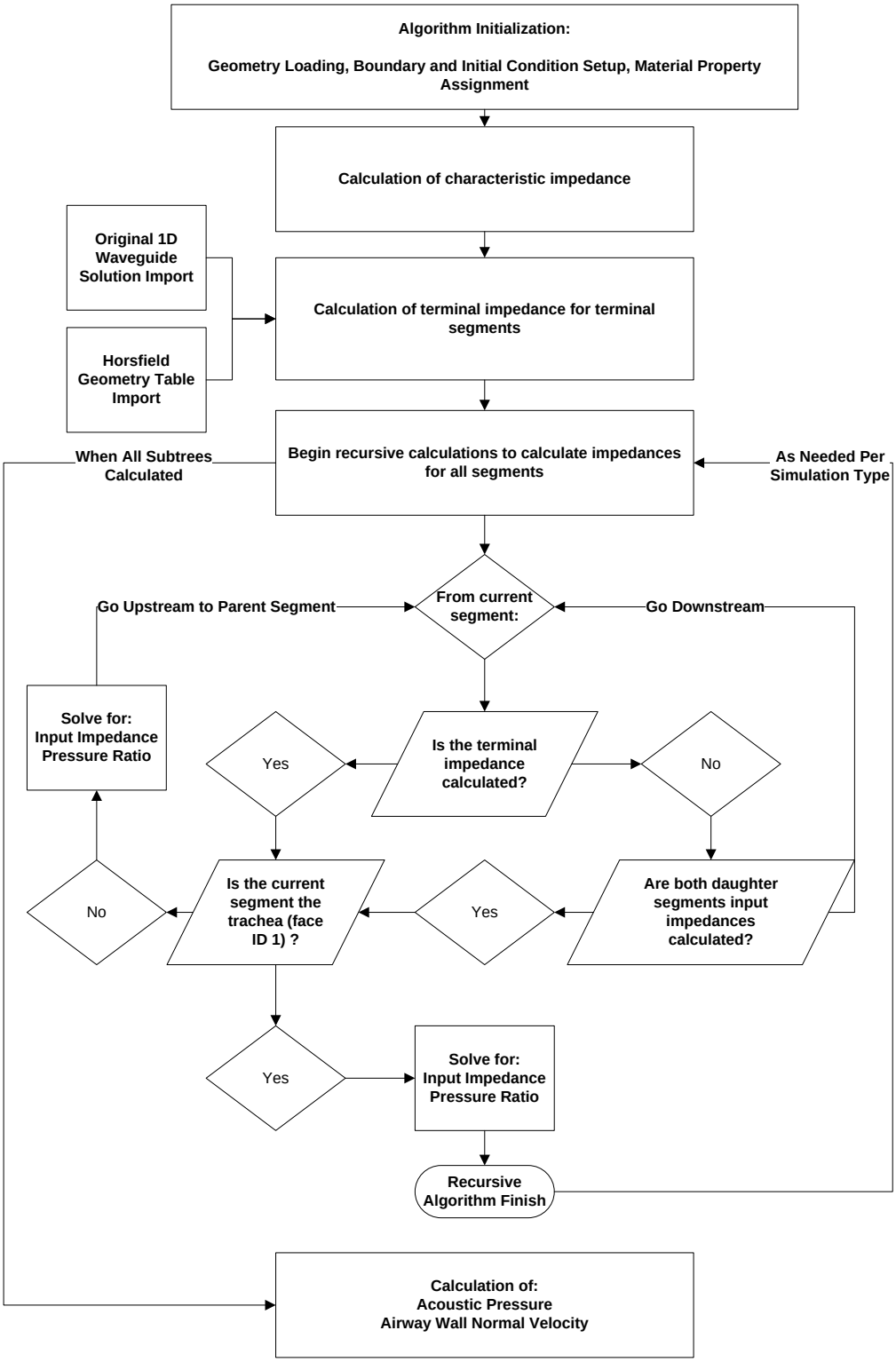

Figure 3.1. Algorithm Flowchart for 1D BS Waveguide.

3.2.3 TIME HISTORY RECONSTRUCTION FROM IMPULSE RESPONSE

The 1D BS waveguide maps the acoustic profile of the 3D conducting tree over a spectral range defined by the user. Furthermore, because the basis of the 1D waveguide is built on linear system theory, conversion to a time-domain analysis from a frequency response function (FRF) can be performed via linear system identification tools. In this dissertation, the System Identification Toolbox's n4sid command in MATLAB 2016a [17] was used on the FRF calculated via the 1D BS waveguide used in Section 3.2.1 to estimate the state-space model (or transfer function for impulse response). In this dissertation, the time history calculated via impulse was calculated using the "impulse" command to model a wheeze, but the same transfer function can alternatively be convoluted with the acoustic time history for non-crackle breathsounds to model other breathsounds of interest including wheezes or stridor. Because of the crackle's sharp onset time response (the fine crackle's 5 ms duration loosely representing an impulse) it was chosen as a simulation case applicable for the time history reconstruction.

3.3 AUSCULTATIVE METHODOLOGY AND STUDIES

After receiving Institutional Review Board approval, 76 adult human subjects (37.5 ± 12.4 years) with SCD were recruited from the adult sickle cell clinic from the University of Illinois Hospital and Health Sciences System. The criteria for ACS used for patient selection was categorized by three clinical criteria: a temperature greater than 38^0C, identification of one or additional radiodensities during an acute respiratory episode on a chest roentgenogram, and decreased oxygen saturation along with and increased respiratory rate in the patients' medical record. Measurements were taken during a routine visit after admission to the Acute Care Center for hospitalization. Subjects used in this study were diagnosed with sickle hemoglobinopathy, were at least 18 years old and were given informed consent. Auscultative measurements and assessment were performed using

digital stethoscopes (Littman Model 3200), on a total of 12 sites on the chest (anterior and posterior sections), for at least 2 breaths/cycle, with the stethoscope in direct contact with the skin during the complete respiratory cycle. The specific sites for measurement were over the left and right lungs, over the upper, middle and lower regions. Analysis of auscultation measurements was performed in MATLAB [17]. Frequency plots were created via the “pwelch” command.

While all patients were analyzed, two patients are highlighted in the post-processing analysis with both a baseline and during-hospitalization for ACS set of measurements. Figure 3.2 depicts spectral measurements for these patients a few days before diagnosis ACS. Figure 3.3 depicts spectral measurements for these patients after resolution of ACS. Also shown is the average of all 76 patients for the same locations when they did not have confirmed ACS, with one standard deviation, to highlight the general acoustic trend with inter-patient variance.

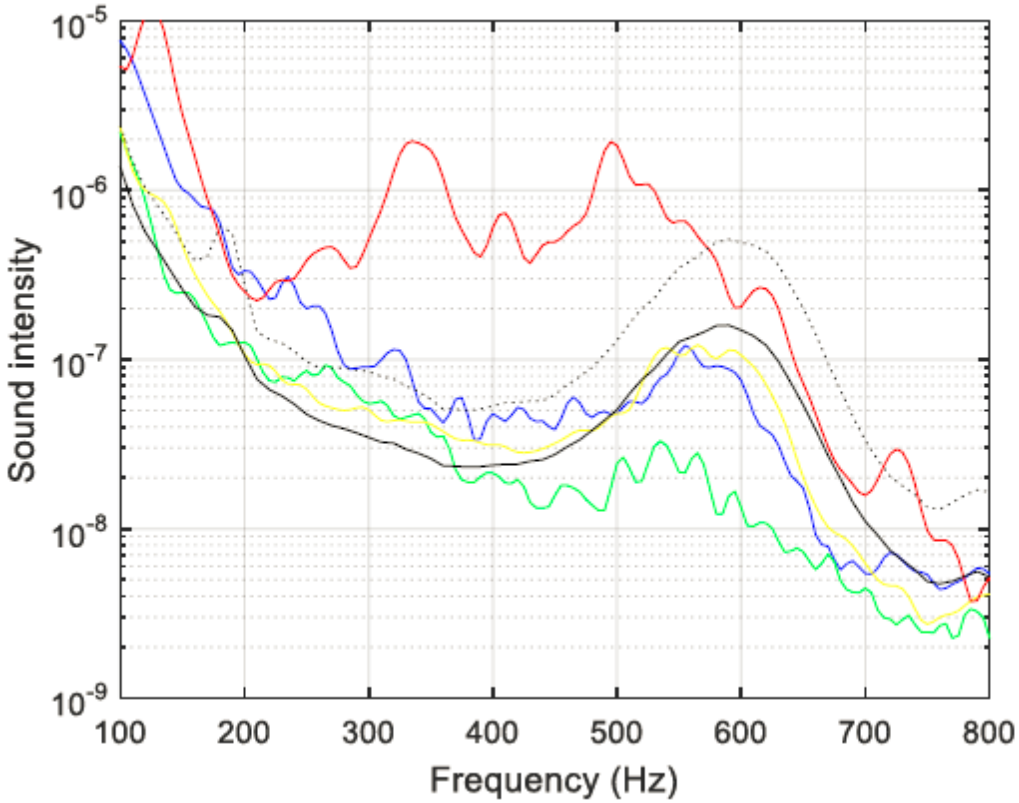

Figure 3.2. Patient 1. Spectral content of breath sounds over posterior middle right (PMR) lung field of confirmed ACS location in a patient. Spectra calculated based on Welch's method and measured on days 4 (blue), 3 (yellow), 2 (red) before the clinical diagnosis of ACS and 20 days (green) after diagnosis when patient sent home, considered as this patient's baseline. Black solid and dashed lines are the averaged baseline value and averaged baseline plus one standard deviation of the spectrum of the same measurements taken on 69 different sickle cell patients not undergoing ACS.

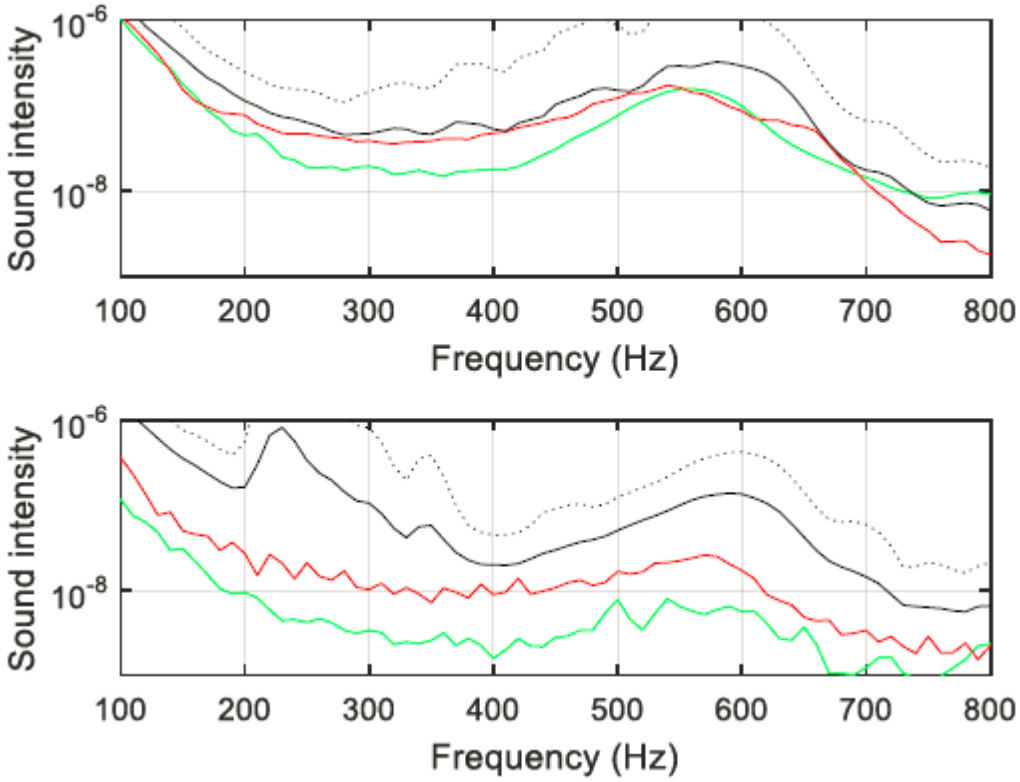

Figure 3.3. Human Subject #2. Spectral content of breath sounds over anterior and posterior base left lung fields (ABL and PBL, respectively) of confirmed ACS in a patient. Spectra calculated based on Welch's method and measured 1 day before (red) the clinical diagnosis of ACS and 1 month prior (green) to the ACS diagnosis, considered as this patient's baseline. Black solid and dashed lines are the averaged baseline value and averaged baseline plus one standard deviation of the spectrum of the same measurements taken on 69 different sickle cell patients not undergoing ACS.

3.4 MODELING ACOUSTIC PROPAGATION IN BREATHSOUND MODELS

3.3.1 1D WAVEGUIDE SIMULATION MODELS FOR BREATHSOUND

Three simulation cases were created for breathsound analysis. The first breathsound model included an approximated monopole source at the distal end of the left mainstem bronchi (LMB), at the site of bifurcation, with material properties identical to those shown in Table 2.1. This simulation model can approximate the way sound is generated via stridor caused by a partial occlusion of the mainstem bronchi, however further study needs to be performed to check the material, geometry and boundary condition changes relevant to stridor. In this model, the acoustic profile was calculated via the 1D BS waveguide, the full acoustic map stitched together after three iterative recursive calculations. The acoustic profile was broadband, mapped over 1 Hz to 3600 Hz in 1 Hz increments, although for the ease of presentation results for 400 Hz is shown in this section for relevance in respiratory sounds and applicability in dynamic elastography test methods. The mapped acoustic pressure in a partial 3D conducting model with an approximate monopole source can be seen in Figure 3.4 down from the trachea to Horsfield Order 10.

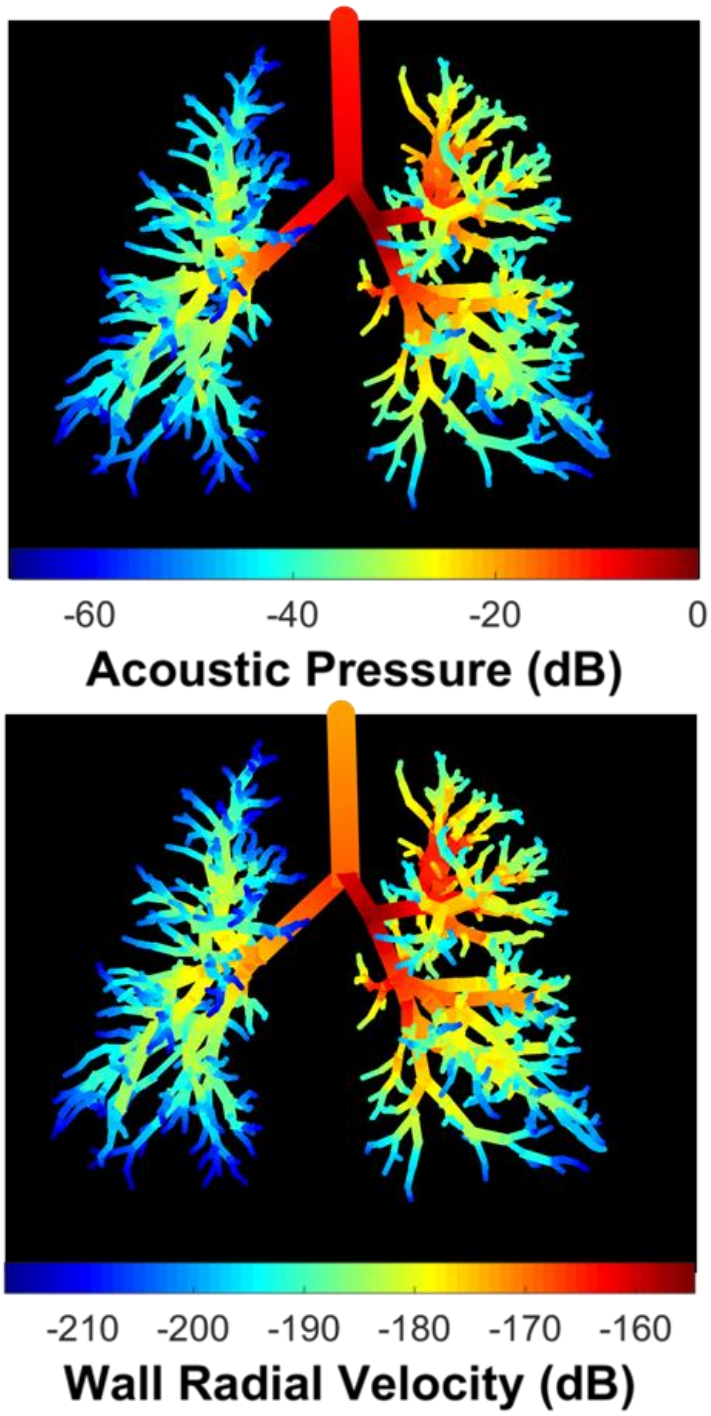

Figure 3.4. Acoustic pressure (ref. 1 Pa) and wall radial velocity in dB (ref. 1 m/s) at 400 Hz in partial conducting tree models for monopole approximation simulation model located in RMB. Monopole was located at the distal end of the LMB.

The second simulation case included a BS in the lower left lobe, with material properties identical to those shown in Table 2.1. This simulation model was created to model a wheezeoccurring in the lower left lobe at a segment randomly chosen to the last terminal segment in the connectivity matrix exclusive for that lobe with spectral content from 1 Hz to 3600 Hz in 1 Hz increments. However, one important distinction to note is that there is no physiological basis for a “healthy” wheeze breathsound model: there would be no wheeze in a healthy individual. This simulation mode was included to provide distinction to a physiologically relevant wheeze case modeled with pulmonary infiltrate. In this model, a planar wave was introduced at the distal end of the segment (which after connectivity reversing was considered the proximal end). Additionally, in this simulation model, as only a single tree was recursively calculated there was no need to run the 1D BS waveguide iteratively. The mapped acoustic pressure at 400 Hz in the 3D conducting model for a wheeze can be seen in Figure 3.5.

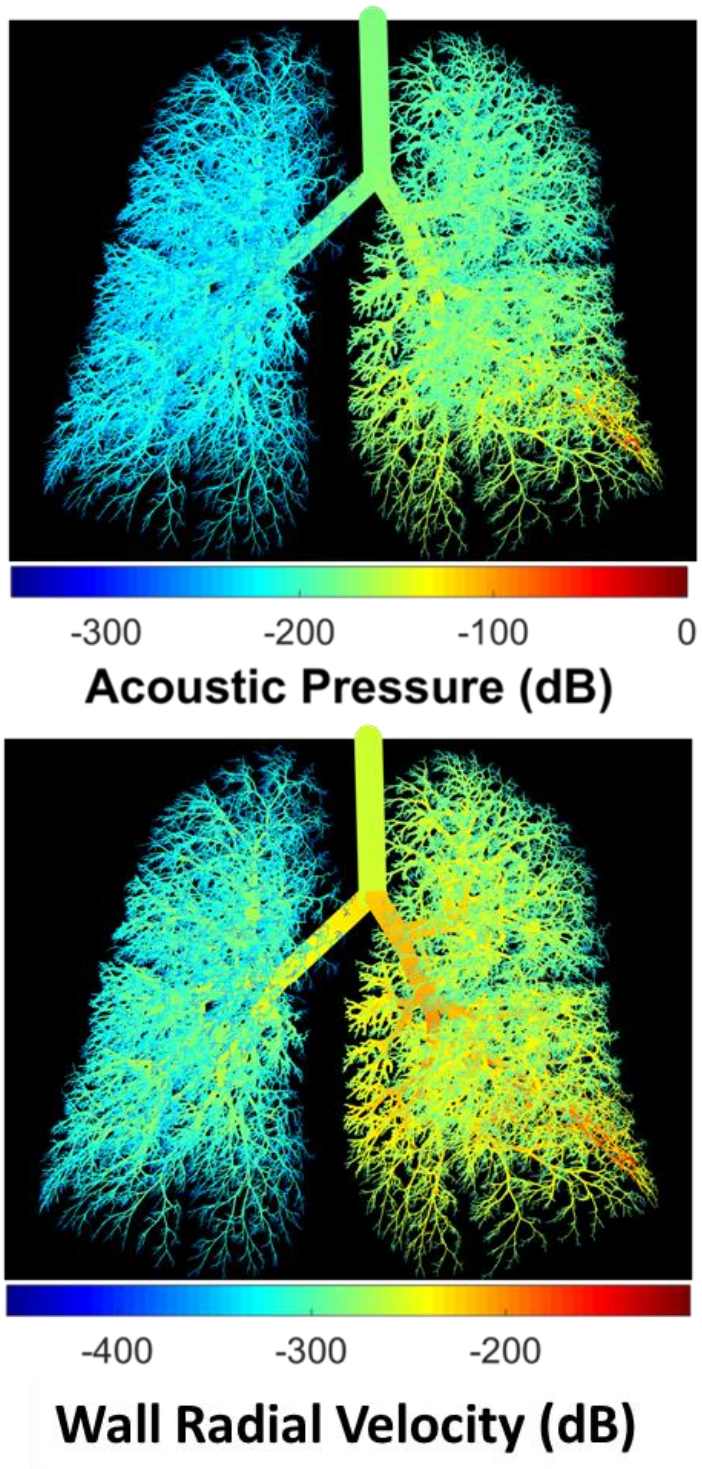

Figure 3.5. Acoustic pressure (ref. 1 Pa) and wall radial velocity in dB (ref. 1 m/s) at 400 Hz in full conducting tree models for wheeze representative simulation model without PI.

The final simulation case consisted of a wheeze BS in the lower left lobe, with material properties identical to those shown in Table 2.1, but with a pulmonary infiltrate in the lower left lobe following the boundary condition changes for PI in Section 2.4.3. This simulation case was made to model a wheeze produced via PI, from a single terminal segment in the lower left lobe afflicted with PI and with spectral content from 1 Hz to 3600 Hz in 1 Hz increments. Additionally, in this simulation model, as only a single tree was recursively calculated there was no need to run the 1D BS waveguide iteratively. The mapped acoustic pressure in the 3D conducting model at 400 Hz for a wheeze in a lobe afflicted with PI can be seen in Figure 3.6.

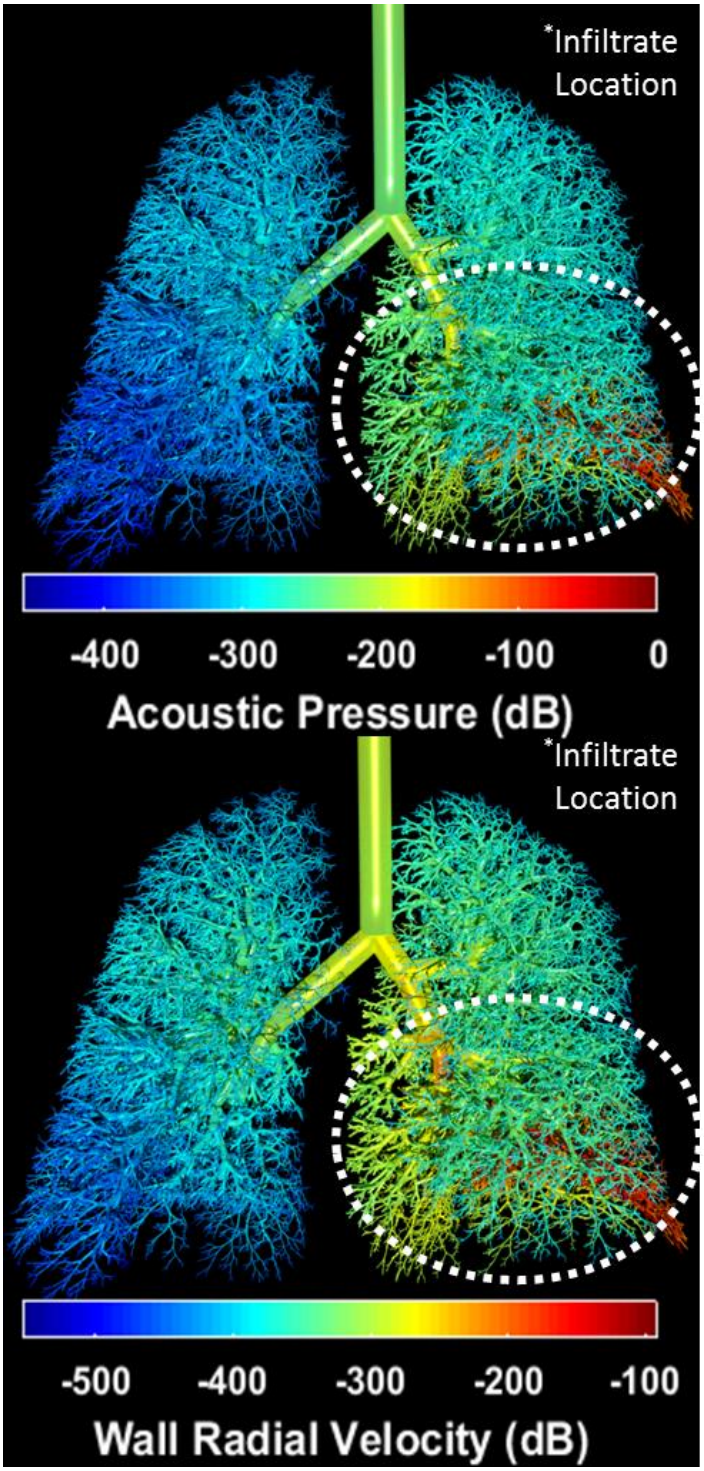

Figure 3.6. Wall radial velocity in dB (ref. 1 m/s) at 400 Hz in full conducting tree models for wheeze simulation model.

The acoustic pressure in dB (ref. 1 Pa) and wall radial velocity in dB (ref. 1 m/s) of the healthy wheeze model and wheeze BS model can be seen in Figure 3.7.

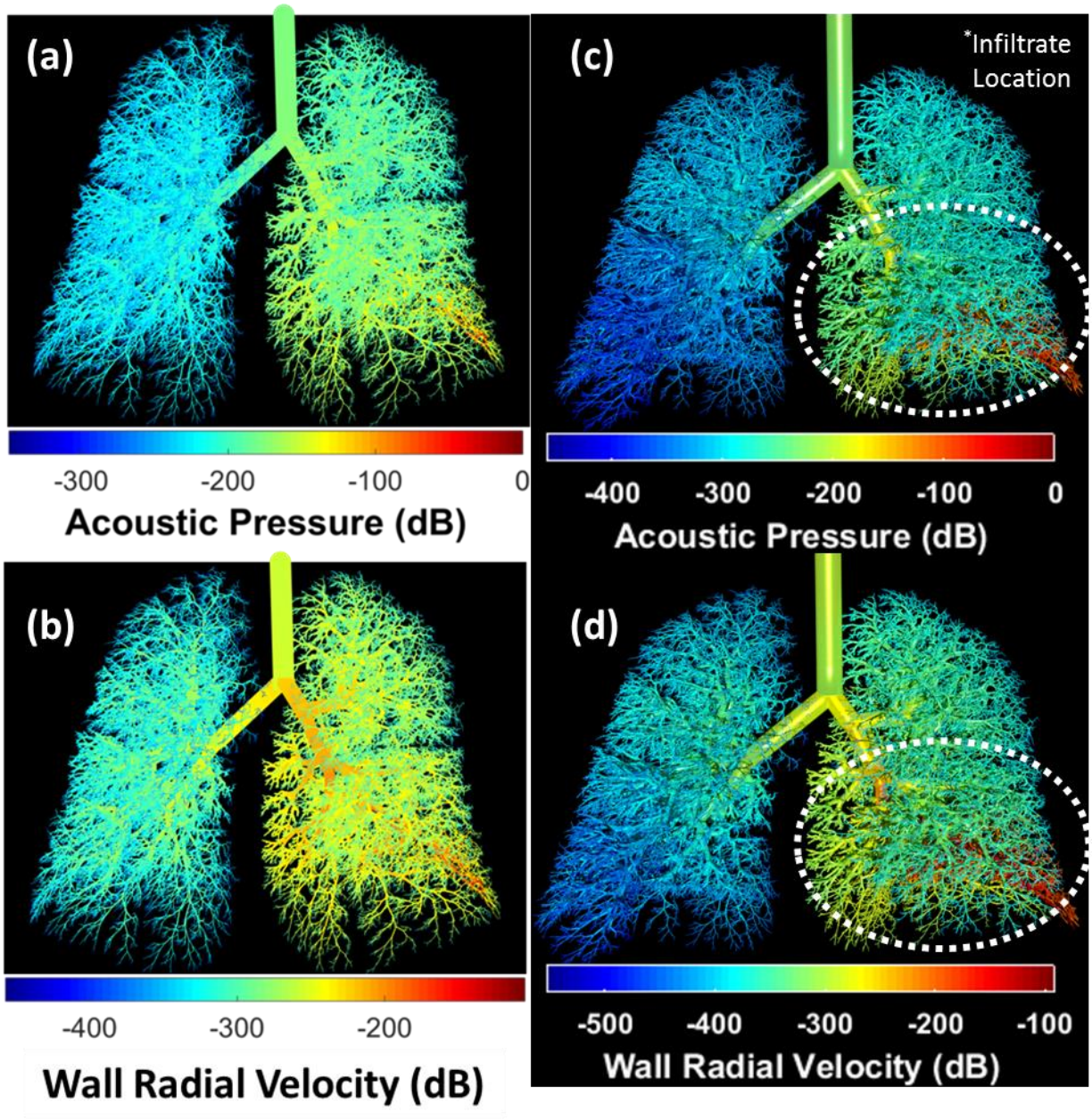

Figure 3.7. Acoustic pressure in dB (ref. 1 Pa) for (a) healthy wheeze model and (c) wheeze BS simulation model and wall radial velocity in dB (ref. 1 m/s) for (b) healthy wheeze model and (d) wheeze BS simulation model.

The acoustic pressure in dB (ref. 1 Pa) and wall radial velocity in dB (ref. 1 m/s) of the insonification PI model and crackle BS model can be seen in Figure 3.8.

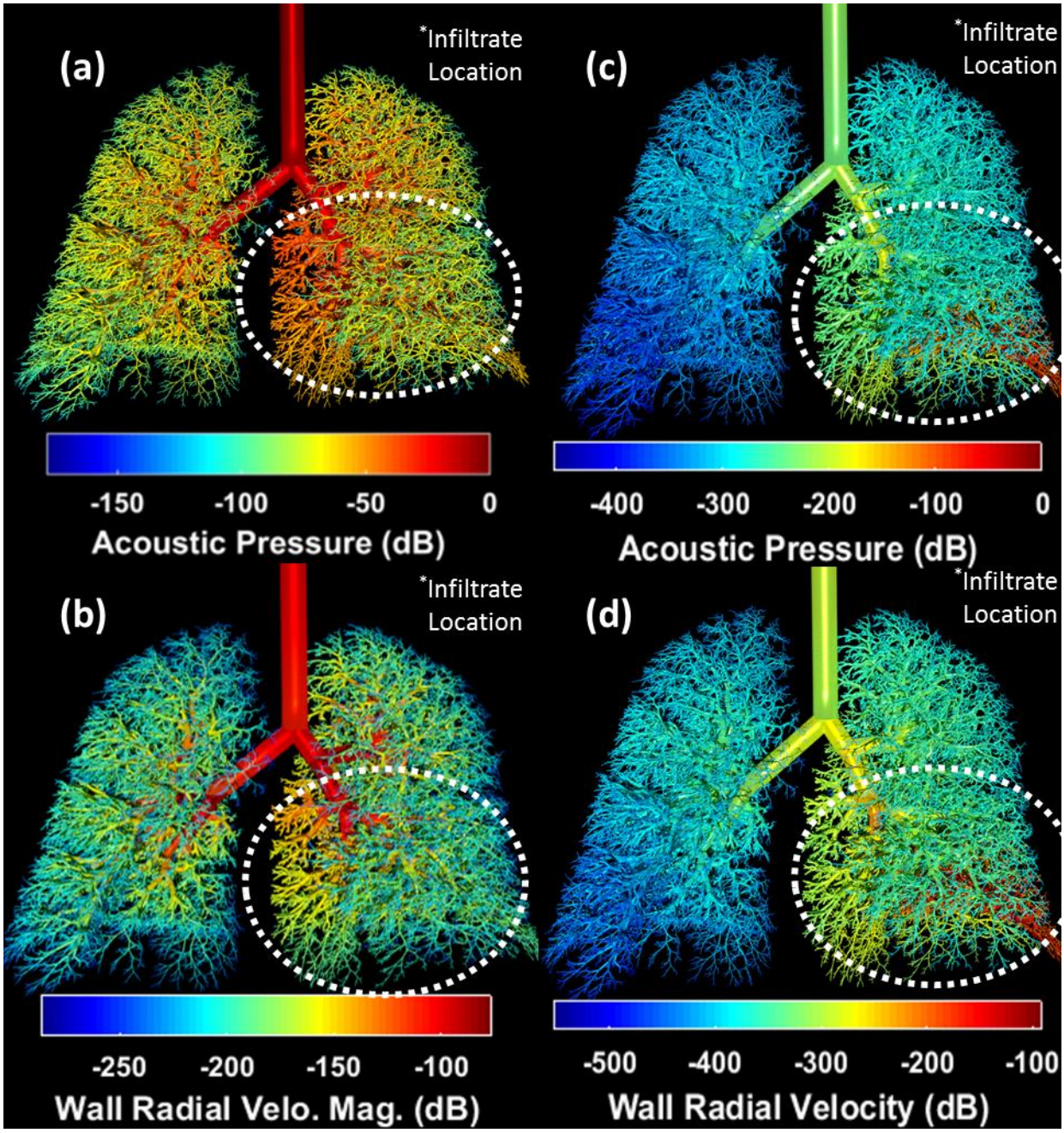

Figure 3.8. Acoustic pressure in dB (ref. 1 Pa) for (a) insonification PI model and (c) wheeze BS model and wall radial velocity in dB (ref. 1 m/s) for (b) insonification PI model and (d) wheeze BS model.

3.5 TIME HISTORY RECONSTRUCTION OF WAVE PROPAGATION

3.4.1 TIME HISTORY RECONSTRUCTION FROM IMPULSE RESPONSE

Two FRFs calculated from an insonification model and a BS model with pulmonary infiltrate presented in Section 3.3.1. These FRFs were converted to a time-domain estimation of the acoustic pressure, with the time domain sound source including a sharp pulse, the time reconstruction BS model is a crackle model. Both models were broadband with spectral content from 1 Hz to 3600 Hz in 1 Hz increments in order to estimate an impulse response function as accurately as possible. The acoustic pressure pulse was mapped from the acoustic inlet to a predefined outlet on a segment to segment basis, meaning every segment from inlet to outlet was mapped. In the insonification model, the inlet was the trachea and the outlet was the terminal segment chosen in the BS model. In the crackle PI BS model, the inlet was the terminal segment acoustic source and the outlet was the trachea. Each segment was estimated to a transfer function via the “n4sid” command in MATLAB. For all models, a range from 1 to 100 states was calculated in order to provide an optimal transfer function estimate, in order to fit the FRF as accurately as possible. For the insonification model the transfer function estimate had a mean fit value of 96.61% with a standard deviation of 3.37%, whereas the crackle model had a mean fit value of 92.35% with a standard deviation of 13.33%.

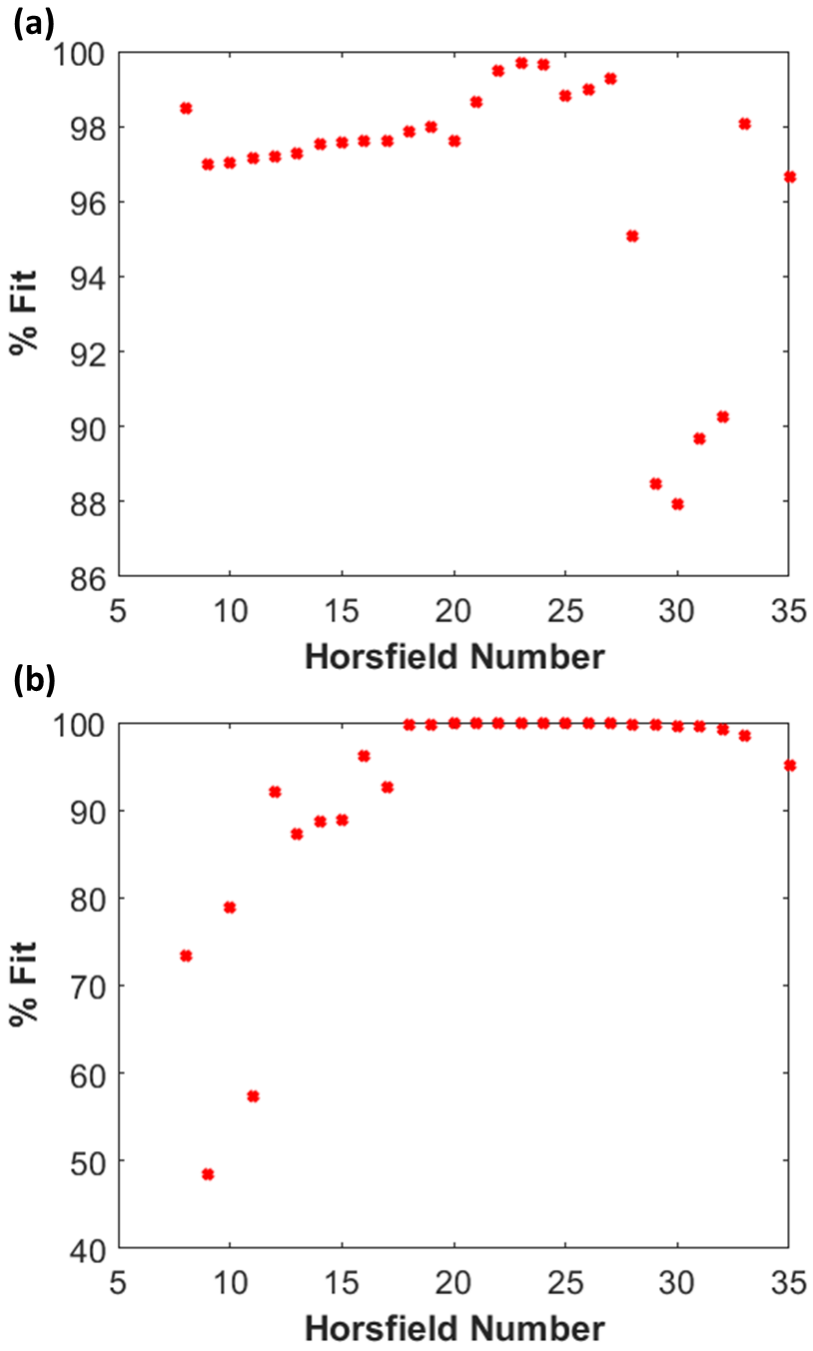

Figure 3.9. Impulse response function fit values for (a) insonfication model, and (b) crackle BS model.

The time history for each segment from inlet to outlet was then calculated with the “impulse” command in MATLAB. An acoustic pressure pulse was approximated by treating the input acoustic source as an impulse, and the time history reconstruction calculated via the impulse

response function was pieced together from two independent calculations, one from 0 to 0.1 s in 1 x 10^{-7} s increments, and from 0.1 to 1s in 1 x 10^{-3} s. Figure 3.10 shows the time history reconstruction of the acoustic pressure pulse for the insonification model.

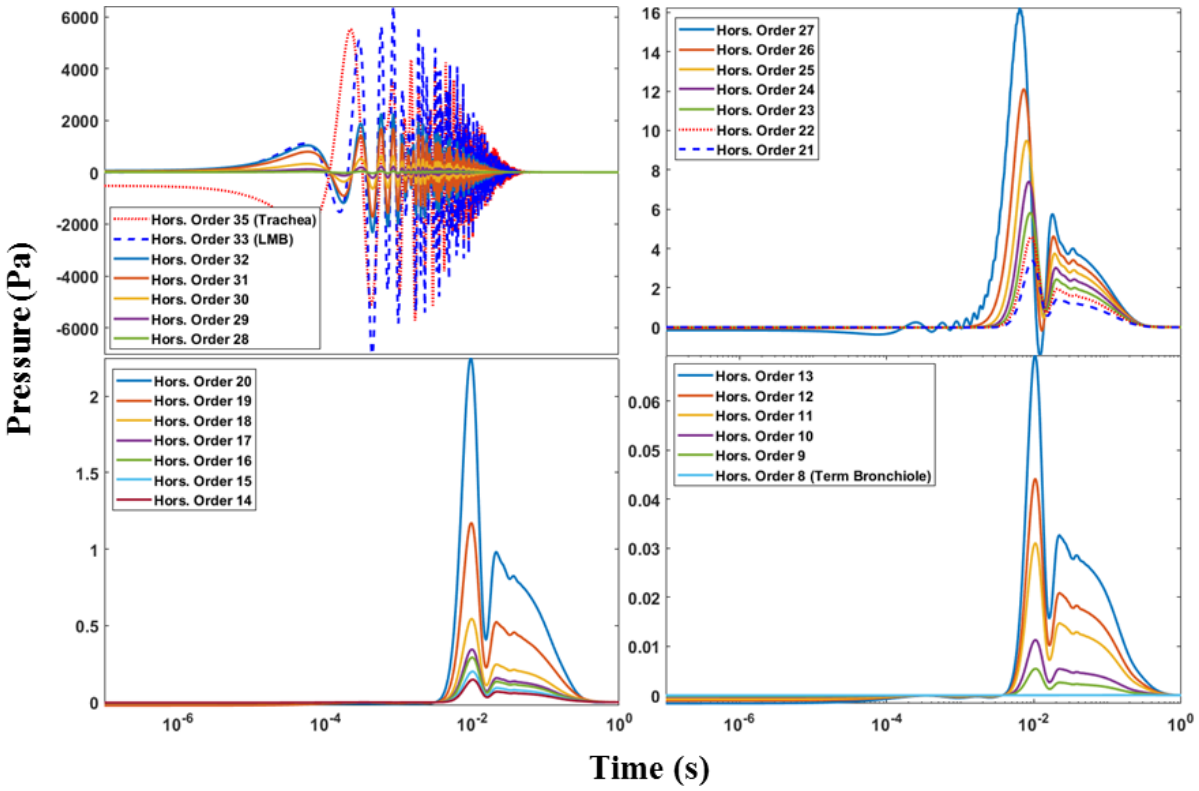

Figure 3.10. Time history reconstruction of the acoustic pressure pulse for the insonification model, from the trachea (source) to terminal bronchiole (outlet).

Figure 3.11 shows the time history reconstruction of the acoustic pressure pulse for the crackle BS model.

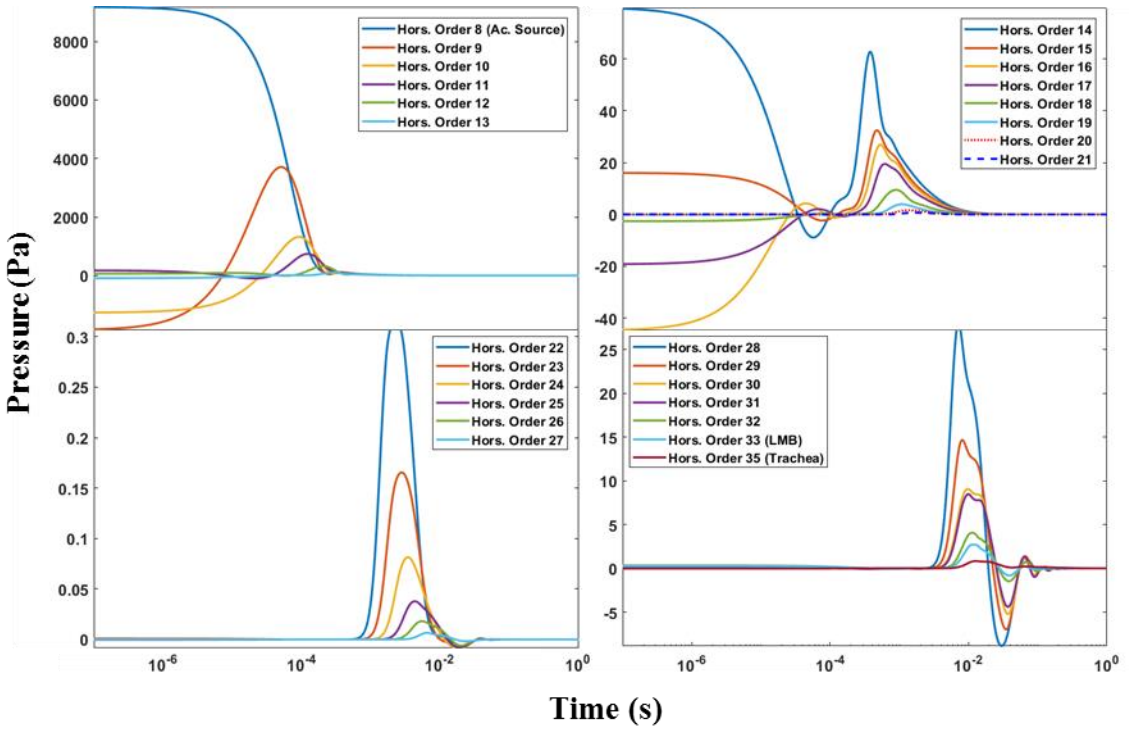

Figure 3.11. Time history reconstruction of the acoustic pressure pulse for the crackle BS model, from the terminal bronchiole (source) to trachea (outlet).

3.6 DISCUSSION

Analysis of the experimental data presented in Figures 3.2 and 3.3 suggests, but does not rigorously prove, that breathsounds during an episode of ACS and after the episode contain quantitative differences that, when analyzed, may serve as an early marker for the development of ACS. If we consider the mean values of the baseline and ACS spectra from 200 – 500 Hz for human patients 1 and 2 in Figures 3.2 and 3.3, we find the mean ratio of ACS to baseline to be about 7, but with a standard deviation of 7. The paired, equal variance student's t-test yields a two-tailed p value of 0.21. If we were to maintain the same mean ratio and standard deviation with increasing samples, then n = 7 cases would be sufficient to establish significance based on the standard criterion of $p < 0.05$. Therefore, further study with improved signal analysis is necessary to determine the relationship between ACS and breathsounds.

While it has been proposed that small airway flutter (wheezes) and collapse/opening (crackles) are associated with ACS and better understanding of the acoustical coupling of the airway walls, organs in the thoracic cavity and chest, quantifying acoustical properties associated with these breathsounds has proven to be difficult. Modifications to the 1D waveguide are used to produce a range of breathsound simulations, allowing for acoustic sources including approximated monopole sources and non-tracheal insonified sources. Use of the 1D BS waveguide allows for analytical modeling of small airway diseases that normally are difficult to experimentally measure. Figure 3.4 shows the acoustic profile of a partial conducting tree with an acoustic source located at the distal end of the LMB. While no studies at present were conducted for these simulation models in this dissertation, these monopole models can represent both stridor BS and others that occur within parts of the airway tree. With modifications to the airways mechanical and geometric properties, representing physiological disease progressive states for crackles and wheezes, the 1D BS waveguide shows potential to calculate the acoustic profile, and quantitative analysis of the differences between progression states can provides possible diagnostic applications in early-onset detection of crackles and wheezes.

In Figure 3.5, a healthy wheeze model with broadband spectral content is presented. Additionally, in Figure 3.6, a wheeze BS model is presented. Visual comparison in Figure 3.7 shows a larger average acoustic pressure in downstream airways for the healthy wheeze relative to the wheeze BS model. This can be attributed to the higher impedances in the wheeze model as a result of the PI boundary conditions: by making the terminal impedances of the LL lobe infinite, the impedances in the left lung are correspondingly larger, increasing attenuation because of the larger impedance mismatches associated with the PI boundary conditions. Moreover, the magnitude of acoustic pressure and wall radial velocity in the right lung is 100 dB larger in magnitude. Although intensities of pressure and velocity at -300 dB are virtually negligible, a 100

dB difference is significant, which provides evidence to the point that introduction of PI into the LL lobe has profound effects on the acoustic profile.

In Figure 3.8, analysis between an insonified model with PI and a wheeze BS model is shown. In the LL lobe of the insonified PI model, there was a significant increase in the mean terminal airway acoustic pressure and wall radial velocity, over a wide spectral range. This is consistent with broadband increases of acoustic signals associated with ACS. Visual detection shows profound differences in attenuation of sound between the two modes of sound excitation: a 350 dB difference in minimum acoustic pressures and wall radial velocity. Moreover, sound attenuates in greater magnitude as the sound heads upstream in the wheeze model: the model only has the local area around the source having a significant acoustic pressure and wall radial velocity. Sound propagation has a large effect with where the sound is introduced into the tree: from trachea to terminal bronchioles, the airways decrease in radial size and (typically) decreasing in length. The cartilage fraction also decreases along with wall thickness. This is almost the opposite for the wheeze model heading upstream to the trachea. The rapid changes in impedances heading upstream result in more significant impedance mismatches early on, as the source is located in the LL lobe in close proximity to the neighboring segments with the hard sound boundary condition. As a result, sound attenuates much earlier in the tree relative to the insonification model; as sound propagates from the trachea into the mainstem bronchi, one of the lungs have no change in material properties, geometry or boundary conditions.

Temporal response simulations shown in Figures 3.10 and 3.11 for insonification and crackle BS models may be useful in the development and optimization of source localization studies. Shown in the figures are graphical depictions of how sound attenuates over time per segment bifurcation. Fit estimates of the FRF transfer function used to calculate the impulse response function can be seen in Figure 3.9. In the source segment, and several downstream generations, the transfer function showed poor fit values, possible as a result of wider variability of the

broadband acoustic pressure and wall radial values. Sharper resonant peaks and wider variable ranges resulted in more difficulty while fitting; this wide broadband variability in acoustic parameters was much less pronounced in downstream airway segments due to sound attenuation lessening the sharpness of the resonant peaks and troughs, which were much easier to fit.

Combining improved quantitative assessment of acoustic parameters, which can indicate disease severity, and source localization based on computer models can lead to better diagnostic applications of breathsounds, as well as accelerate research on the topic. Mobile health (mhealth) via acoustical methods can be fast, efficient, and cheap, and provide possible early-onset detection of ACS for people who suffer from SCD, as well as other pulmonary pathologies.

3.7 FUTURE WORK

The breathsound and monopole approximation additions to the 1D modified waveguide show considerable promise in terms of analytical modeling of sound propagation in the airways that include non-tracheal insonified sources. Avenues of improvement can be divided into two areas: algorithmic changes and future studies. In terms of algorithm improvements, the iterative steps of recursive calculations in the 1D BS waveguide are independent of each other and can be done in parallel. Moreover, identification of monopole source locations right now is currently done through visual inspection of the tree, with the segment manually defined where the monopole will be located. Tree characterization techniques can be applied to better differentiate the conducting models based on parent-daughter connectivity starting with the trachea, to identify major branches where breathsounds commonly reside in. In terms of studies, the breathsound models in this dissertation were limited to a single crackle model with a pulmonary infiltrate, compared against non-breathsound models. Breathsounds models and simulations can be created for other breathsounds including wheeze, stridor, pleural rub, ronchi and squawks, all of which contain acoustic properties that can analyzed experimentally and compared analytically.

Currently, the transfer functions used in the impulse response function are done via the “n4sid” command in MATLAB. For the inlet segments, where the acoustic wave has the highest energy and the greatest amount of terminal impedance, the transfer function fitting parameter decreases significantly, rising over time. Better estimation of the transfer function fit can lead to better time history reconstructions of the acoustic pulse, which in turn allows for more accurate comparison and predictions of acoustic properties.

Additionally, current methodology of time history reconstructions of the acoustic pulse of current breathsound analytical models are limited to impulse response functions. Wheezes have pathological relevance in SCD as an indicator for disease stage and progression, but cannot be analytically modeled currently using impulse response functions because of their long duration. Convoluting the transfer functions calculated in Section 3.2.2 with a time history relevant to wheezes to reconstruct the acoustic pulse can lead to analytical models of wheezes. These analytical models can be analyzed to find patterns of disease progression, which provides potential early-onset diagnostic applications for ACS.

Finally, validation of the algorithm can be performed to assess algorithm accuracy by comparing it vs numerical or experimental studies. Although validation of the 1D waveguide was presented in Chapter 2.4.1, the validation was performed to assess how the algorithm compares in insonification studies. Monopole and BS simulations via the 1D BS waveguide can be verified numerically and/or experimentally, and further validation of the algorithm can provide validity to the analytical backbone presented in this dissertation.

REFERENCES

[1] Weatherall, D.J., “The inherited diseases of hemoglobin are an emerging global health burden,” *Blood,* vol. 115, no. 22, pp. 4331-6, 2010.

[2] Platt, O. S., D. J. Brambilla, W. F. Rosse, P. F. Milner, O. Castro, M. H. Steinberg, and P. P. Klug. “Mortality in sickle cell disease. Life expectancy and risk factors for early death,” *N. Engl. J. Med.,* vol. 330, no. 23, pp. 1639-44, 1994.

[3] Quinn, C. T., Z. R. Rogers, T. L. McCavit, and G. R. Buchanan. “Improved survival of children and adolescents with sickle cell disease,” *Blood,* vol. 115, pp. 3447-3452, 2010.

[4] Brousseau, D. C., P. L. Owens, A. L. Mosso, J. A. Panepinto, and C. A. Steiner. “Acute care utilization and rehospitalizations for sickle cell disease,” *JAMA*, vol. 303, no. 13, pp. 1288-94, 2010.

[5] Charache, S., J. C. Scott, and P. Charache. “Acute chest syndrome in adults with sickle cell anemia. Microbiology, treatment, and prevention,” *Arch Intern Med*., vol. 139, no. 1, pp. 67-9, 1979.

[6] Castro, O., D. J. Brambilla, B. Thorington, C. A. Reindorf, R. B. Scott, P. Gillette, J. C. Vera, and P. S. Levy. “The acute chest syndrome in sickle cell disease: incidence and risk factors. The Cooperative Study of Sickle Cell Disease,” *Blood*., vol. 84, no. 2, pp. 643-9, 1994.

[7] Paul, R. N., O. L. Castro, A. Aggarwal, P. A. Oneal. “Acute chest syndrome: sickle cell disease,” *Eur. J. Haematol.*, vol. 87, no. 3, pp. 191-207, 2011.

[8] Bartolucci, P., A. Habibi, M. Khellaf, F. Roudot-Thoraval, G. Melica, A.-S. Lascaux, S. Moutereau, S. Loric, O. Wagner-Ballon, J. Berkenou, A. Santin, M. Michel, B. Renaud, Y. Lévy, F. Galactéros, and B. Godeauc. “Score predicting acute chest syndrome during vaso-occlusive crises in adult sickle-cell disease patients,” *EBioMedicine*., vol. 10, pp. 305–311, 2016.

[9] Mekontso Dessap, A., J. F. Deux, A. Habibi, N. Abidi, B. Godeau, S. Adnot, C. Brun-Buisson, A. Rahmouni, F. Galacteros, B. Maitre. “Lung imaging during acute chest

syndrome in sickle cell disease: computed tomography patterns and diagnostic accuracy of bedside chest radiograph," *Thorax*, vol. 69, no. 2, pp. 144-51, 2014.

[10] Taylor, C., F. Carter, J. Poulose, S. Rolle, S. Babu, and S. Crichlow. "Clinical presentation of acute chest syndrome in sickle cell disease," *Postgrad. Med. J.*, vol. 80, no. 944, pp. 346-9, 2004.

[11] Cohen, R. T., A. Madadi, M. A. Blinder, M. R. DeBaun, R. C. Strunk, and J. J. Field. "Recurrent, severe wheezing is associated with morbidity and mortality in adults with sickle cell disease," *Am. J. Hematol.*, vol. 86, no. 9, pp. 756-61, 2011.

[12] Sobota, A., D. A. Graham, M. M. Heeney, E. J. Neufeld. "Corticosteroids for acute chest syndrome in children with sickle cell disease: variation in use and association with length of stay and readmission," *Am. J. Hematol.*, vol. 85 pp. 24–8, 2010.

[13] Strouse, J. J., C. M. Takemoto, J. R. Keefer, G. J. Kato, and J. F. Casella. "Corticosteroids and increased risk of readmission after acute chest syndrome in children with sickle cell disease," *Pediatr. Blood. Cancer.*, vol. 50, pp. 1006–12, 2008.

[14] Morris, C. R. "Asthma management: reinventing the wheel in sickle cell disease." *Am. J. Hematol.,* vol.84, pp. 234-41, 2009.

[15] Knight-Madden, J., and A. Greenough. "Acute pulmonary complications of sickle cell disease," *Paediatric. Resp. Rev.*, vol. 15, pp. 13–16, 2014.

[16] B. Henry and T. Royston, "A multiscale analytical model of bronchial airway acoustics," *J. Acoust. Soc. Am.*, vol. 142, no. 4, pp. 1774-1783, 2017.

[17] MATLAB, Version 9.0.1 (The MathWorks Inc., Natick, MA, 2016a).

[18] M. Bahoura, "Pattern recognition methods applied to respiratory sounds classification into normal and wheeze classes," *Comput. Biol. Med.*, vol. 39, no. 9, pp. 824–843, 2009.

[19] S. Reichert, R. Gass, C. Brandt, and E. Andrès, "Analysis of respiratory sounds: state of the art.," *Clin. Med. Circ. Respirat. Pulm. Med.*, vol. 2, pp. 45–58, 2008.

[20] J. Fredberg and S. Holford, “Discrete lung sounds: crackles (rales) as stress-relaxation quadrupoles.,” *J. Acoust. Soc. Am.*, vol. 73, pp. 1036–1046, 1983.

[21] P. Piirila and A. R. A. Sovijarvi, “Crackles: Recording, analysis and clinical significance,” *Eur. Respir. J.*, vol. 8, no. 12, pp. 2139–2148, 1995.

[22] A. Bohadana, G. Izbicki, and S. S. Kraman, “Fundamentals of lung auscultation.,” N. *Engl. J. Med.*, vol. 370, no. 8, pp. 744–51, 2014.

[23] Z. Wang, S. Jean, and T. Bartter, “Lung sound analysis in the diagnosis of obstructive airway disease,” *Respiration*, vol. 77, no. 2, pp. 134–138, 2009.

[24] B. A. Reyes, S. Charleston-Villalobos, R. Gonzalez-Camarena, and T. Aljama-Corrales, “Analysis of discontinuous adventitious lung sounds by Hilbert-Huang spectrum.,” *Annu. Int. Conf. IEEE Eng. Med. Biol. Soc.*, vol. 2008, pp. 3620–3, 2008.

[25] H. Pasterkamp, S. S. Kraman, and G. R. Wodicka, “State of the Art Advances Beyond the Stethoscope,” *Am. J. Respir. Crit. Care Med.*, vol. 156, no. 3, pp. 974–987, 1997.

[26] S. A. Taplidou and L. J. Hadjileontiadis, “Wheeze detection based on time-frequency analysis of breath sounds,” *Comput. Biol. Med.*, vol. 37, no. 8, pp. 1073–1083, 2007.

[27] D. U. Silverthorn, Human Physiology - An integrated approach. 2010.

[28] P. Forgacs, Lung Sounds. 1978.

CHAPTER 4

BOUNDARY ELEMENT AND SOURCE LOCALIZATION

4.1 INTRODUCTION

Detailed in Section 3.1 is a review on breathsound pathophysiology and its relevance in acoustics studies. Normal breathsounds are defined by the sound generated in healthy airways and lungs by unenforced breathing. These breathsounds can be tracheobronchial (or airway breathsounds) or vesicular (in the thorax) [1], and the deficiency of healthy breathsounds (or manifestation of adventitious breathsounds) can be a hallmark of pulmonary disease. It is therefore of interest to understand the acoustics of how these breathsounds are generated and how the acoustics change under pathological states relative to healthy models; the analysis of acoustical properties of these patient sets can provide invaluable information in the pathophysiology of the lungs and airways [2]. Of particular interest in this dissertation are crackles and wheezes.

Crackles. Crackles (or crepitations) are categorized with short, discontinuous, non-stationary sounds [1]. Crackles generate sound by the opening of closed airways; turbulent airflow effects caused by the re-equilibrium of pressure on a closed-off section of airways re-opening cause airway wall oscillatory motion, generating sound [2]. Although crackles generally happen in the inspiratory phase, they are known to occasionally occur during the expiratory phase [3]. Crackles are categorized into fine crackles, coarse crackles or a combination of the two (biphasic crackles). Crackles are associated with a variety of pathological lung and airway states, including (COPD), edema, bronchiectasis and fibrosis [1-4].

Wheezes. Wheezes are continuous and adventitious breathsounds heard between the end of the inspiratory phase and start of the expiratory phase. Compared to crackles, which generate sound via sharp re-openings causing airway radial motion, wheezes are caused by the gradual re-opening (inspiration) and closing (expiration). This gradual opening and closure of airways (including 100-250 ms duration) creates a harmonic which generates wall radial motion. Wheezes

can be heard from the mainstem bronchi (generation 2) down to 7 generations of airways [4]. The spectral content is wideband, from 100 Hz to 1 kHz, although some harmonics can go far beyond 1 kHz [6]. Theoretical models of wheezes incorporating flutter in flow-limited collapsible conduits show that the frequency of wheezing is affected by mechanical and geometrical properties including elasticity of the airways, thickness of the airway walls, and airway tension along (longitudinal) the airways [7].

A variety of lung injuries and pathologies result in breathsounds which alter sound propagation in the lung, with regional and spectral differences that, if properly quantified, can yield information about the lung pathology stage and progression. These breathsounds can be sharp or transient like crackles or more “musical” like ronchi, or have characteristics of both that make it difficult to differentiate between similar pathologies. Spectrally, breathsounds can be wideband or shortband, have a dominant frequency or be more disperse. Using acoustical techniques source localization can predict sound pathology location. This could be useful because while acoustically it may be difficult to differentiate between several lung pathologies, the generated sound origin may provide useful information that can eliminate possible pathologies, making diagnosis and treatment planning much easier and more targeted.

Advances in multi-sensor simultaneous auscultation methods have been made in mapping the acoustical profile of the thoracic cavity by several groups [7-11]. More recently, Kompis et al. [12] attempted to create a 3D acoustic image of predicted sound sources using multiple sensors and assuming a “ray acoustic” (incident field) model to predict sound propagation from these sources. They noted in their study that a useful imaging system for a lung should: 1) be robust with respect to acoustic properties, especially speed of sound which is highly variable and thus is not precisely known; 2) provide images and 3D data sets that are intuitively interpretable; and 3) be robust with respect to noisy data from individual sensors or missing sensors. His algorithmic approach included spherically symmetric sound radiation from a source, which propagated through the

thorax without reflections or standing waves. The only algorithm dependence was sound speed and length: attenuation was attributed per unit length via a damping factor. Sound localization was performed via signal triangulation with redundancy of the propagating sound. In five human studies, the algorithm indicated differences in predicted source location between inspiration and expiration. In one case, it predicted severe consolidation located in the lower left lung. However, parametric computer simulation studies showed that their algorithm lacked robustness, specifically with regards to acoustical properties. In an idealized phantom model, their algorithm demonstrated a 2 cm nominal resolution.

There are two main components to modeling sound transmission through the pulmonary system and chest region: 1) modeling sound transmission through the tracheobronchial tree, and 2) coupling the airway model to the biological tissue up to the thoracic surface, which includes lung parenchyma (and its varying composition of air, tissue, air and blood), bone (including the ribcage), surrounding muscle and soft outer tissues. Previous models of sound transmission included sound propagation studies including a full conducting airway model [13], along with other models of coupled organ structures.

In previous studies of sound transmission from biological tissue to the chest surface, robustness of the models used were limited in several aspects. In one study, the organs in the thoracic cavity assumed a simple geometry with homogenized material properties, such as its simulation as a 2D planar geometry [15]. In another study an axisymmetric layered model of the thorax with annular regions for the parenchyma, outer soft tissue, rib cage and skin was studied [16] and in a final study an axisymmetric cylindrical geometry with a uniform mass load of the chest on a lung parenchyma [17] was created.

In Ozer et al. [14], a boundary element (BE) model was created to model sound transmission through coupled biological tissue to the chest surface originating in a source located in a lung without an airway tree. The BE model was validated numerically, and compared vs experimental

studies on phantom lung models with no airway structure. Parametric studies were performed to quantify the effect of different model parameters on the acoustic field of the phantom models. In addition, the BE model was partnered with a source localization algorithm to predict the location of the acoustic source within the analytical and experimental models. The sound was localized experimentally using an array of sound measurements on the phantom surface. Experimental studies validated the BE source localization algorithm. Sound localization using incident field assumptions which neglect reflections and standing wave patters did not perform as well within the phantom. The BE model and sound localization procedure was then used on a lung geometry obtained via segmentation from the National Library of Medicine's Visible Human Project, which resulted in agreement with earlier findings that the BE model predicted the sound source well, whereas the incident field assumption proved to be a worse approach for localization.

4.2 THEORY

4.2.1 BE ELEMENT THEORY

In previous work [9, 14], a boundary element (BE) model was created to simulate fast compression wave sound propagation within the lung parenchyma. Sound propagation was calculated via the following:

$$\left(\boldsymbol{H}+\frac{1}{2}\boldsymbol{I}\right)\boldsymbol{\varphi}[\omega]=\boldsymbol{L}\boldsymbol{v}[\omega]+\boldsymbol{\varphi}^{\boldsymbol{inc}}[\omega]. \tag{4.1}$$

Here, $\boldsymbol{\varphi}$ and $\boldsymbol{v}$ are velocity potential and face centroid normal velocities vectors of length N, respectively, defined at the centroids of the N triangular discretized elements denote the lung surface. $\boldsymbol{I}$ is a square unit matrix of size N,. The acoustic pressure at the i^{th} boundary element is calculated via $p_i = j\omega\rho\varphi_i$, where ρ is the density of the bounded volume (in this case the lung parenchyma) and $j=\sqrt{-1}$. Derivations of $\boldsymbol{H}$ and $\boldsymbol{L}$ can be found in the references [9, 14, 18].

The incident field velocity potential $\boldsymbol{\varphi}^{\boldsymbol{inc}}$ listed above is meant to serve as a approximation for the acoustic input, and represents a finite number of monopoles. These monopoles represent the

conducting airway walls which, after air conduction, radiate transferred energy to the coupled lung parenchyma. In a "incident field" assumption, $\boldsymbol{\varphi}^{\boldsymbol{inc}}$ is assumed as the response, and this approach neglects any reflections or wave scattering and caused by the lung's parenchyma surface. In contrast, the BE model takes scattering and reflections into consideration.

For eq. (4.1) to be solved, the N boundary conditions relating $\boldsymbol{\varphi}$ and $\boldsymbol{v}$ need to be defined. Boundary conditions can be free $(\varphi_i = 0)$ or fixed $(v_i = 0)$ for all discretized boundary elements in a simpler implementation, or alternatively more complex using coupled linear algebraic equations relating $\boldsymbol{\varphi}$ and $\boldsymbol{v}$. These coupled boundary conditions can be calculated using numerical FE analysis, or through multiple implementations of BE simulation on volumes coupled to the BE volume of interest.

If using a complex boundary condition with FE formulation surrounding the BE volume, master degrees of freedom (DOFs) chosen must be consistent with BE DOFs. In other words, at the centroid of each boundary element where $\boldsymbol{\varphi}$ and $\boldsymbol{v}$ are defined and in a normal direction oriented away from the volume interior. This can be defined via application of Newton's law as:

$$-j\omega\rho\boldsymbol{A}\boldsymbol{\varphi} + \left(j\frac{\boldsymbol{K}}{\omega} + \boldsymbol{C} - j\omega\boldsymbol{M}\right)\boldsymbol{v} = \boldsymbol{F}. \tag{4.2}$$

Here, $\boldsymbol{K}$, $\boldsymbol{M}$, and $\boldsymbol{C}$ are structural stiffness, mass, and damping matrices, respectively, for the coupled organs surrounding the lung volume (chest wall, rib cage, scapula and sternum). The NxN matrix $\boldsymbol{A}$ is diagonal, with $[\boldsymbol{A}]_{ii}$ being the area of the i^{th} boundary element. The length N vector $\boldsymbol{F}$ represents external forces, for example sternal percussion from a mechanical shaker.

Generally, $\boldsymbol{K}$, $\boldsymbol{M}$, and $\boldsymbol{C}$ are non-diagonal matrices that couple the N DOFs to the BE model. These boundary conditions can also be decoupled to simplify the simulation. For example, considering only an inertial load on the elements, the stiffness and damping on the lung surface caused by the other organs in the thoracic cavity is neglected. Instead, the mass loading is considered independently. Suppose a volume of material of density ρ_{si} and thickness h_i resides

on the i^{th} element or a series of elements. Then, $\boldsymbol{M}$ is diagonal with $[M]_{ii} = [A]_{ii} h_i \rho_{si}$ and $\boldsymbol{K}$ and $\boldsymbol{C}$ are neglected. If $\boldsymbol{F} = 0$, eq. (2) reduces to decoupled scalar equations:

$$-\rho\varphi_i - h_i \rho_{si} v_i = 0 \quad i = 1, \dots, N \tag{4.3}$$

$$\boldsymbol{v}[\omega] = -\left(\boldsymbol{H} + \frac{1}{2}\boldsymbol{I}\right)^{-1} \boldsymbol{\varphi^{inc}}[\omega], \tag{4.4}$$

Neglecting mass loading and inertial loading on the surface of the model yields a free field model, where only attenuation per unit distance, wave reflections and standing waves are considered by dropping $\boldsymbol{K}$, $\boldsymbol{M}$, and $\boldsymbol{C}$. By rearranging eqn. (4.1), this can be simplified to:

$$0 = \boldsymbol{L}\boldsymbol{v}[\omega] + \boldsymbol{\varphi^{inc}}[\omega]. \tag{4.5}$$

$$\boldsymbol{v}[\omega] = -L^{-1}\boldsymbol{\varphi^{inc}}[\omega]. \tag{4.6}$$

Simplifying the BE model to a free field model has some advantages in computation speed, and provide a basis for comparison versus existing mass loaded models presented in this dissertation. In the mass loaded BE model, damping and elasticity of the thoracic cavity organs and chest surface were neglected. However, the density of material ρ_{si} and thickness h_i residing on the i^{th} boundary element were used to construct a mass matrix that was correlated with the mass load, with the density of the chest wall density of 1,000 kg/m^3, bone with a density of 1,800 kg/m^3 and the lung with a density of 240 kg/m^3.

4.2.2 MONOPOLE SOURCE EVALUATION

The acoustic monopole strength, Q_s in $meter^3/second$ for a particular airway segment calculated via the modified 1D waveguide in section 2 or 3 for breathsounds can be calculated given the segment length L and radius r, and the complex amplitude of its acoustic radial velocity U_S via [13]:

$$Q_s = 2\pi r L U_S. \tag{4.7}$$

If we define a spherical finite monopole located at the centroid of a cylindrical airway segment to have the same acoustic strength and radius r, there needs to be a conversion from cylindrical strength per segment, thus the spherical strength Q_m is:

$$Q_m = 4\pi r^2 U_m, \tag{4.8}$$

$$U_m = \frac{1}{2} * \frac{L}{r} * U_S, \tag{4.9}$$

where U_m is the monopole radial velocity amplitude. To solve for U_m, the midpoint of the cylindrical segments in the conducting tree model are approximated as monopole sources.

Additionally, Green's function can be solved via the following equations [14]:

$$G[p,q] = \frac{1}{4\pi R} e^{jK_p R}, \tag{4.10}$$

$$R = |p - q|, \tag{4.11}$$

where p and q are the BE centroid and monopole location, respectively, and K_p is the lung compression wave complex wavenumber. The incident field created via a single monopole source within the lung volume is found by multiplying its strength $Q_s = Q_m$ by the Green's function. Thus, the incident field φ_i^{inc} at the on the surface of the i^{th} boundary element's centroid is created by taking the summing the number of segment monopoles S via:

$$\varphi_i^{inc} = \sum_{s=1}^{S} Q_s G[p_i, q_s]. \tag{4.12}$$

The value of U_S for each airway segment is calculated via the modified 1D waveguide and per equations (4.8,9), and is unique per simulation model excitation mode and pathological state [14].

So, for the incident fields at the i^{th} centroid we have:

$$\varphi_i^{inc} = \sum_{s=1}^{S} Q_s \frac{1}{4\pi R_s} e^{jK_p R_s}, \tag{4.13}$$

$$v_i^{inc} = \nabla\varphi_i^{inc} = \sum_{s=1}^{S} cos[\gamma_s] \left(\frac{jK_p R_s - 1}{R_s}\right) Q_s \frac{1}{4\pi R_s} e^{jK_p R_s}, \tag{4.14}$$

where γ_s is the angle between the line $(p_i - q_s)$ and the normal to the i[th] BE.

The complex valued wavenumber K_p was calculated based on the fast compression wave speed and attenuation via application of Biot theory [19-20] as described in Dai et al. [21]. The wavenumber was calculated for 200, 400 and 800 Hz. Then, a final set of three wavenumbers were calculated for a fibrotic subject by increasing the shear viscoelasticity of the parenchyma by a factor of 5. Below in Table 4.1 is a table of k_p values.

Frequency (Hz)	Healthy	Fibrotic
200	24.4+ 8.94j	24.8 + 8.14j
400	28.0 + 29.0j	28.0 + 27.5j
800	37.6 + 67.6j	37.6 + 67.6j

Table 4.1. k_p values used in BE and incident field model simulations

4.2.3 SOURCE LOCALIZATION

The beamformer equation for the Bartlett processor is [14]:

$$B(\theta) = \frac{|\boldsymbol{a}^H[\omega,\theta]\boldsymbol{y}[\omega]|^2}{\boldsymbol{a}^H[\omega,\theta]\boldsymbol{a}[\omega,\theta]}. \quad (4.15)$$

Here, $\boldsymbol{a}[\omega,\theta]$ is a vector of length N_R of the predicted responses at N_R sensor locations due to a monopole source located at θ of frequency ω; **y** is a vector of the measured responses at those N_R sensor locations. In the context of this dissertation, θ refers to a set of x,y,z Cartesian coordinates. Superscript H denotes the Hermitian of the vector. First, a grid is created within the volume where the source will be searched. This grid was created by overlapping the BE volume with a regular grid, with a defined spacing. The grid is then checked relative to the BE volume and

points inside are kept and put into a BE hypothetical monopole source grid of size N_θ, while the points outside are discarded. The Bartlett processor is then evaluated via eqn. (4.15).

Implementing the source localization algorithm via application with Bartlett processors requires use of the BE solution as the experimental measurement at the N_R sensor locations. In other words: $\boldsymbol{y}[\omega] = \boldsymbol{v}[\omega]$, where $\boldsymbol{v}[\omega]$ is obtained by solving eqs. (4.4,6) with modifications for the incident field for non-BE simulation.

If the simulation type uses BE then the Bartlett processor vector $\boldsymbol{a}[\omega, \theta]$ is obtained also using eqs. (4.4,6) just like $\boldsymbol{y}[\omega]$, but $\boldsymbol{\varphi^{inc}}[\omega]$ is calculated iteratively per hypothetical monopole source at a time at location θ.

If we are using the incident field assumption then $\boldsymbol{a}[\omega, \theta] = \boldsymbol{v^{inc}}[\omega, \theta]$ via eqn. (4.12), except that only a single iterative hypothetical monopole at location θ of strength Q_θ is assumed in the final calculation. In other words:

$$v_r^{inc} = cos[\gamma_\theta]\left(\frac{jK_pR_\theta - 1}{R_\theta}\right)Q_\theta \frac{1}{4\pi R_\theta} e^{jK_pR_\theta}, \tag{4.16}$$

where R_θ is the distance between the rth sensor location and hypothetical monopole location θ.

Once all Bartlett processors are calculated, they are then subdivided based on the magnitude of their results into bins of (typically) 10 or 20. In either set the highest bin would denote the Bartlett processors predicting the most likely source location.

4.3 BE AND INCIDENT FIELD MODEL SETUP AND SIMULATION

For all studies conducted in this dissertation for BE, incident field and source localization, the conducting tree model and lung geometry subdivided into lobes was obtained from Miyakawi et al. [22], which were developed according to a hybrid segmentation approach involving image

segmentation to develop an anatomically relevant airway skeleton model along with algorithmic generation of airway segments to fill in the conducting tree. Section 2.2.1 has a full outline of this process. The full conducting tree model consisted of about 60,000 cylindrical segments.

In this dissertation, the left lung was used individually for BE/incident field analysis and source localization. Moreover, the left lung was meshed without lobe differentiation to simplify the surface volume in terms of discretized surface elements. Because of the nature of image segmentation, when the left lung was meshed with differentiation based on lobe geometry the lung mesh along the fissures was complex, leading to more surface elements being needed to mesh accurately. As a result, the left lung was meshed without lobe differentiation to bring node count down. The final lung volume consisted of 6,188 surface elements.

4.3.1 SIMULATION OVERVIEW

The mass loading BE, free field and incident field simulation were all performed on the left lung discretized into 6,188 surface elements. All analytical modeling and analysis were done in MATLAB 2016a [23]. To determine the source monopoles for BE analysis, the full conducting tree model was subdivided into two parts: segments with midpoints within the left lung, and those without. Only the segments with midpoints in the left lung were considered as monopoles in the left lung and the rest discarded. There were about 30,000 monopoles in the left lung used in the BE analysis. Shown in Figure 4.1 is the geometry used in all BE, free field and incident field simulations, with red dots signifying monopole locations and blue arrow signifying surface element normals.

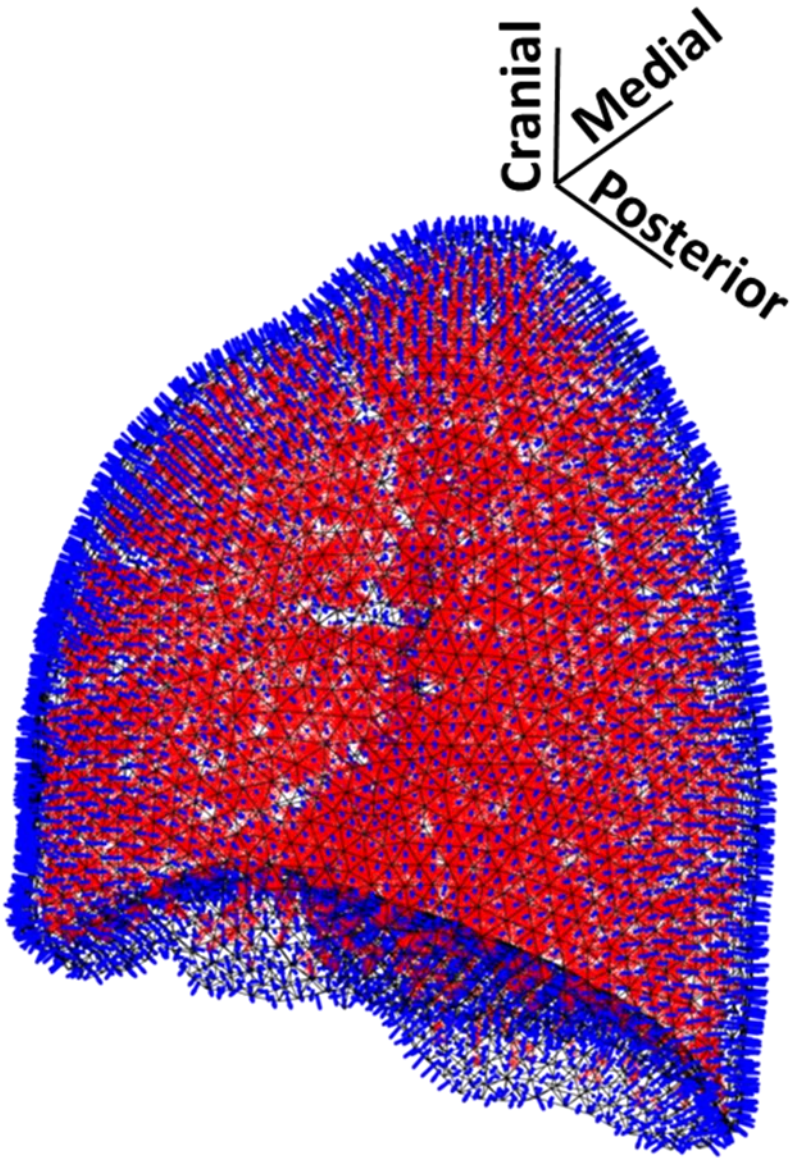

Figure 4.1. Left lung depicted as a wireframe mesh in a coronal orientation. Red dots inside the left lung depict the monopole locations from the conducting tree geometry. Blue arrows depict the surface centroid norms.

For the mass loading BE simulation, the boundary conditions and mass-load setup was performed via Section 4.2.1. Monopole strength was calculated via Section 4.2.2 for all segments in the left lobe. Average monopole strength across each Horsfield order can be seen in Figure

4.2 for the three models used in this study: healthy and fibrotic insonification along with bronchoconstriction wheeze BS cases.

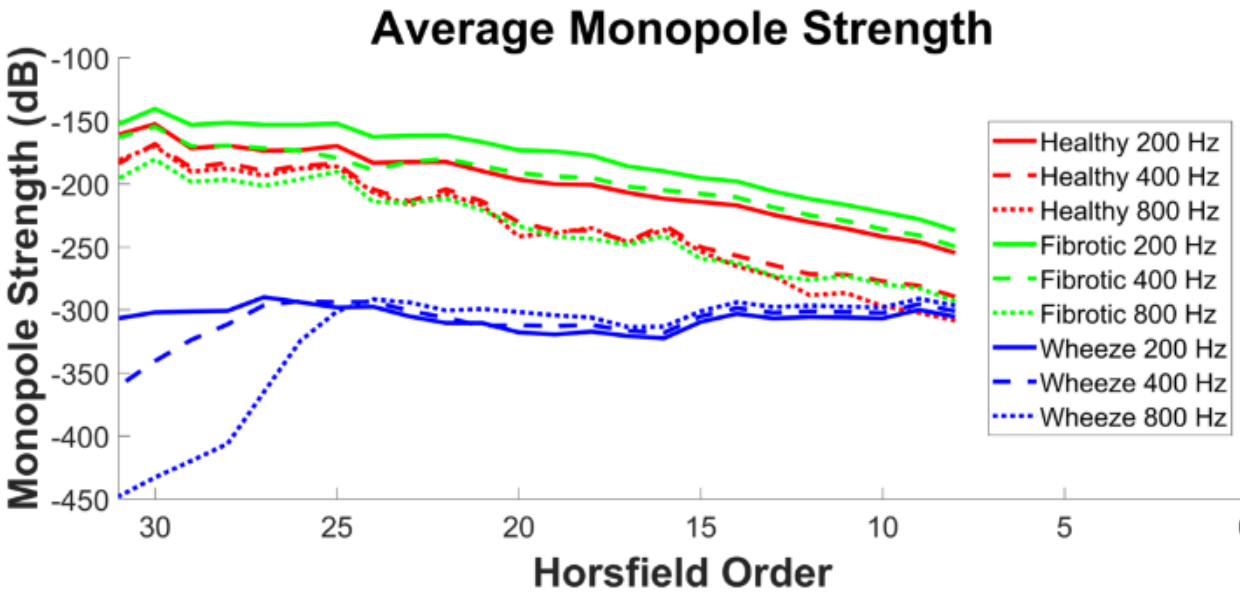

Figure 4.2. Average monopole strength in dB (ref. 1 m/s) for healthy (red) and fibrotic (green) insonification models and wheeze BS (blue) case at 200 (solid line), 400 (dashed line) and 800 (dotted line) Hz.

Magnitudes of acoustic normal velocities for the segments in the conducting tree were calculated via the modified 1D waveguide in Section 2.2.3. The mass load on the left lung was done by calculating from each lung centroid normal the distance from the centroid to the edge of the torso surface, taking into consideration all intersections into the bone structures (ribcage, sternum), and the right lung. For each intersection into the bone or right lung (if applicable), the intersection ingress and egress distance was recorded. These distances were translated into the "thicknesses" from the centroid out to the torso surface, and the mass load per centroid was calculated with the unique path through the thoracic cavity, other organ intersections included. This process can is illustrated in Figure 4.3.

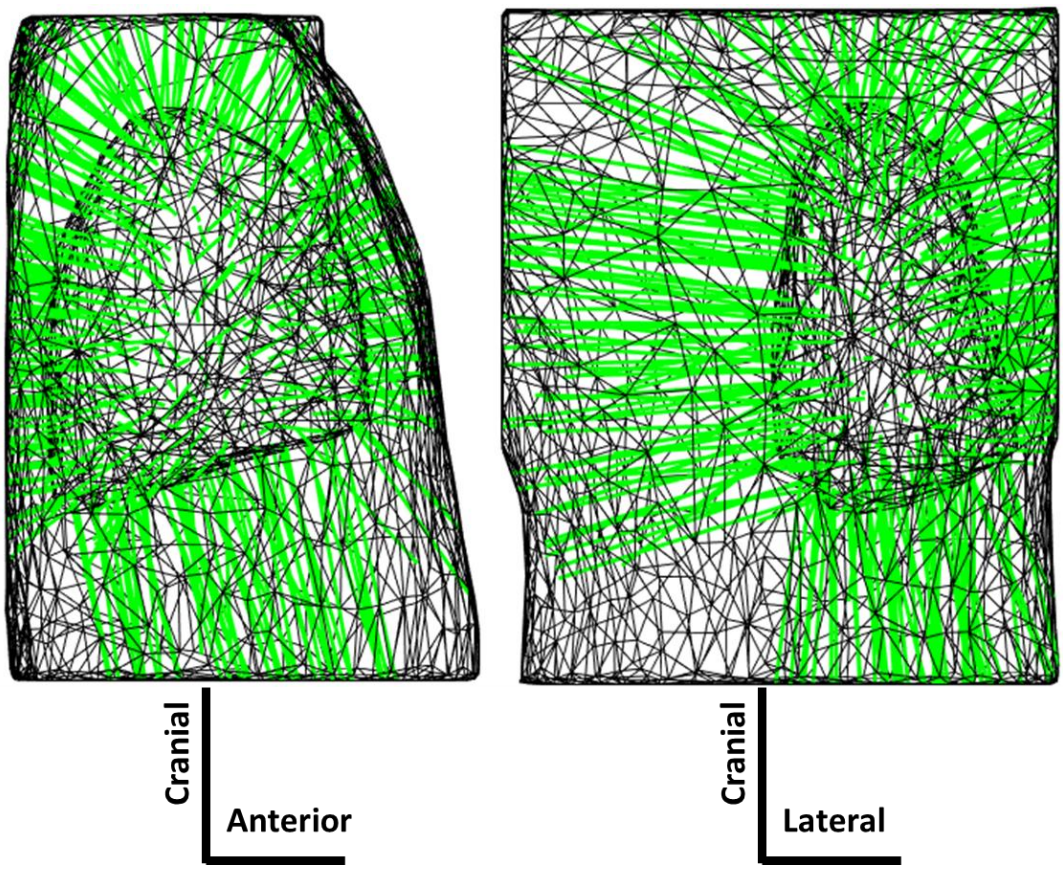

Figure 4.3. Chest surface with example left lung. The extended green lines from the lung to the surface of the torso depict the line of sight from the centroid norms of the lung surface to the torso.

Additionally, a model of the thoracic cavity used with some modification can be seen in Figure 4.4. The scapula were discarded from analysis due to difficulty in determining the thickness of the segments; a small part of the scapula intersected the torso surface and caused improper line of sight issues when calculating the thickness.

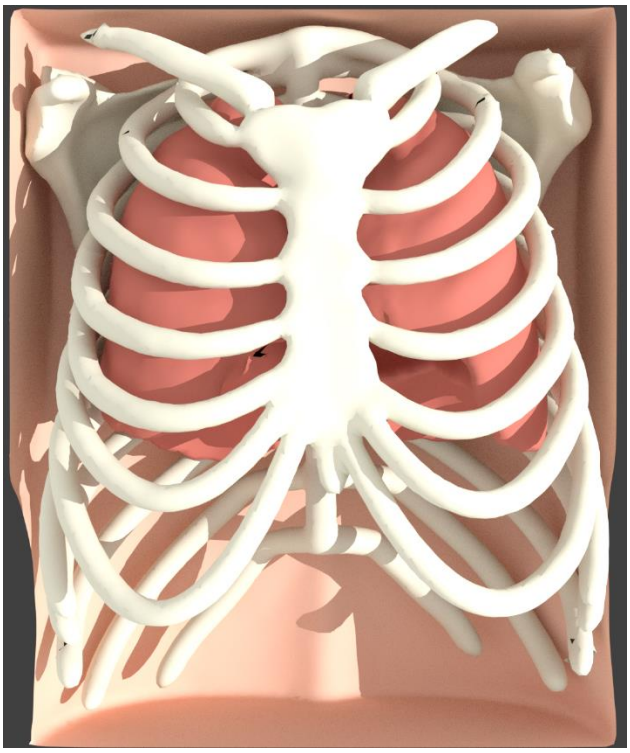

Figure 4.4. Depiction of the thoracic cavity with the anterior end open to depict internal geometry. Included in the thoracic cavity model is the ribcage, lungs scapula and torso surface. The scapula were not used in mass loading calculations.

Mass loading simulations included insonification models (healthy and fibrosis) as well as three BS model types (healthy, PI and bronchoconstriction) at 200, 400 and 800 Hz. Healthy and PI wheeze models were used for comparison, for simplicity bronchoconstriction wheeze BS models are referred to as wheeze BS models. Free field and incident field simulation only include wheeze BS models at 200, 400 and 800 Hz. Per simulation type calculation of the Green function via eqn. (4.12) was frequency dependent and used k_p values per Table 4.1.

4.3.2 ALGORITHM ADAPTATION AND IMPROVEMENTS

In Ozer et al. [14], the BE and localization algorithm was hardcoded to fit the phantom geometry. Present use of the algorithm calculates all acoustic parameters dynamically based on file input. The BE algorithm in this dissertation requires two inputs: a stereolithography (STL) file noting the

lung volume as a series of discretized triangular surface elements, and a 1D modified waveguide or 1D BS waveguide acoustic map of the conducting tree for the accompanying STL volume.

In BE, to solve the above set of 2N non-coupled equations (4.4,6) to calculate the lung surface normal acoustic velocity requires inverse matrix operations in MATLAB. Even using the backslash operator, this complex non-sparse calculation depending on the number of discretized surface elements N can make this step computationally expensive. To reduce computation time and memory usage c++ MEX files were compiled and wrapped into the MATLAB application as an alternative to the backslash operator. In doing so, the complex matrix division compute time was reduced from ~10 to ~3 seconds per iteration. For a STL volume with 6,188 discretized elements with the improvements above, calculation of the discretized lung centroid normal velocity takes 42 seconds.

As a final improvement, the code was adapted to run as a batch process. The user can specify a folder with the given lung geometry and monopole strengths. Per filename of the monopole strengths the algorithm would set proper material properties (wavenumber) based on a specific parsed filename including frequency, run the BE or incident field code and output the lung surface velocity vector to a specified folder.

4.3.3 ACOUSTIC PROFILES AND RESULTS

The centroid normal acoustic velocity map for healthy and fibrotic insonification cases at 200, 400 and 800 Hz can be seen in Figure 4.5 for mass loaded BE. The centroid normal acoustic velocity map for “healthy” BS, PI BS and bronchoconstriction BS models at 200, 400 and 800 Hz can be seen in Figure 4.6 for mass loaded BE. For figure orientation, anterior direction to the left, lateral coming out of the page, and cranial at the top of the figure.

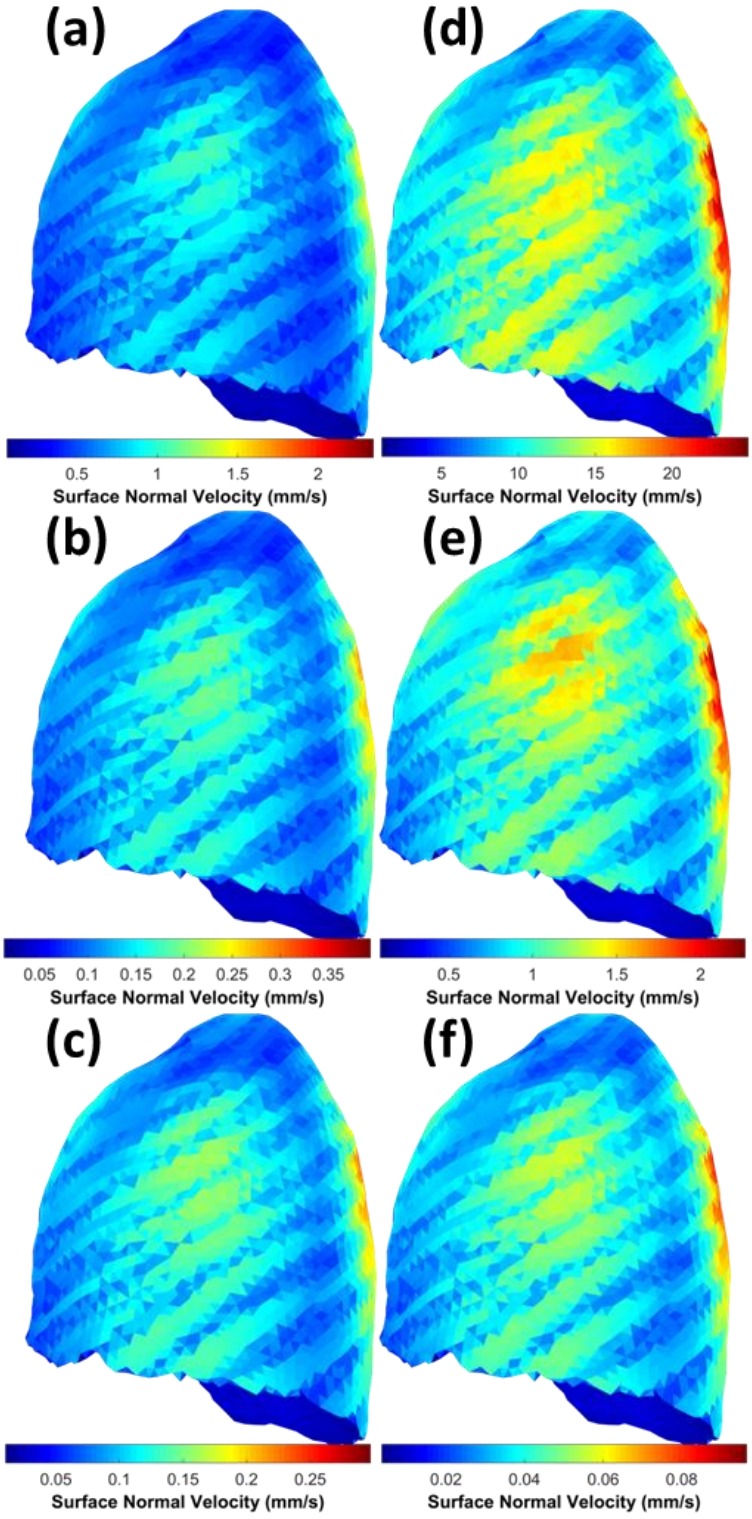

Figure 4.5. Lung centroid normal acoustic velocity amplitude with healthy and fibrotic insonification models at 200, 400 and 800 Hz for (a-c) healthy and (d-f) fibrotic lung cases. Anterior direction to the left, lateral coming out of the page, and cranial at the top of the figure.

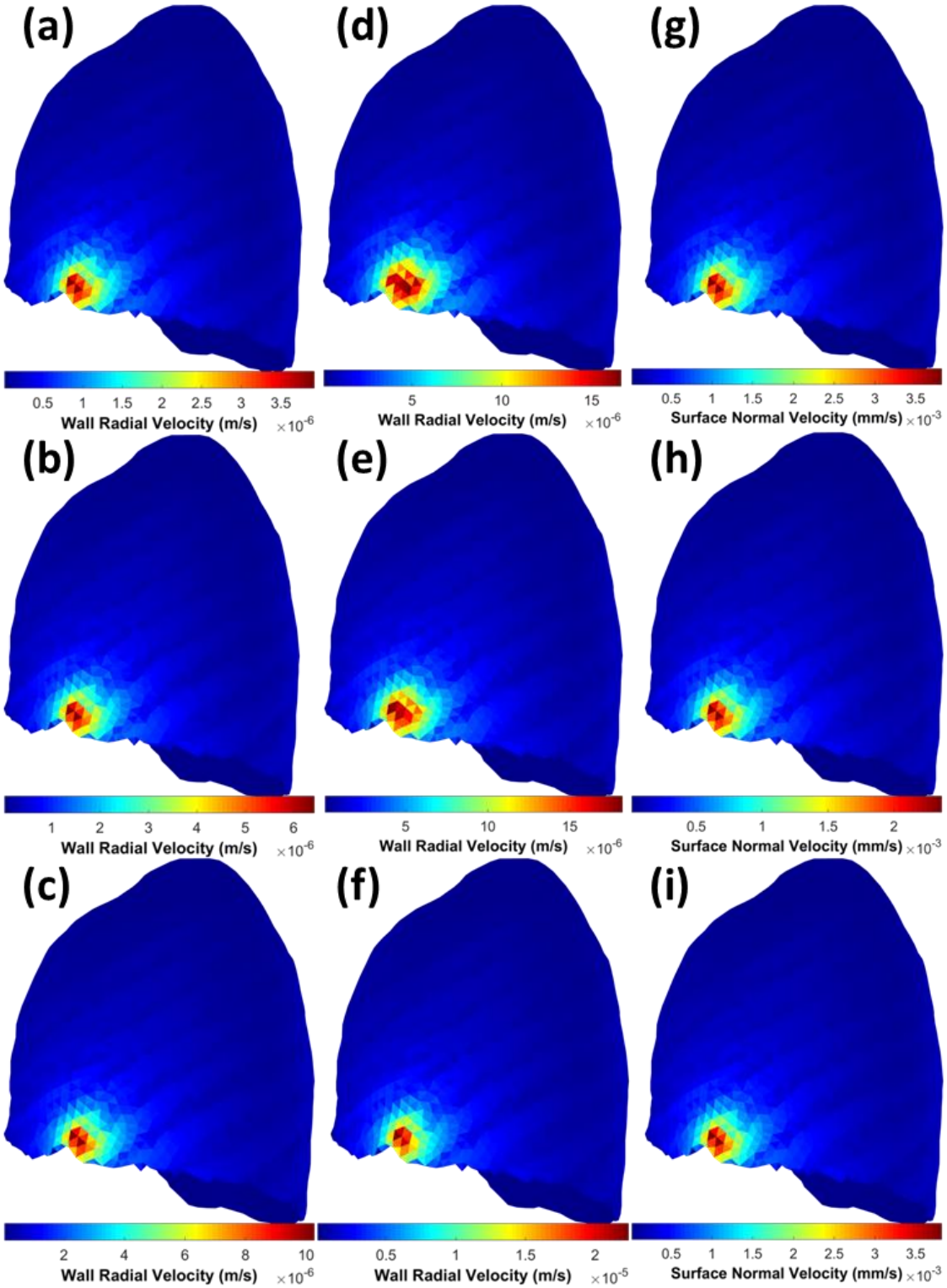

Figure 4.6. Lung centroid normal acoustic velocity amplitude with BS models at 200, 400 and 800 Hz for (a-c) healthy, (d-f) PI and (g-i) bronchoconstriction cases. Anterior direction to the left, lateral coming out of the page, and cranial at the top of the figure.

Maximum centroid velocity amplitude for normal and fibrotic insonification models along with the wheeze BS model can be seen in Table 4.2.

Frequency (Hz)	Normal	Fibrosis	Wheeze
200	2.30	2.50	1.43×10^{-3}
400	0.394	2.30	2.36×10^{-3}
800	0.297	0.0965	3.82×10^{-3}

Table 4.2. Maximum centroid amplitude for normal, fibrotic insonification models and wheeze BS model for 200, 400 and 800 Hz.

The centroid normal acoustic velocity map for wheeze BS models at 200, 400 and 800 Hz can be seen in Figure 4.7 for free field BE. For figure orientation, anterior direction to the left, lateral coming out of the page, and cranial at the top of the figure.

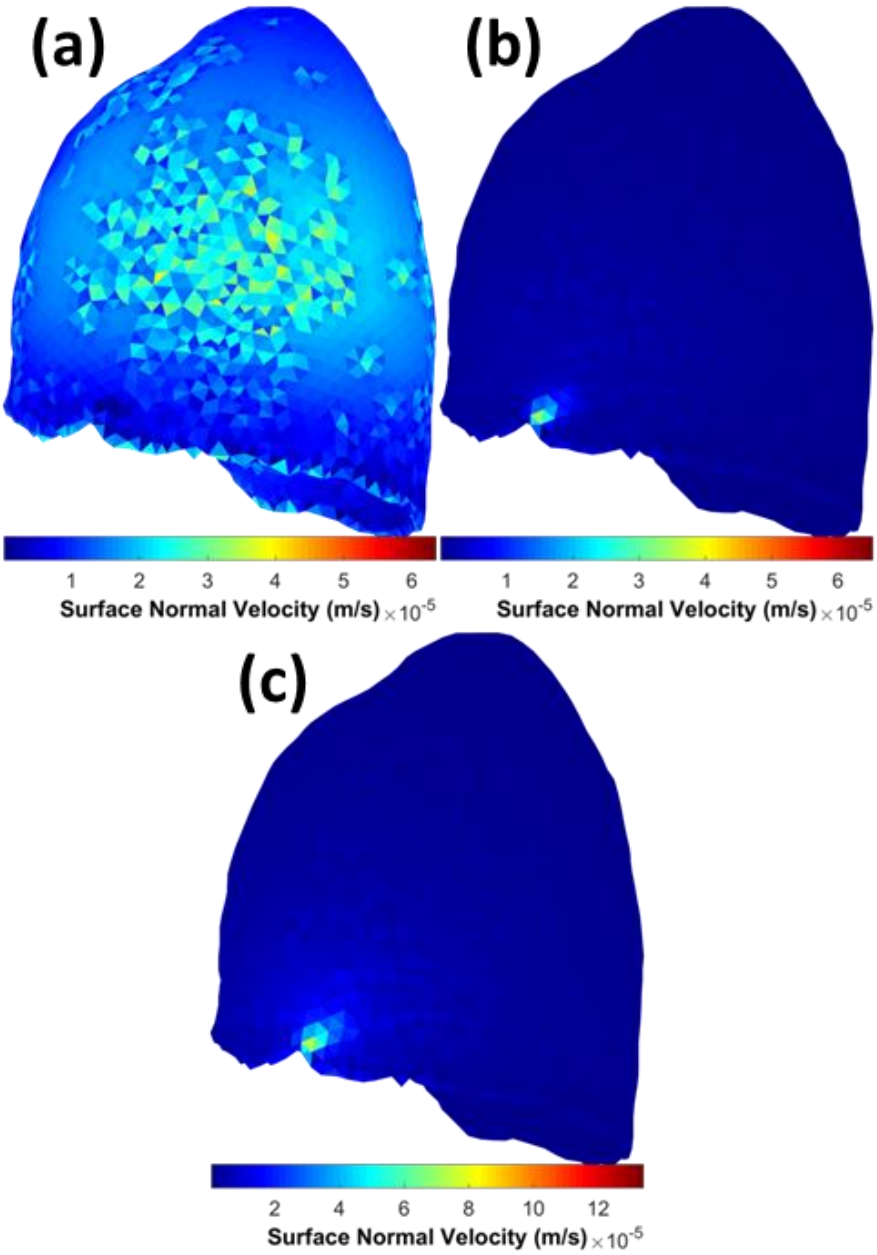

Figure 4.7. Lung centroid normal acoustic velocity amplitude with BS models at 200, 400 and 800 Hz for (a-c) wheeze BS cases for free field BE. Anterior direction to the left, lateral coming out of the page, and cranial at the top of the figure.

The centroid normal acoustic velocity map for wheeze BS cases at 200, 400 and 800 Hz can be seen in Figure 4.8 for incident field. For figure orientation, anterior direction to the left, lateral coming out of the page, and cranial at the top of the figure.

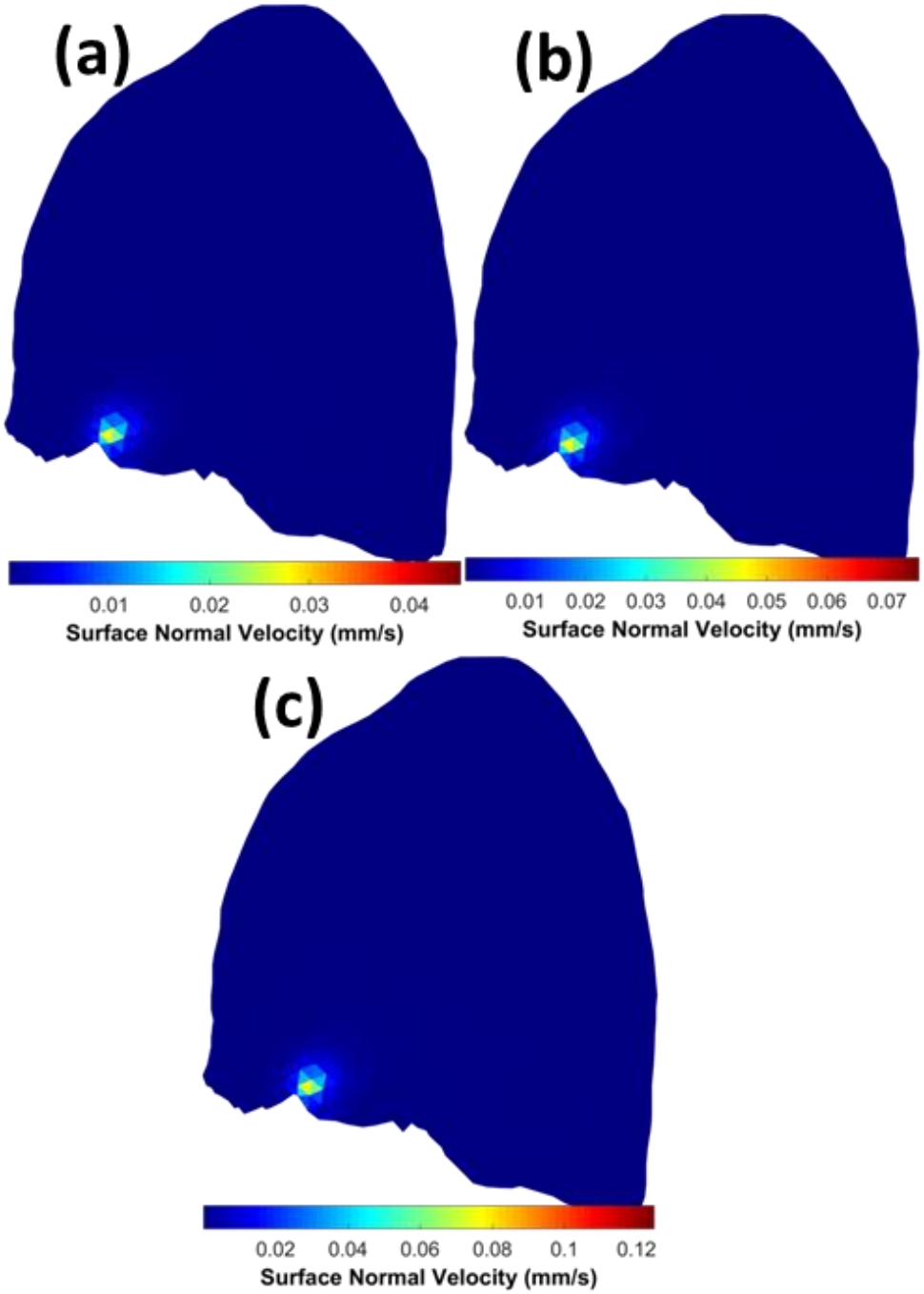

Figure 4.8. Lung centroid normal acoustic velocity amplitude with BS models at 200, 400 and 800 Hz for (a-c) wheeze BS cases with incident field. Anterior direction to the left, lateral coming out of the page, and cranial at the top of the figure.

4.4 SOURCE LOCALIZATION IN A HUMAN LEFT LUNG

For mass loaded BE and incident field simulations in Section 4.3, a source localization algorithm presented in Section 4.2.3 was applied to determine the hypothetical location of the acoustic source based on the simulations and results presented in Section 4.3.3.

The hypothetical monopole source grid outlined in Section 4.2.3 was created by creating a uniform grid of points spaced 1 cm apart using the left lung coordinate bounds to create a box. The grid was then subdivided in a similar fashion to the monopole sources in the left lung via Section 4.3.1 by dividing the points based on their inclusion in the left lung. Points in the left lung became the hypothetical monopole source locations. After subdivision, there were 2,370 hypothetical monopole sources in the grid in the left lung spaced 1 cm apart. Figure 4.9 shows the left lung and hypothetical source grid.

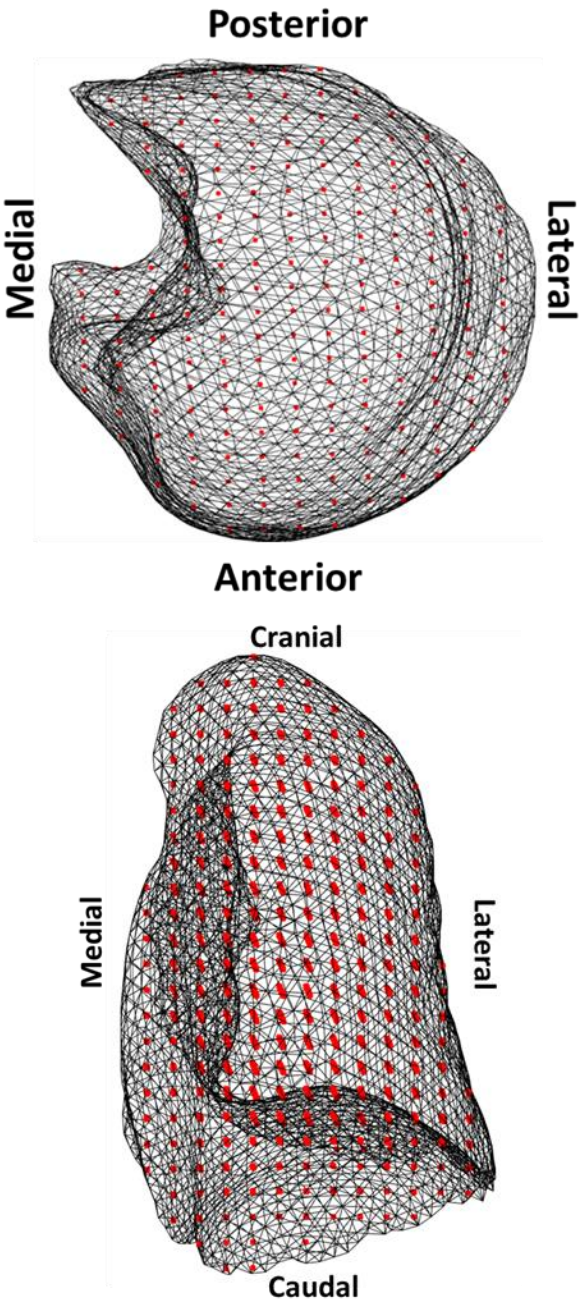

Figure 4.9. The left lung discretized surface depicted as a wireframe mesh, with red dots inside depicting the $N_\theta = 2{,}370$ hypothetical monopole source locations. Shown on top is an axial plane with a sagittal plane underneath.

4.4.1 LOCALIZATION OVERVIEW

Per 4.2.3, the theory of the source localization algorithm is described. The hypothetical source grid used for all studies included 2,370 points spaced 1 cm apart. As such, 2,370 iterations of complex division were required to predict the sound source.

Three sets of studies were performed for mass loading: one including all N lung surface elements, a second with one in every 10 lung surface elements chosen from face centroid index 1 to N in an increment of 9 indices, and then a series of 3x3 grids on the lung surface to simulate a 3x3 sensor, at 200, 400 and 800 Hz. For the healthy and fibrotic insonification models, only the full model was tested. For the wheeze BS model, four 3x3 grid locations were placed per Figure 4.10. One set of two 3x3 grids were spaced about 10 mm apart, with the larger grid spaced ~42.5 mm apart. In addition, one set of two 3x3 grids were placed over the BS source location with the other two placed 13 cm cranial to the source location. Sound localization was not performed on free field models.

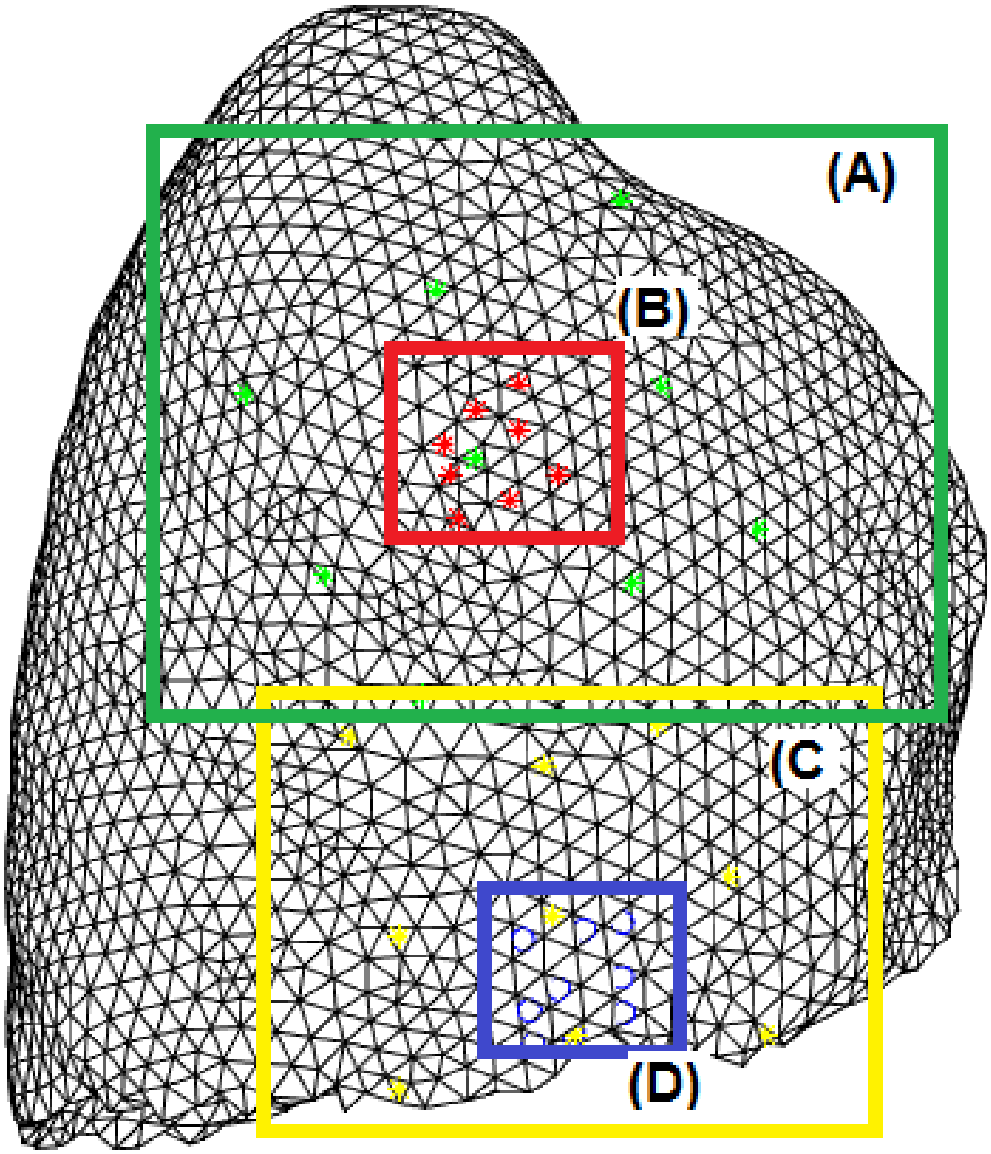

Figure 4.10. 3x3 grid locations for bronchoconstriction BS model cases. (a,c) show large spaced grids in red and yellow respectively with average 42.5 mm spacing, (b,d) show large spaced grids in green and blue respectively with 10 mm spacing. (a,b) are placed 13 cm cranial to the source location, (c,d) are centered around the source location.

Insonification modes utilized 10 bins in categorizing the Bartlett processors. The top 10% were used to predict the source location. BS models utilized 20 Bartlett processors, with the top 5% used to predict the source location.

4.4.2 ALGORITHM ADAPTATION AND IMPROVEMENTS

The lung centroid normal velocity field was calculated with the algorithm improvements via section 4.3.2. As noted earlier, source localization is an iterative operation per hypothetical monopole source location; normally per 2,370 hypothetical monopole points the iterative calculation would take ~2 hours with 3 seconds per iteration.

In MATLAB, the actual runtime for insonification and wheeze BS models were (on average) 1 hour 30 min. However, because these iterative calculations are independent of each other, they can be done in parallel. Running a parallel grid on a 64-bit Windows computer with two 4-core processors at 2.7 GHz and 16 GB RAM with 8 parallel tasks, reduced the 1 hour 30 min localization runtime to around 45 min.

Also per Section 4.3.2, as a final improvement the code was adapted to run as a batch process. The user can specify a folder with the hypothetical monopole grid and lung centroid normal acoustic velocities and per filename associate material properties (wavenumber) accordingly. The localization algorithm would run and output the Bartlett processors to file to a folder specified.

4.4.3 SOURCE LOCALIZATION RESULTS

Source localization for healthy and fibrotic insonification models with the top Bartlett processor (top 5%) shown in green, the second (top 15-5%) shown in yellow and third (top 25-15%) shown in red in Figure 4.11 on a pale blue transparent lung isosurface. Source localization for healthy BS, PI BS and bronchoconstriction BS mass loaded BE models with the top Bartlett processor (top 10%) shown in green, the second (top 20-10%) shown in yellow and third (top 30-20%) shown in red in Figure 4.12 on a pale blue transparent lung subsurface. Source localizations shown from the thorax front, side, and isometric viewpoints.

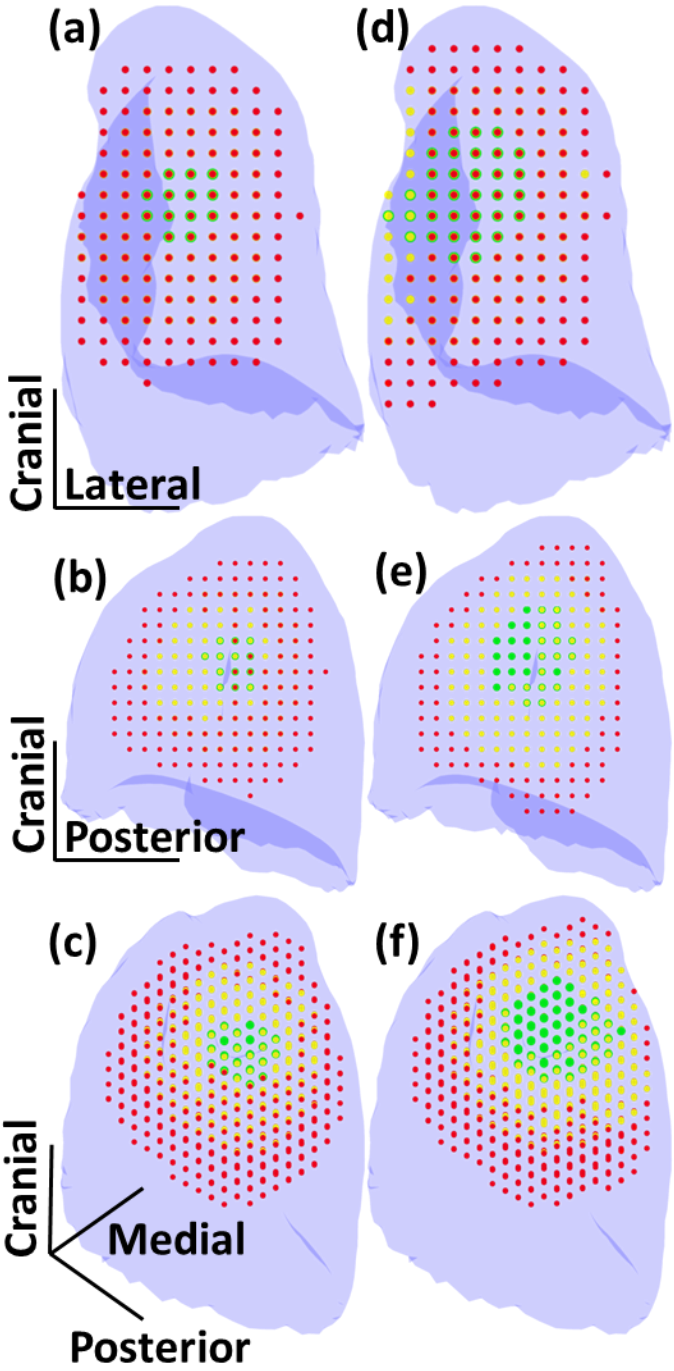

Figure 4.11. Source localization for insonified healthy (a-c) and fibrotic (d-f) lung at 400 Hz. Left lung shown as a light blue transparent isosurface, with source localizations shown from the thorax front, side, and isometrically. Green, yellow and red dots represent Bartlett confidence regions in the top 5% (>95%), 85-95%, and 75-85%, respectively.

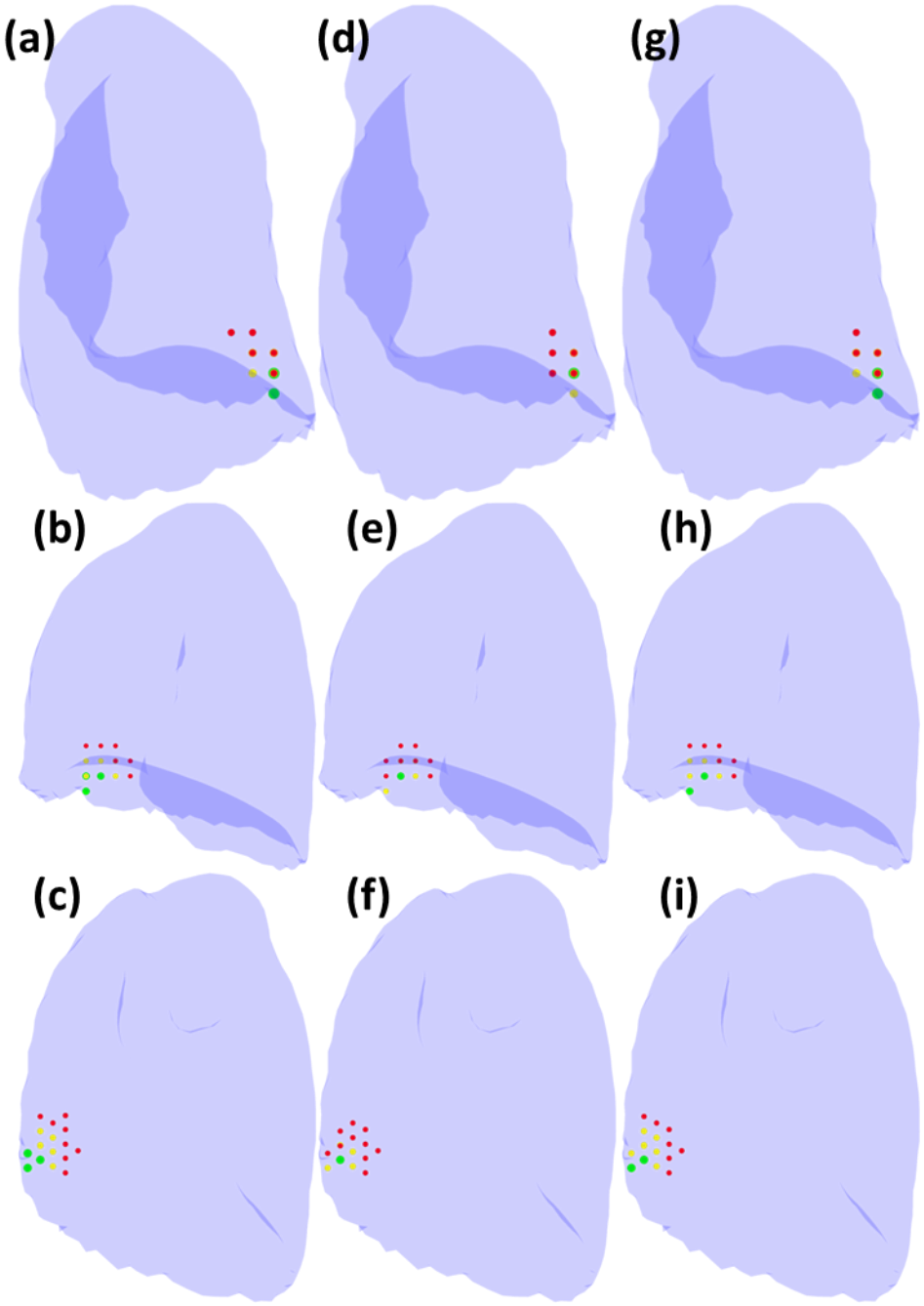

Figure 4.12. Source localization for healthy BS (a-c), PI BS (d-f) and bronchoconstriction BS (g-i) lung at 400 Hz. Left lung shown as a light blue transparent isosurface, with source localizations shown from the thorax front, side, and isometrically. Green, yellow and red dots represent Bartlett confidence regions in the top 10% (>90%), 80-90%, and 70-80%, respectively.

Bartlett processors for healthy and fibrotic insonification models at 400 Hz noted in terms of the volume of the confidence regions for >95%, 85-95% and 75-85% can be seen in Table 4.3. The volume of the Bartlett confidence region was calculated by measuring the volume created by the 1 cm spaced Bartlett processors in the associated confidence regions.

Bartlett confidence regions	Healthy Lung	Fibrotic Lung	Percent Increase
>95%	1.22%	3.67%	301%
>85%	21.7%	30.1%	39.0%
>75%	48.1%	56.5%	17.5%

Table 4.3. Bartlett confidence regions specified by volume for healthy and fibrotic insonification models at 400 Hz for >95%, 85-95% and 75-85% confidence regions

Bartlett processor results from healthy and fibrotic insonification models with the conducting airways with the top 30% magnitude of wall radial velocity (ref. 1 m/s) colored by wall radial velocity magnitude can be seen in Figure 4.13. Bartlett processor results from wheeze BS model with overlayed conducting airways colored by wall radial velocity magnitude can be seen in Figure 4.14.

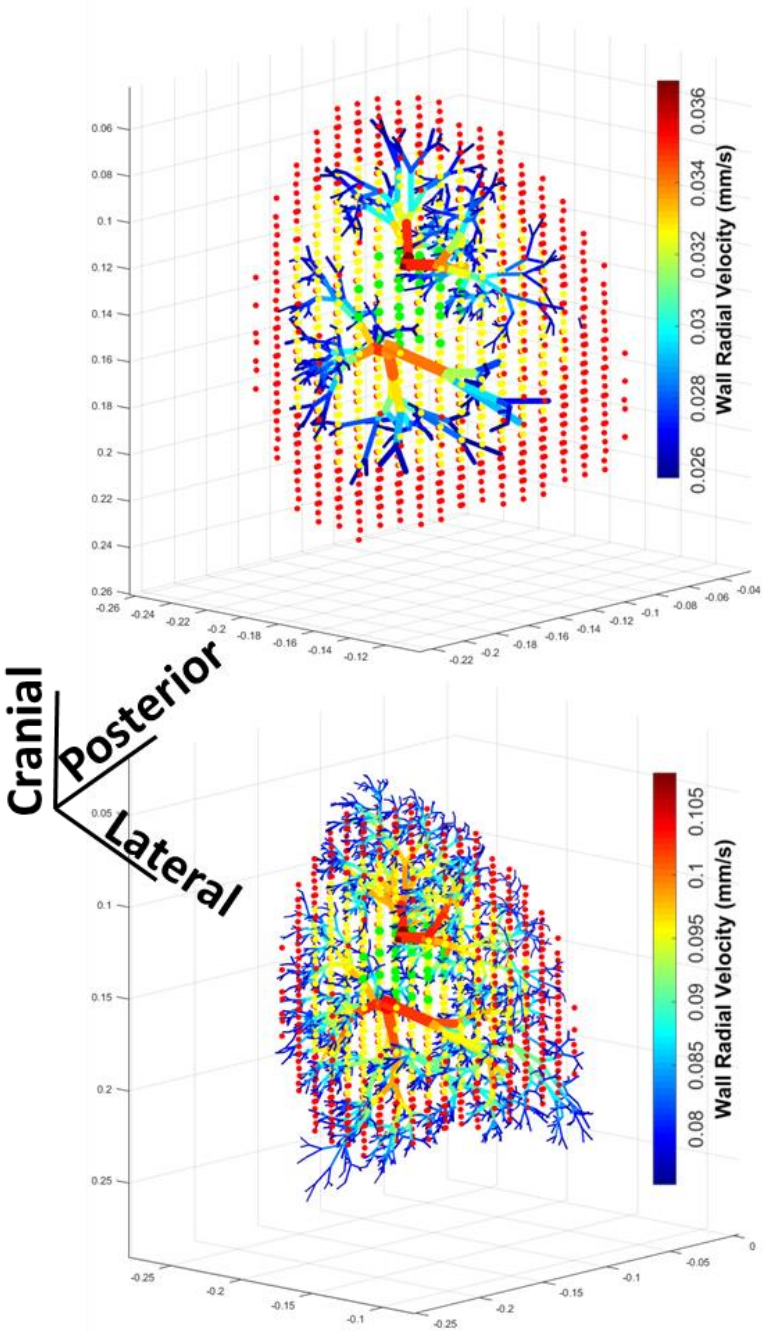

Figure 4.13. Top Bartlett processors of healthy and fibrotic insonification models with major airway branches with the top 30% magnitude of airway wall radial velocity (ref. 1 dB) colored by magnitude. Insonified (a) healthy and (b) fibrotic lung.

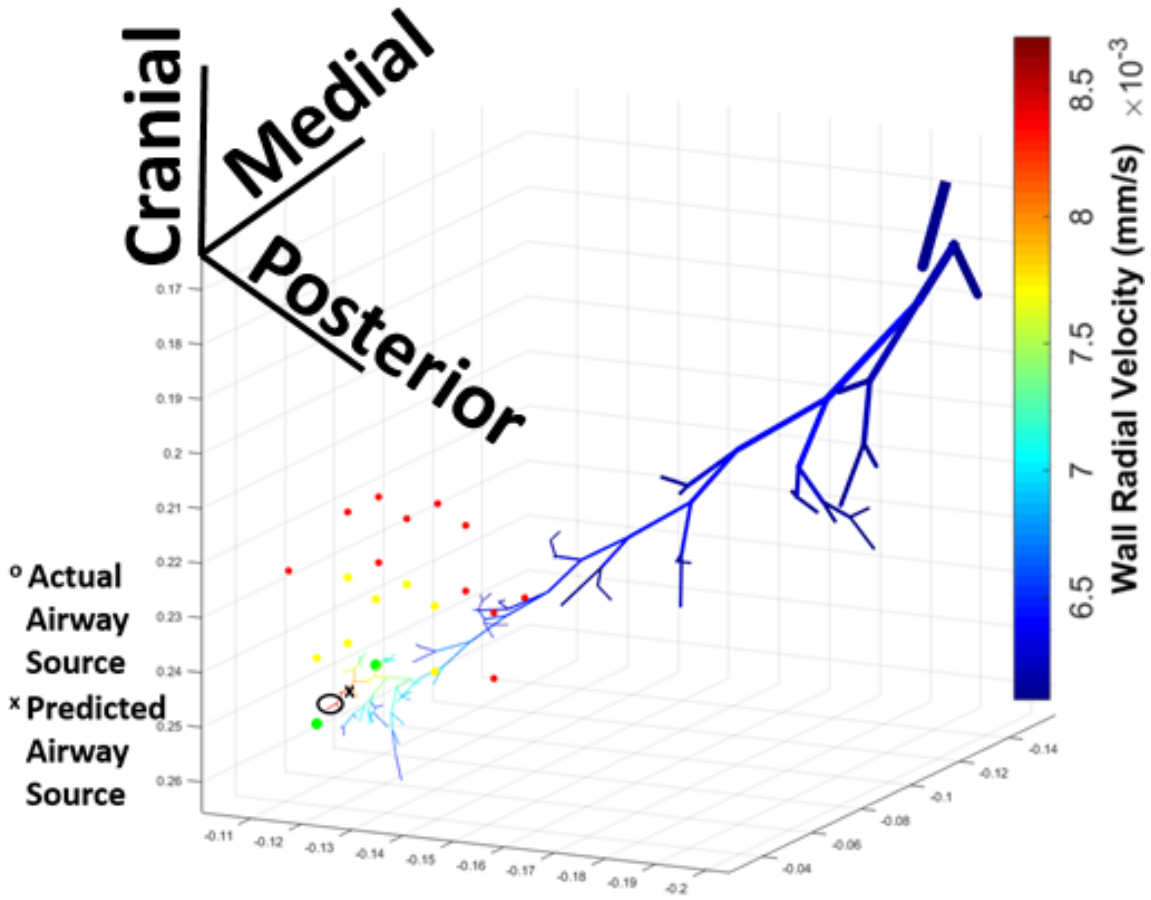

Figure 4.14. Top Bartlett processors of wheeze BS model with major airway branches with the top 30% magnitude of airway wall radial velocity (ref. 1 dB) colored by magnitude for bronchoconstriction BS model.

Source localization for wheeze BS mass loaded BE and incident field models with the top Bartlett processor (top 10%) shown in green, the second (top 20-10%) shown in yellow and third (top 30-20%) shown in red in Figure 4.15 on a pale blue transparent lung subsurface. Location of top Bartlett processor is noted with a dashed black square.

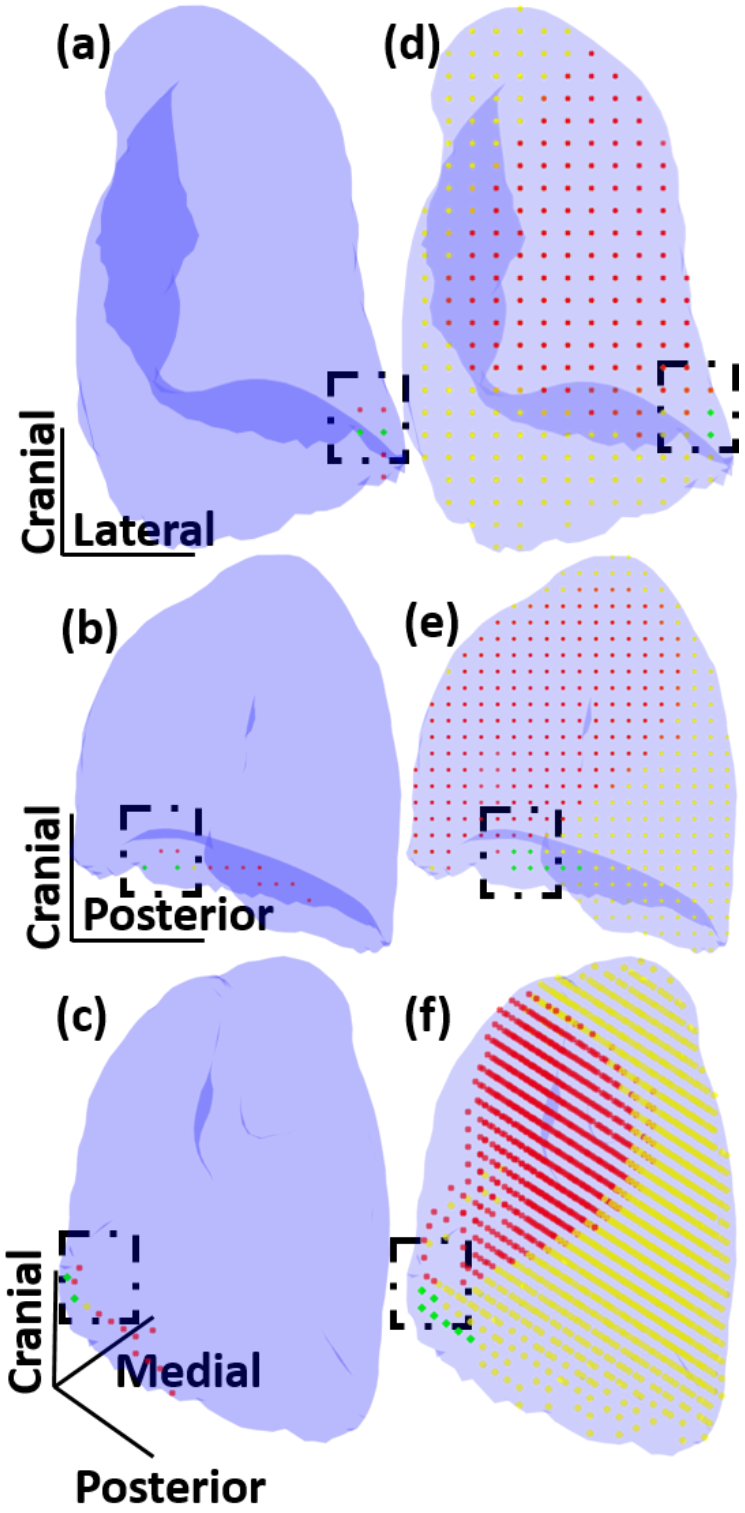

Figure 4.15. Source localization for BE BS (a-c) and incident field BS (d-f) lung at 400 Hz. Left lung shown as a light blue transparent isosurface, with source localizations shown from the thorax front, side, and isometrically. Green, yellow and red dots represent Bartlett confidence regions in the top 10% (>90%), 80-90%, and 70-80%, respectively.

Comparison of wheeze BE and incident field model in localization algorithm at 200 and 400 Hz can be seen in Table 4.4. Results included the full sensor grid and less sensors in the localization algorithm: 3x3 grid place directly over source or 13 cm away cranially, with mean grid spacing of 12.4 mm in small grid and 42.5 mm in large grid.

		Computation Time (Seconds)		Accuracy (mm)	
		Incident Field	BE	Incident Field	BE
With All 6188 BE centroids	200 Hz	2.68	5,330	45.0	2.6
	400 Hz	2.68	5,370	45.0	2.6
Small 3x3 grid near source(9)	200 Hz	0.25	0.23	44.3	9.8
	400 Hz	0.26	0.64	39.1	9.8
Small 3x3 grid far from source(9)	200 Hz	0.23	0.19	107.6	66.6
	400 Hz	0.27	0.25	104.9	126.8
Large 3x3 grid near source(9)	200 Hz	0.24	0.22	143.1	6.0
	400 Hz	0.23	0.22	147.4	6.0
Large 3x3 grid far from source(9)	200 Hz	0.23	0.24	124.5	68.0
	400 Hz	0.23	0.23	124.6	91.5

Table 4.4. Comparison of wheeze BS, BE and incident field model in localization algorithm for wheeze at 200 and 400 Hz, with small (10 mm) or large (42.5 mm) spacing near the source or moved 13 cm cranially (far).

4.5 DISCUSSION

An acoustic boundary element (BE) model of the thoracic cavity including the lung parenchyma, ribcage and chest wall was used to calculate the acoustic field on the left lung surface caused by the distributed sound field within the 3D conducting airway tree, which was approximated using an array of more than 30,000 monopoles, with strength determined though their 1D waveguide calculated radial wall velocities. The BE approach was chosen over a numerical (FE) approach as the it was impractical to create a FE model of the full conducting tree in the left lung, with its multiscale range in terms of radial size of segments. The BE model of the lung surface accounted for mass loading based off of line of sight to the chest wall, including thicknesses creating the mass load based off of bone (ribcage and sternum), the right lung and the torso soft tissue.

It is theorized that the acoustic response calculated on the lung surface, with this mass loading profile may approximate the response on the chest wall, if attenuation is added. Put in context, the response on the lung surfaces account for the other organs in the thoracic cavity per mass loaded profile would match the profile of the velocity on the chest surface, as the sound propagates through the ribcage and intercostal space. However, the sound will attenuate based on the distance to the chest wall. This is an advancement from previous models; historically BE has been limited to simple mass loading based on the chest surface [17]. However, the current model lacks robustness as it should also take into account the effect of rib cage stiffness and damping, not just its mass, as has been done previously [9,14].

In the healthy and fibrotic insonification comparison figure (Fig. 4.5), the fibrotic case exhibited larger velocity amplitudes for 200 and 400 Hz. This can also be seen in Table 4.2. In addition, the larger velocities were more dispersed throughout the lung surface, covering more area. This can be attributed to the larger incident field strength on the lung surface as compared to the healthy case, which reflects the spatially broader acoustic field for the fibrotic case. With stiffer airway walls with fibrosis, more sound energy reaches the smaller airways in the conducting tree, with

the propagating wave energy closer to the parenchymal surface converting to wall radial velocity and ultimately radiating to the lung surface. This can also be seen in Table 4.3, where the fibrotic pathology significantly increased the volume of the predicted airway sources (which was caused by greater dispersion), and also seen in Figure 4.2 where the mean monopole strength per Horsfield order was greater in the fibrotic case.

In the mass-loaded BE simulations for healthy and fibrotic insonification, there is minimal variation on the lung centroid normal velocity based on the material properties (wavenumber) values alone. The more likely explanation is based on the monopole strength of the fibrotic monopoles, seen in Figure 4.2. These differences in BE centroid normal velocities also produced significant differences in source localization. As observed in Fig. 4.11 and quantified in Table 4.3, the Bartlett confidence region, which is an estimate of the location of the sound sources based on their binned categorization, increased in the fibrotic insonification case compared to the healthy insonification case. Generally it is unfavorable to have such a large disperse predicted sound localization volume, as the acoustic source is predicted in a large diffuse volume in the lung, but a larger predicted source volume relative to a baseline healthy subject can itself be an indicator of the disease.

In the wheeze BS case, even with the high number (about 30,000) of segments within the left lung, the sound localization strategy predicted the sound source when coupled with the mass loaded BE calculation of the lung sound field well (see Fig. 4.12 and Table 4.4), to an accuracy of 2.6 mm. This predicted source error of 2.6 mm in the full sensor BE model was consistent at 200, 400 and 800 Hz, and can likely be the result of the relatively coarse grid spacing of 1 cm used in the beamformer algorithm. The incident field assumption the Bartlett beamformer algorithm showed significantly less precision in predicting in estimating the sound source location (minimum error of 6 mm) at all frequencies considered.

Reducing the number of sensor locations used in the beamforming calculations from 6,188 to one in 10 and further to only 9 near the source significantly decreased the computation time to less than a second (comparable to incident field assumption calculation times). Moreover, with BE, when then the 3x3 grid was placed over the sound source, the error was still less than a centimeter, showing that the number of sensors had relatively less impact on the precision of the predicted source location. This is clinically relevant because a 3x3 array of sensors is much more feasible to utilize in a clinical setting. Additionally, per Table IV, while distance of the sensor array from the source location does decrease accuracy, in all cases localization using the BE model outperforms use of the incident field model. One important note to take into further consideration however is that source localization accuracy may worsen when viscoelasiticity of the rib cage is accounted for with coupled models with structural stiffness and damping.

4.6 FUTURE WORK

Insonification models of healthy and fibrotic pathological states, including wheeze BS models with simulated frequencies at 200, 400 or 800 Hz were studied here as a representative example of adventitious respiratory sounds. However, other pathological states and breathsounds including crackles with broadband spectral content could also be analyzed in the same way by identifying prominent frequencies and conducting the analysis on a frequency per frequency basis. Put simply, more studies can be performed to analyze the lung surface response as a result of a number of pathologies and adventitious breathsounds.

In addition, while it may prove difficult, numerical analysis can be performed to compare against analytical solutions of the lung centroid normal velocity. To a degree, this can be done by importing a monopole list into a FEA utility using a FE model of the thoracic cavity excluding the airways. While this has potential, such a numerical FE model would have to include nodes at each monopole location. This means the lung FE volume will be complex, however it would still be less

complex compared to a lung and airway FE model, making numerical simulation and comparison possible but still cumbersome and computationally expensive.

REFERENCES

[1] M. Bahoura, “Pattern recognition methods applied to respiratory sounds classification into normal and wheeze classes,” *Comput. Biol. Med.*, vol. 39, no. 9, pp. 824–843, 2009.

[2] S. Reichert, R. Gass, C. Brandt, and E. Andrès, “Analysis of respiratory sounds: state of the art.,” *Clin. Med. Circ. Respirat. Pulm. Med.*, vol. 2, pp. 45–58, 2008.

[3] P. Piirila and A. R. A. Sovijarvi, “Crackles: Recording, analysis and clinical significance,” *Eur. Respir. J.*, vol. 8, no. 12, pp. 2139–2148, 1995.

[4] A. Bohadana, G. Izbicki, and S. S. Kraman, “Fundamentals of lung auscultation.,” N. *Engl. J. Med.*, vol. 370, no. 8, pp. 744–51, 2014.

[5] Z. Wang, S. Jean, and T. Bartter, “Lung sound analysis in the diagnosis of obstructive airway disease,” *Respiration*, vol. 77, no. 2, pp. 134–138, 2009.

[6] B. A. Reyes, S. Charleston-Villalobos, R. Gonzalez-Camarena, and T. Aljama-Corrales, “Analysis of discontinuous adventitious lung sounds by Hilbert-Huang spectrum.,” *Annu. Int. Conf. IEEE Eng. Med. Biol. Soc.*, vol. 2008, pp. 3620–3, 2008.

[7] H. Pasterkamp, S. S. Kraman, and G. R. Wodicka, “State of the Art Advances Beyond the Stethoscope,” *Am. J. Respir. Crit. Care Med.*, vol. 156, no. 3, pp. 974–987, 1997.

[8] G. Benedetto, F. Dalmasso and R. Spagnolo, “Surface distribution of crackling sounds,” *IEEE Trans. Biomed. Eng.,* vol. 35, pp. 406–12, 1988.

[9] T. Bergstresser, D. Ofengeim, A. Vyshedskiy, J. Shane and R. Murphy, “Sound transmission in the lung as a function of lung volume,” *J. Appl. Physiol.,* vol. 93, pp. 667–74, 2002.

[10] S. Charleston-Villalobos, S. Cortes-Rubiano, R. Gonzalez-Camarena, G. Chi-Lem and T. Aljama-Corrales, “Respiratory acoustic thoracic imaging RATHI: assessing deterministic interpolation techniques,” *Med. Biol. Eng. Comput.*, vol. 42, pp. 618–26, 2004.

[11] R. Paciej, A. Vyshedskiy, J. Shane and R. Murphy, “Transpulmonary speed of sound input into the supraclavicular space,” *J. Appl. Physiol.,* vol. 94, pp. 604–11, 2003.

[12] M. Kompis, H. Pasterkamp and G. R. Wodicka, “Acoustic imaging of the human chest,” *Chest,* vol. 120, pp. 1309–1321, 2001.

[13] B. Henry and T. Royston, "A multiscale analytical model of bronchial airway acoustics," *J. Acoust. Soc. Am.*, vol. 142, no. 4, pp. 1774-1783, 2017.

[14] M. B. Ozer, S. Acikgoz, T. J. Royston, H. A. Mansy and R. H. Sandler, “Boundary element model for simulating sound propagation and source localization within the lungs” *J. Acoust. Soc. Am.*, vol. 122, pp. 657–71, 2007.

[15] T. J. Royston, X. Zhang, H. A. Mansy and R. H. Sandler, “Modeling sound transmission through the pulmonary system and chest with application to diagnosis of a collapsed lung,” *J. Acoust. Soc. Am.*, vol. 111, pp. 1931–46, 2002.

[16] V. Vovk, V. T. Grinchenko and V. N. Oleinik, “Modeling the acoustic properties of the chest and measuring breath sounds,” *Acoust. Phys.,* vol. 41, pp. 667–76, 1995.

[17] G. R. Wodicka, K. N. Stevens, H. L. Golub, E. G. Cravalho and D. C. Shannon, “A model of acoustic transmission in the respiratory system,” *IEEE Trans. Biomed. Eng.,* vol. 36, pp. 925–34, 1989.

[18] T. J. Royston, M. B. Ozer, S. Acikgoz, H. A. Mansy and R. H. Sandler, “Advances in Computational Modeling of Sound Propagation in the Lungs and Torso with Diagnostic Applications,” *Vibration and Acoustics in Biomedical Applications: Imaging, Characterization and Diagnostics.* Chapter 9, pp. 217-248, 2008.

[19] M. A. Biot, “Theory of Propagation of Elastic Waves in a Fluid-Saturated Porous Solid. I. Low-Frequency Range,” *J. Acoust. Soc. Am.*, vol. 28, pp. 168–78, 1956.

[20] M. A. Biot, “Theory of Propagation of Elastic Waves in a Fluid-Saturated Porous Solid. II. Higher Frequency Range,” *J. Acoust. Soc. Am.*, vol. 28, pp. 179–91, 1956.

[21] Z. Dai, Y. Peng, H. Mansy and T. Royston, "Comparison of Poroviscoelastic Models for Sound and Vibration in the Lungs," *J. Vib. Acoust.*, vol. 136, pp. 051012-1 - 051012-11, 2014.

[22] S. Miyawaki, S. Choi, E. Hoffman, and C.-L. Lin, “A 4DCT imaging-based breathing lung model with relative hysteresis,” *J. Comput. Phys.,* vol. 326, pp. 76–90, 2016.

[23] MATLAB, Version 9.0.1 (The MathWorks Inc., Natick, MA, 2016a).

CHAPTER 5

ANIMAL STUDIES, VISUALIZATION APPLICATIONS AND DISSERTATION SUMMARY

5.1 LUNG MODEL GENERATION AND ACOUSTIC SIMULATION OF ANIMAL SUBJECTS

Historically, porcine subjects were used to develop the hybrid segmentation method at the Acoustics and Vibrations Laboratory. Image sets of four healthy porcine subjects were obtained from a CT scanner (Brilliance 64, Philips Electronics) with a voxel resolution of 0.6 x 0.6 x 1 mm. Models of the conducting airway geometries were obtained using they hybrid segmentation method outlined in Section 2.2.1.

Image segmentation was performed in ITK-SNAP version 3.0 [1]. The lung volume was segmented and exported along with the base viewable airway structure, where the airways had high enough contrast to be segmented properly. Seen in Figure 5.1 is the baseline porcine conducting tree model used for further algorithmic generation.

Figure 5.1. Airway image segmentation from porcine subject.

Algorithmic generation was performed in MATLAB 2016a [2]. Before algorithmic generation, the airway segmentation needed to be converted from a volume to a centerline traced bifurcating network with parent daughter connectivity. This was performed in MATLAB via a tracing application written for this purpose. Seen below in Figure 5.2 is a depiction of the interface used.

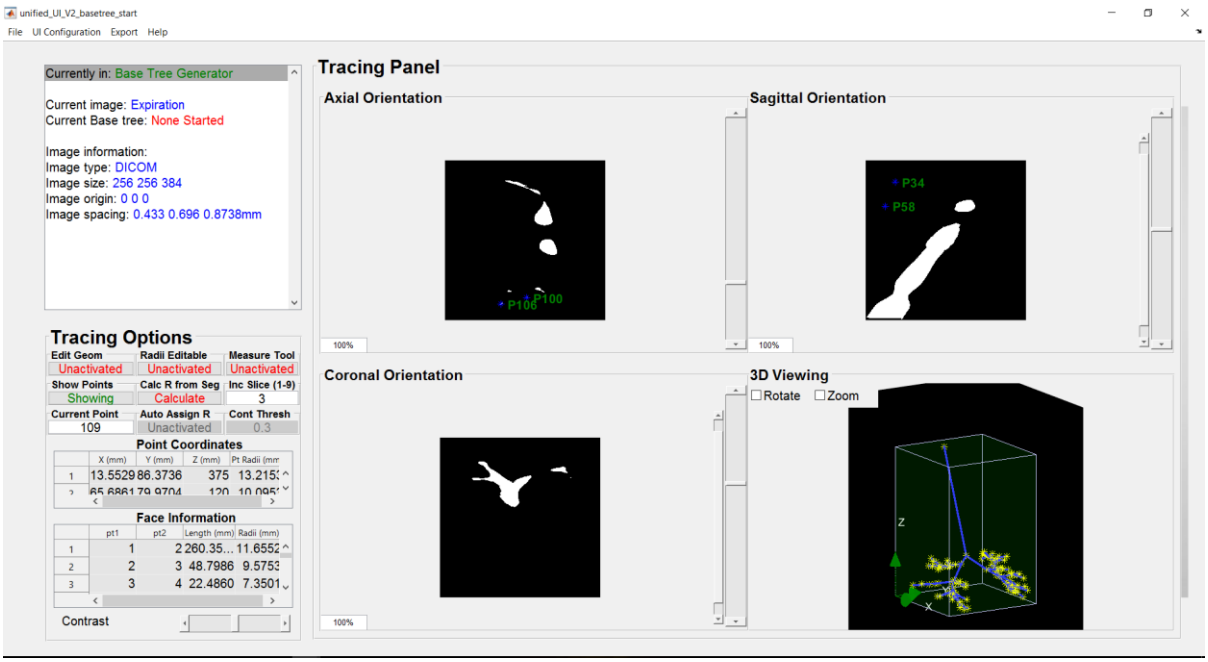

Figure 5.2. UI for the tracing application used to convert airway segmentations to a bifurcating airway network format usable in algorithmic generation.

In the MATLAB interface, the traced bifurcating network is created by tracing the skeleton of the medical image. A medical image is first loaded into the application, which shows up on the axial, coronal and sagittal views seen in Figure 5.2. With the image loaded, a trace can then be created from the trachea to the bronchioles, with the application setting the radius of the segment both automatically (in some cases where the contrast is clear) and manually. When the traced geometry is finished, it is exported into a MATLAB (.mat) format with its radii array, point geometry matrix and face connectivity matrix saved, which can then be loaded and visualized with its host lung volume exported as a STL volume as a lung segmentation. Seen in Figure 5.3 is the STL of the lung volume overlaid over the traced airway skeleton produced via tracing.

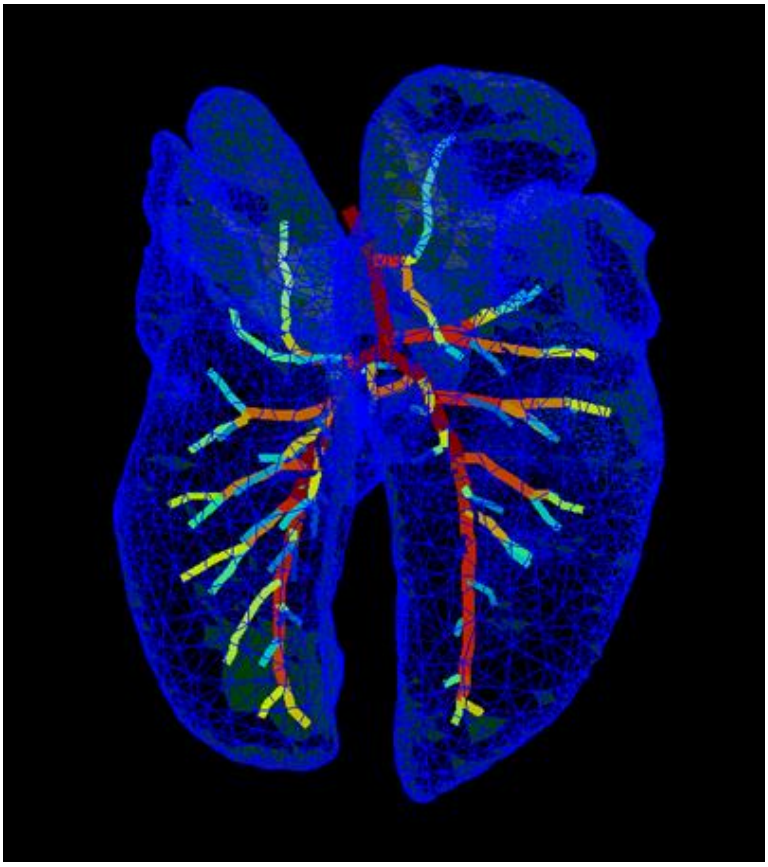

Figure 5.3. Base conducting tree model used for algorithmic generation, colored by its radii, in a blue wireframe lung geometry representing the volume for algorithmic generation.

With the skeletonized airway network and lung volume, algorithmic generation can then be performed to generate the rest of the conducting airways in the porcine lung. Section 2.2.1 details this process. Seen in Figure 5.4 is the full conducting porcine airway network with 3564 airway segments, or with 11 to 12 total generations of airways. In this model, the terminal segments had a mean radius of 2 mm while the trachea had a radius of 1.6 cm, which is physiologically consistent with a porcine tracheal radius.

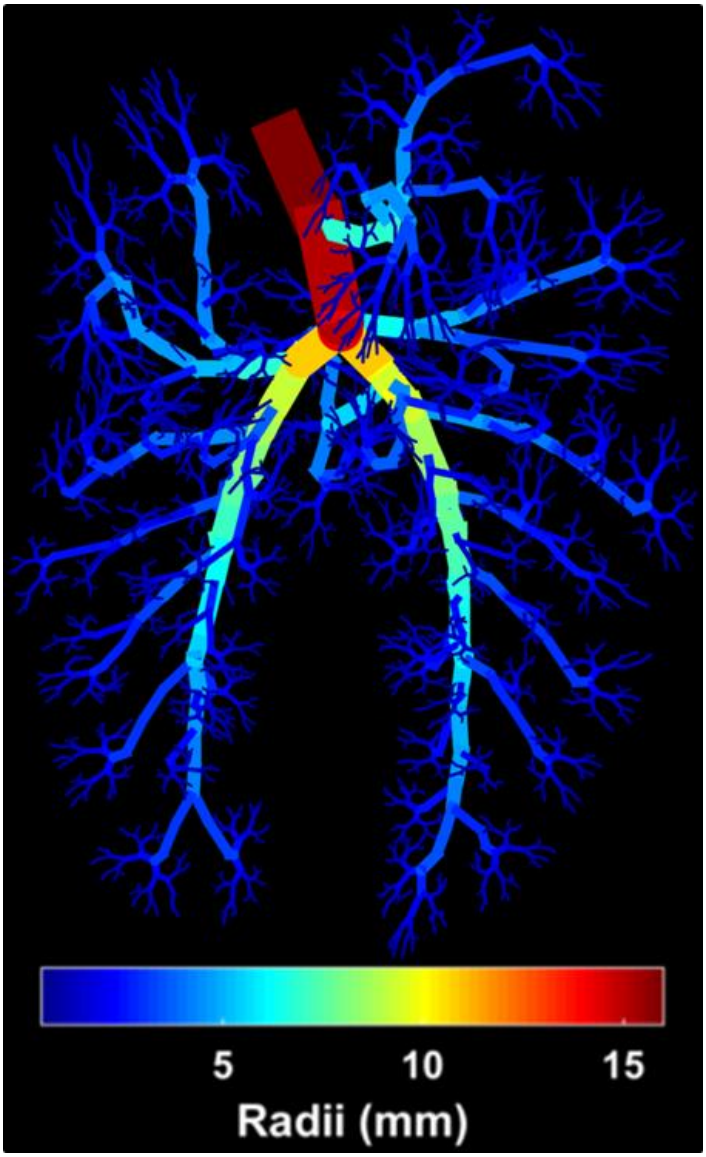

Figure 5.4. Porcine model with algorithmically generated airways on top of base model skeletonized airways.

Additionally, the acoustic pressure and wall velocity in the porcine conducting tree were calculated through use of the 1D modified waveguide per section 2.2.3. The porcine model was insonified through the trachea with a 1 Pa planar sound wave with spectral content from 100 to 800 Hz in 100 Hz increments. In the porcine models, no cartilage fraction was attributed to the airways as no Horsfield model equivalent exists for the porcine lung. Other material properties for

viscoelasticity were taken from Table 2.1. For brevity and for its physiological relevance, results at 400 Hz are shown in Figure 5.5.

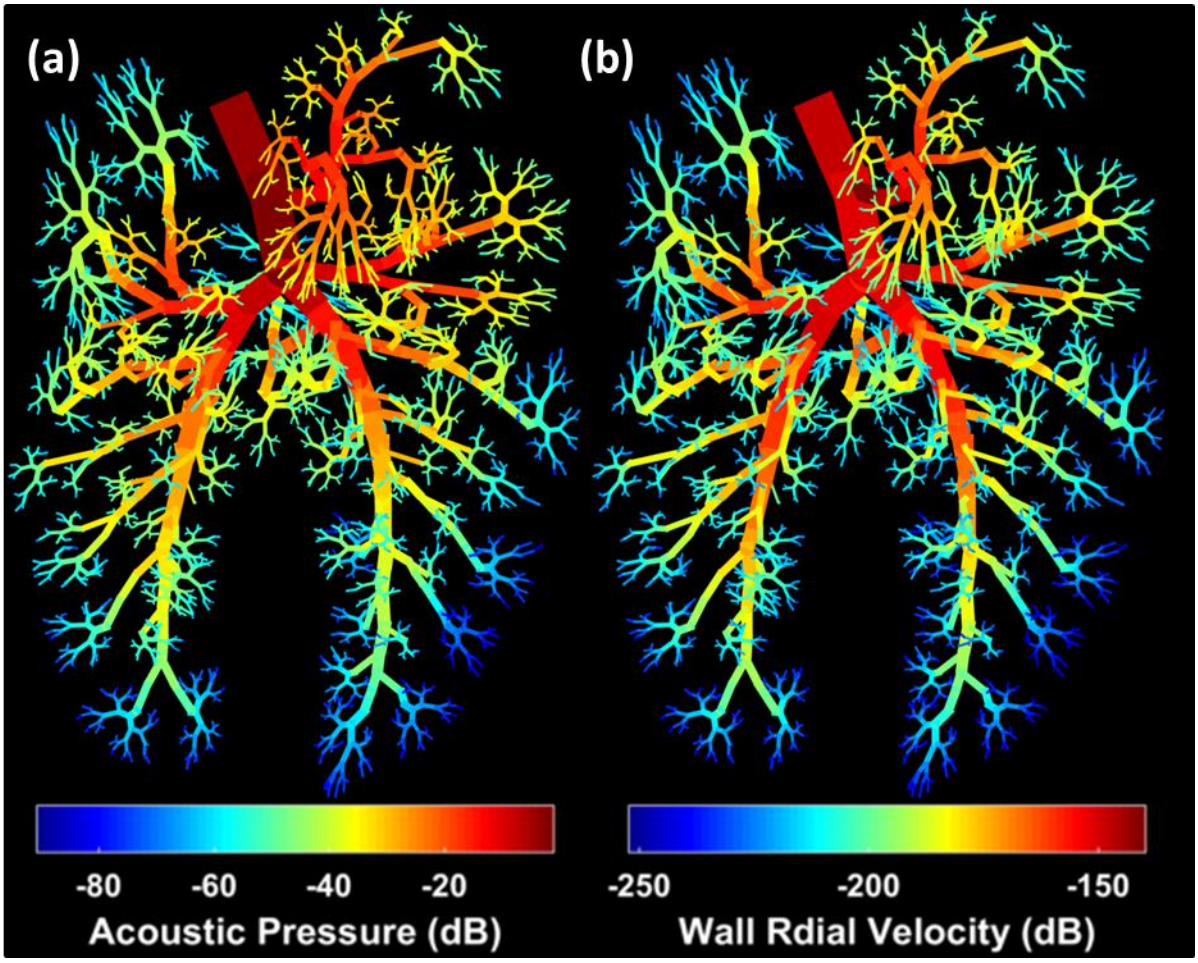

Figure 5.5. (a) Acoustic pressure in dB (ref. 1 Pa) and (b) wall radial velocity in dB (ref. 1 m/s) of porcine tree geometry at 400 Hz.

5.2 AHP VISUALIZATION TOOL

In an effort to better understand complex surface and volume-oriented data given by analytical and numerical models, a tool is needed to make the data more accessible and easily readable. It is difficult to visualize volumetric data on a typical 2D computer screen without an acoustic map to guide users through it. In addition, when acoustic maps have several properties to visualize at once, data storage and access can become a problem. For example, in Chapter 2, there may be

multiple geometry presentations per use of the hybrid generation technique, and when combined with the acoustic outputs of the 1D waveguide (pressure, wall radial velocity) at wide spectral ranges, this can cause large problems associated with too much data available to the user. In addition, interpretation of the data itself may be difficult without knowledge of the acoustic theory.

In this dissertation, the Audible Human Project (AHP) Visualization Tool was developed to streamline the visualization process of waveguide results. Previously, the AHP Visualization Tool was developed to visualize 2D and 3D numerical simulation results, and has more recently been expanded to include 3D airway waveguide results. The AHP Visualization Tool can assist not only with data access, but can also be used for improved education and healthcare purposes. The user menu interface can be seen in Figure 5.6, the user visualization interface for the 2D and 3D numerical datasets can be seen in Figure 5.7 and the current user visualization interface for the 3D airway waveguide datasets can be seen in Figure 5.8.

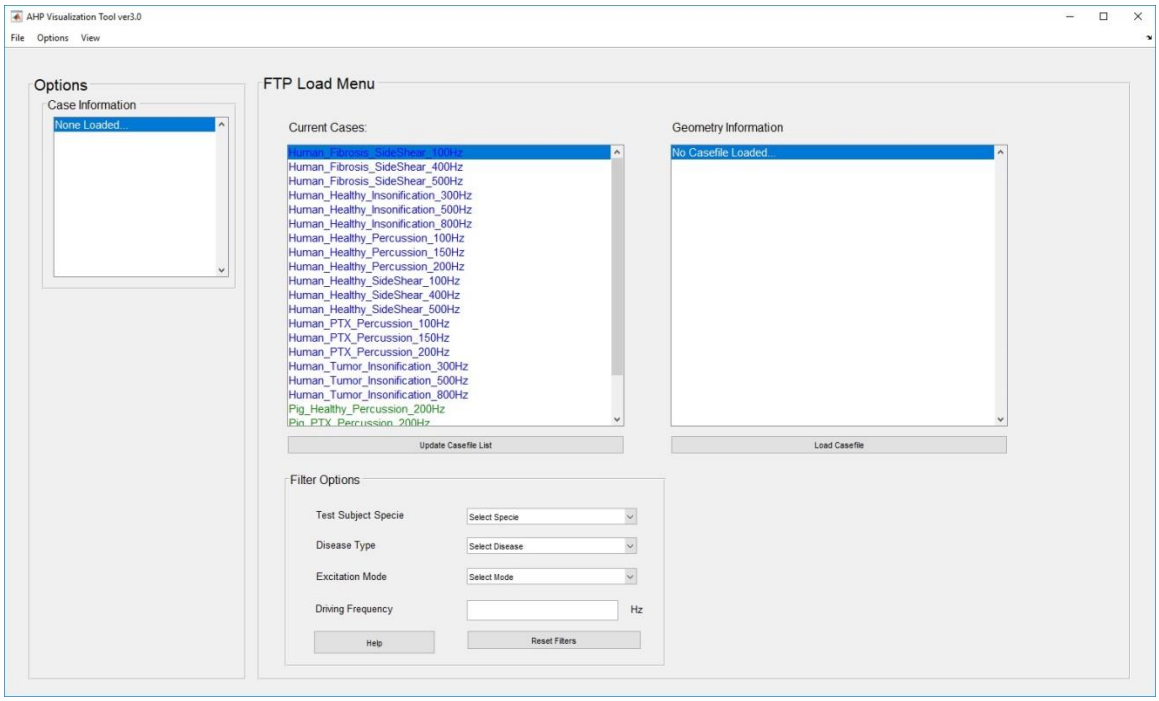

Figure 5.6. AHP Visuzalization Tool main menu. Data is imported from the middle panel, blue files denote human numerical datasets, green represent porcine numerical datasets, and red (not shown below) denote airway waveguide datasets.

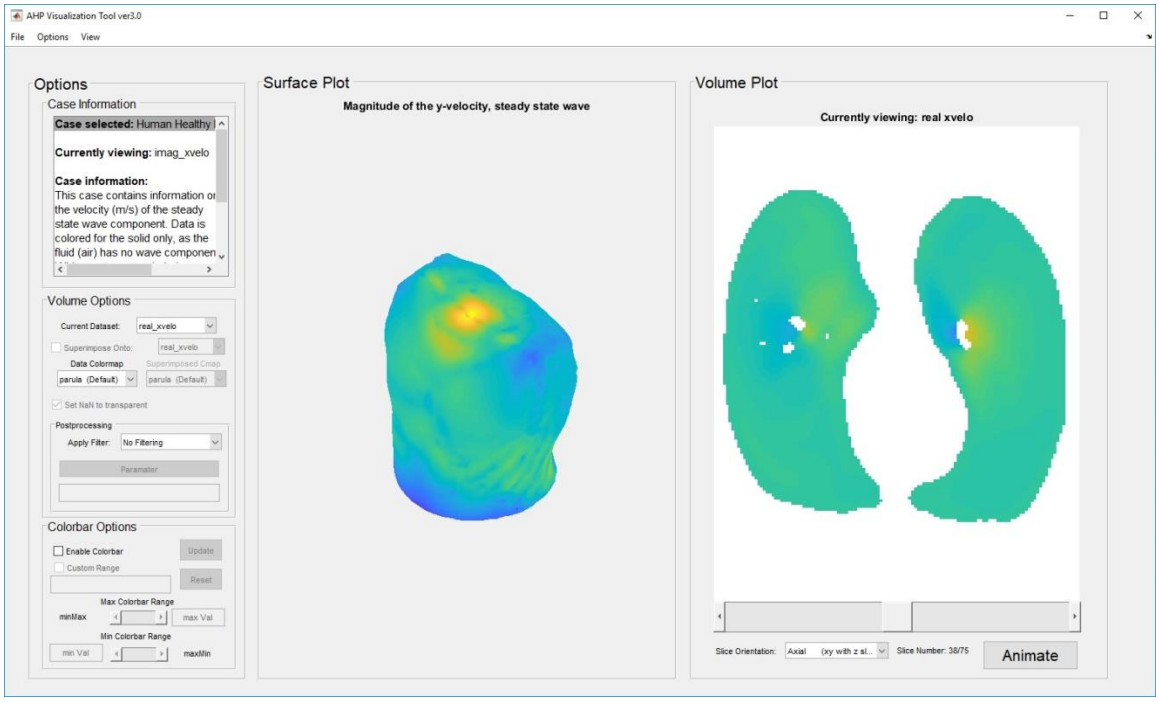

Figure 5.7. AHP Visualization mode for 2D and 3D numerical datasets. Insonification model at 500 Hz is currently shown. Shown to the left is the option panel where visualization settings can be set, the middle shows 2D surface data attributed to the surface, and the right volume plot shows 3D data as a system of axial, coronal or sagittal images. The 3D data sets, being complex acoustical pressure or velocity data, can also be animated from 0 to 2*pi phase.

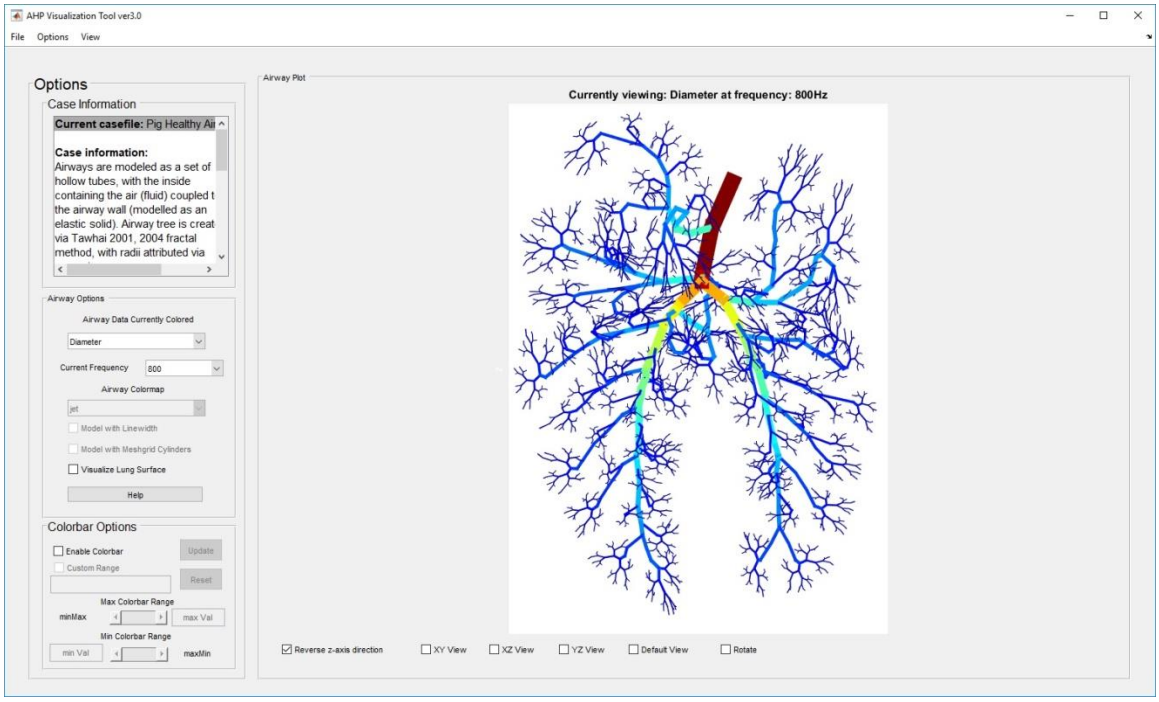

Figure 5.8. AHP Visualization mode for airway waveguide results. Current model is the porcine model shown in Section 5.1. To the left is the options menu, where visualization options can be set. Axes pane in the middle shows the airways with current acoustic variable (for example, acoustic pressure, wall radial velocity, impedances, radii) visualized.

The AHP Visualization Tool works as a file transfer protocol (FTP) client, with cases stored at a server in lab. The numerical and analytical datasets have large file sizes, so the AHP Visualization Tool would be impractical if it was packaged with all case data. In the menu presented in Figure 5.6, the user can pick the cases they want visualized, and they will be downloaded to their computer where they can afterwards view offline without an internet connection. The list of current cases can also be updated in the main menu, as the master list of casefiles is kept server side. As the user updates the list they can visualize the most current list of casefiles.

5.3 SUMMARY

Acoustic modeling of the pulmonary system may provide useful information about lung structure and material composition, and notably how it changes in response to disease or injury. Through

numerous experimental, numerical and analytical studies, lung structural and material changes have resulted in differences in transmitted sounds in pathological models. However, comparatively to the analysis of pulmonary sound measurements, transmission of sound, specifically how it changes in pathological states, has received less attention. A better understanding of sound transmission can lead to more robust diagnostic techniques that can give note not only to disease qualification, but also disese stage and progression.

The Audible Human Project (AHP) is a long-standing project at the Acoustics and Vibrations Laboratory with the aim to develop a series of acoustic models that can accurately measure sound generation, transmission and noninvasive measurement. This dissertation, as a smaller part of the whole AHP, is focused on sound propagation in pulmonary models, from airway networks to the lung surface.

***Airway Modeling via Hybrid Segmentation Method*.** A hybrid image segmentation with algorithmic airway generation was adapted. The ultimate purpose of the hybrid segmentation method is to produce airway conducting trees down to bronchiole level in a physiological relevant manner that can be used for future waveguide studies. These airway models are valuable because some pulmonary disorders have airway specificity. A full conducting tree model may give additional means to model pulmonary disease that up to this point was impossible due to simplistic airway modeling. Additionally, some normal and adventitious respiratory sounds have large differences in the site of generated sound. For example, wheezes and crackles are generated down at the bronchiole level, and require a detailed airway tree to model properly.

Image segmentation of lung CT/MRI imaging is done to create a lung and airway volume, and exported as a volume discretized by triangular surface elements. The airway segmentation is then skeletonized in MATLAB to create a centerline model based on parent-daughter connectivity. This base model of the airways includes airways down to the limit of CT resolution, but does not (typically) incorporate all airways in a conducting tree model. For that reason, an algorithmic

means of generating airways is then applied to grow airways in a physiologically relevant manner to “fill in” the rest of the tree from the physiological accurate backbone generated from CT.

This is done through seeding the lung volume with an evenly spaced grid with a resolution comparable to the size of alveolar respiratory units. The algorithm uses a quasi-volume halving fractal algorithm to grow airways due to the volume filling nature of the airways. The airways are grown iteratively, halving volumes until a terminal bronchiole is reached. The radii for each segment is then attributed based on an order-based law or by power laws based on geometrical properties (length and radius). The algorithm was adapted for use on porcine subjects, and will be used in the future with other animal subjects.

***1D Waveguide Evolution*.** A 1D waveguide was used historically in conjunction with the Horsfield model to solve for acoustic pressure and wall radial velocity. Horsfield models are self-similar in the aspect that they have consistent geometrical properties per order, with an ordered asymmetrical branching at each bifurcation. Human Horsfield trees are ordered from the trachea (n=35) down to the terminal bronchioles which branch into alveolar segments (n = 1). Asymmetry in Horsfield models is given by a delta value, which can vary by Horsfield order, and govern which daughters the parent bifurcates into. Horsfield models also are currently limited to 2D models.

Because of the self-similar structure of the airways, acoustic computation via the 1D waveguide is quick and efficient. Computations are done for 35 orders of segments, for 35 total iterations, acoustically mapping (for a full airway model) millions of segments. Because each order has identical geometrical properties, then one order is calculated, every segment in the tree sharing that Horsfield order is also calculated.

Because of the several limitations and requirements in the Horsfield model and 1D waveguide, it is impractical to use it as-is in a full 3D conducting model. This is due to two reasons: for one a 3D conducting model does not exactly follow self-similarity and has segment-unique geometrical

properties. Secondly, because self-similarity is violated, there is no typical Horsfield ordering of segments, which makes use of the 1D waveguide impossible. For those reasons, a modified 1D waveguide based on parent-daughter connectivity was created for valid use of 1D waveguide analytical analysis on complex 3D conducting airway trees.

Present use of the 1D waveguide requires two inputs: a conducting tree model and a defined frequency range. Material properties, boundary conditions and initial conditions can be specified in the waveguide subfunctions. The modified 1D waveguide outputs both segment-wide acoustic pressures and wall radial velocities in addition to segment-interpolated acoustic pressures and wall radial velocities.

Cases presented in this dissertation were divided into four cases: one healthy case, one fibrotic case incorporating pulmonary fibrosis, one case representing bronchoconstriction of the bronchiole segments and a final fourth case with pulmonary infiltrate. The fibrotic case had an altered material property changing the elasticity of the segments by a factor of five to mimic airway wall stiffening. The bronchoconstriction cases included geometric changes: a narrowing of the inner tubular segment radius and an increase of the outer wall radius to incorporate airway wall narrowing, mucous buildup and airway wall thickening. The pulmonary infiltrate cases have a boundary condition change with the terminal segments in a lobe specified as a hard sound boundary; the terminal impedance of those segments was set to an infinite value. All cases had unique acoustic properties and 1D modified waveguide results provided a quantitative basis for differentiation that can be used in possible modes for diagnosis.

Although currently only three pathological states are modeled, there is room for other lung pathological modeling as the algorithm is adaptive to changes in geometrical, material and boundary condition changes.

Breathsound Modeling. The 3D conducting airway tree geometry and 1D modified waveguide incorporated several changes to accommodate respiratory sound modeling. Previous use of the modified 1D waveguide was limited to tracheal insonification models. Three new simulation modes were added: one for monopole placement at any bifurcation junction, another for placement within an airway segment and a final mode for insonification via a terminal segment. Several respiratory sounds, such as crackles or wheezes, originate in the small airways, which are modeled in this dissertation as sound propagating upwards into the tree via an insonified sound source located at a defined terminal segment. In contrast, other sounds like stridor happen in larger airway segments and propagate both upwards to the mouth and downwards to the bronchioles. To model these breathsounds, both geometrical changes were applied to the model in addition to 1D modified waveguide changes to accommodate these models.

Geometric changes were applied to models to allow for valid use of the 1D BS waveguide. These geometrical changes were associated with switching of the proximal/distal point relationship from the acoustic source upwards to the trachea, to simulate a “downstream” source from the source to the trachea. In the case of monopole placement at a bifurcation junction, three iterations of the 1D BS waveguide were implemented as the full conducting tree was split into two downstream and one upstream trees. During inter-segment monopole placement, one downstream and one upstream tree are created, requiring two iterations of the 1D BS waveguide. In terminal segment insonification, one iteration of the 1D BS waveguide is required with a single upward tree calculation.

A stridor case was theorized as a monopole was placed at a junction distal to the LMB, but was not rigorously tested to check for physiological consistency with the stridor breathsound, but rather as a test to the monopole source mode for introducing sound with the 1D BS waveguide. In addition, wheeze models were introduced as a result of bronchoconstriction and PI disease states, with sound being introduced via insonification from a terminal segment. These cases

included geometry and boundary condition changes consistent with changes due to pathology, and each case relative to a healthy respiratory sound and tracheal insonification cases exhibited unique acoustical information that can be used as a basis for diagnosis.

Acoustic Pulse Time History Reconstruction. Time history reconstruction of the acoustic pulse has relevance in sound localization and estimation of pulse velocities. A crackle case was created by use of impulse response of an estimated transfer function. The crackle FRF was created via implementation of the 1D BS waveguide on a wheeze PI case. The FRF was then fit to a transfer function via the "n4sid" command in the System Identification Toolbox in MATLAB 2016a. Estimation of the transfer function was worse in inlet segments due to difficulty in fitting the FRF due to wide segment variability in resonant peaks and troughs, but as the signal evened out in upstream/downstream segments the fit value increased. The acoustic pulse was then calculated via an impulse response to mimic a crackle's sharp onset. Crackles typically have a 5 ms duration, making an impulse estimate reasonable. Time history of insonification and BS cases yielded information can be useful in future localization strategies.

Boundary Element Method and Incident Field Analysis. A boundary element model including the chest wall, ribcage, sternum, lung and airways was developed. Adaptation of the BE method was done to accommodate current model by dynamically calculating BE acoustical properties as opposed to a hardcoded single model use. Use of BE and incident field analysis allowed for acoustical mapping of the lung surface based on acoustic monopoles placed and with strength determined via 1D waveguide results.

Organs in the thoracic cavity introduced a mass load onto the lung surface. This mass loading was calculated via line of sight from the lung surface centroids up to the chest wall. Intersections up to the lung wall were calculated, and used to determine thicknesses of bone and tissue intersection to the torso surface, which were then used to calculate a mass matrix per element which was incorporated into mass loading BE calculations of the centroid normal surface velocity.

Free field models were similar in all regards except the absence of mass loading, and still incorporated standing wave and reflections in the model. Incident wave calculations still implemented monopole contributions on each surface element via the Green function, but lacked contributions due to reflections and standing waves, although were calculated significantly faster (less than a second) compared to BE models.

Two disease states were investigated: healthy cases, fibrotic cases and bronchoconstriction wheeze cases. The healthy and fibrotic cases were insonified via the trachea and the wheeze case was insonified via a terminal segment mimicking sound generated from a wheeze. All cases yielded unique acoustical maps that can be used as a basis for differentiation. Fibrosis exhibited larger magnitudes of acoustic velocity on the lung surface, and were diffused across larger regions on the lung surface compared to healthy models. Wheeze states by comparison estimated a small localized region with maximum amplitude, with the rest of the lung surface universally low in acoustic velocity on the surface.

Sound Source Localization. Sound localization strategies were adopted to predict the sound sources of BE and incident field simulation results. Hypothetical monopole source grids were created using an evenly spaced 1 cm grid of points which were fit to the lung model. Beamformer equations then used BE gold standard results versus the hypothetical acoustic velocity maps produced using hypothetical monopole sources, cycling iteratively monopole per monopole in the grid of hypothetical sources. This was advanced to be done in parallel, and also done using c++/mex functions to speed up runtime.

Sound localization was performed on BE and incident field simulations. BE simulations across all frequencies and source numbers predicted the acoustic source more accurately for wheeze simulations, but took up to 45 minutes to complete. Incident field calculations still predicted the source to less than a cm from the actual location, but took less than a second.

Smaller grids exhibited larger sources of error based on sensor placement, suggesting that sensor placement is sensitive to prediction results.

Insonification cases exhibited large Bartlett confidence regions. Although typically this is undesirable, having large diffuse regions as predicted sources can be beneficial to a degree as the volume of the predicted source grid can point towards fibrotic states. Fibrosis is associated with a larger Bartlett confidence region across all frequencies, and this is consistent with the larger diffused wall radial velocity across the conducting airway tree with the modified 1D waveguide solution.

5.4 TOPICS FOR FUTURE RESEARCH

***Airway Modeling via Hybrid Segmentation Method*.** Adaptations to the volume halving algorithm to better model small animal subjects can lead to better waveguide analysis to aid dynamic elastographic studies. As a result, further development of the algorithm to qualify airway generation in animal subjects as well as more simulated animal studies are recommended to prove use and usability with dynamic elastographic methods.

***1D Waveguide Analysis and Time History Reconstruction*.** Use of the 1D modified waveguide has been validated with numerical and experimental results. However, use of the 1D modified waveguide is currently limited to fibrotic, bronchoconstriction and PI disease states. Further pathological modeling to qualify pulmonary disease stage and progression is recommended to better act as a possible contributor to future analytical diagnostic methodologies.

This has to be performed on several fronts. For one, experimental or numerical analysis of pathological states can be performed to qualify an algorithm's physiological relevance with pathology. In addition, lung pathophysiology and adventitious respiratory sounds can be further researched to develop more disease states, or model progression of current disease states. The

1D waveguide offers promise as a quick and efficient method to solving acoustical pressures and wall radial velocities quickly and efficiently, but is underutilized in its current state.

***Boundary Element Method and Source Localization*.** Current BE analysis is likewise limited to simple disease cases and relatively coarse geometries. With advances in computer technology, big data computations will become easier and more commonplace, making BE analysis increasingly more feasible on smaller, more mobile computers. Additional pathological states can be investigated along with disease state progression cases to further utilize the BE algorithm so it can be better used as a possible diagnostic aid.

In addition, numerical FE and experimental studies can be performed in parallel to numerical BE studies to validate algorithm accuracy and approach. Currently, the BE method has been validated against previous literature, but has not been compared to actual disease state cases.

Something that is currently neglected in current BE implementation is thoracic cavity organ coupling and organ viscoelasticity. Organ elasticity and damping are neglected. Further studies may be done with FE-accompanied analysis to couple the lung surface to the rest of the organs in the thoracic cavity.

For source localization, higher resolution hypothetical monopole grids can be generated to better predict results. In addition, alternative approaches to the beamformer equation can be utilized to predict the acoustic sources. Current beamformer implementation is best suited for single sources, and with the 1D waveguide introducing 30,000 monopole sources the beamformer implementation comes into question. As predicted, the wheeze BS is predicted more accurately because the sound is rapidly attenuated, which gives an appearance of localized source, making the beamformer approach more suitable for analysis. However, for insonification studies it has its limitations. Alternative algorithmic approaches to localize sound can be investigated that can predict multiple sound sources.

REFERENCES

[1] Yushkevich P, Piven J, et al, “User-guided 3D active contour segmentation of anatomical structures: Significantly improved efficiency and reliability,” *Neuroimage*, vol. 31, no. 3, pp. 1116-28, 2006.

[2] MATLAB, Version 9.0.1 (The MathWorks Inc., Natick, MA, 2016a).

CITED LITERATURE

[1] A. Benade, "On the propagation of sound waves in a cylindrical conduit," *J. Acoust. Soc. Am.*, vol. 44, pp. 616-623, 1968.

[2] A. Bohadana, G. Izbicki, and S. S. Kraman, “Fundamentals of lung auscultation.,” N. *Engl. J. Med.*, vol. 370, no. 8, pp. 744–51, 2014.

[3] A. C. Jackson, J. P. Butler, and R. W. Pyle, Jr., “Acoustic input impedance of excised dog lungs,” *J. Acoust. Soc. Am.,* vol. 64, pp. 1020–1026, 1978.

[4] A. C. Jackson, J. P. Butler, E. J. Millet, F. G. Hoppin, Jr., and S. V. Dawson, “Airway geometry by analysis of acoustic pulse response measurements,” *J. Appl. Physiol..* vol. 43, pp. 523–536, 1977.

[5] A. Cancellieri, G. Dalpiaz, M. Maffessanti, A. Pesci, R. Polverosi, and M. Zompatori, “Cystic diseases,” in Diffuse Lung Disease: Clinical Features, Pathology, HRCT (Springer, New York, 2007), Chap. 6, pp. 202–206.

[6] A. Dubois, A. Brody, D. Lewis, and B. Burgess, Jr., “Oscillation mechanics of lungs and chest in man,” *J. Appl. Physiol.,* vol. 8, pp. 587–594, 1956.

[7] A. Saravazyan, O. Rudenko, S. Swanson, J. Fowlkes and S. Emelianov, "Shear wave elasticity imaging: a new ultrasonic technology of medical diagnostics," Ultrasound in Med. & Biol., vol. 24, pp. 1419-1453, 1998.

[8] A. Siddiqui and S. Ahmed, “Pulmonary manifestations of sickle cell disease,” *Postgrad. Med. J.* vol. 79, pp. 384–390, 2003.

[9] ANSYS ICEM CFD, Version 17.1 (ANSYS Inc., Canonsburg, PA, 2016).

[10] B. A. Reyes, S. Charleston-Villalobos, R. Gonzalez-Camarena, and T. Aljama-Corrales, “Analysis of discontinuous adventitious lung sounds by Hilbert-Huang spectrum.,” *Annu. Int. Conf. IEEE Eng. Med. Biol. Soc.*, vol. 2008, pp. 3620–3, 2008.

[11] B. C. Goss, K. P. McGee, E. C. Ehman, A. Manduca, and R. L. Ehman, “Magnetic resonance elastography of the lung: Technical feasibility,” *Magn. Reson. Med.,* vol.56, pp. 1060–1066, 2006.

[12] B. Henry and T. Royston, "A multiscale analytical model of bronchial airway acoustics," *J. Acoust. Soc. Am.*, vol. 142, no. 4, pp. 1774-1783, 2017.

[13] Bartolucci, P., A. Habibi, M. Khellaf, F. Roudot-Thoraval, G. Melica, A.-S. Lascaux, S. Moutereau, S. Loric, O. Wagner-Ballon, J. Berkenou, A. Santin, M. Michel, B. Renaud, Y. Lévy, F. Galactéros, and B. Godeauc. “Score predicting acute chest syndrome during vaso-occlusive crises in adult sickle-cell disease patients,” *EBioMedicine*., vol. 10, pp. 305–311, 2016.

[14] Brousseau, D. C., P. L. Owens, A. L. Mosso, J. A. Panepinto, and C. A. Steiner. “Acute care utilization and rehospitalizations for sickle cell disease,” *JAMA*., vol. 303, no. 13, pp. 1288-94, 2010.

[15] C. M. Ionescu, P. Segers, and R. De Keyser, “Mechanical properties of the respiratory system derived from morphologic insight,” *IEEE Trans. Biomed. Eng.,* vol. 56, pp. 949–959, 2009.

[16] Castro, O., D. J. Brambilla, B. Thorington, C. A. Reindorf, R. B. Scott, P. Gillette, J. C. Vera, and P. S. Levy. "The acute chest syndrome in sickle cell disease: incidence and risk factors. The Cooperative Study of Sickle Cell Disease,” *Blood*., vol. 84, no. 2, pp. 643-9, 1994.

[17] Charache, S., J. C. Scott, and P. Charache. “Acute chest syndrome in adults with sickle cell anemia. Microbiology, treatment, and prevention,” *Arch Intern Med.*, vol. 139, no. 1, pp. 67-9, 1979.

[18] Cohen, R. T., A. Madadi, M. A. Blinder, M. R. DeBaun, R. C. Strunk, and J. J. Field. “Recurrent, severe wheezing is associated with morbidity and mortality in adults with sickle cell disease,” *Am. J. Hematol.* Vol. 86, no. 9, pp. 756-61, 2011.

[19] COMSOL, Version 5.2a (Comsol Inc., Burlington, MA, 2016).

[20] D. Craiem and R. Armentano, "A fractional derivative model to describe arterial viscoelasticity," *Biorheol.*, vol. 44, pp. 251-263, 2007.

[21] D. Klatt, U. Hamhaber, P. Asbach, J. Braun and I. Sack, "Noninvasive assessment of the rheological behavior of human organs using multigrequency MR elastogrpahy: a study of brain and liver viscoelasticity," *Phys. Med. Biol.*, vol. 52, pp. 7281-7294, 2007.

[22] D. U. Silverthorn, Human Physiology - An integrated approach. 2010.

[23] E. R. Fernandez Perez, C. E. Daniels, D. R. Schroeder, J. St. Sauver, T. E. Hartman, B. J. Bartholmai, E. S. Yi, and J. H. Ryu, “Incidence, prevalence, and clinical course of idiopathic pulmonary fibrosis: A population-based study,” *Chest,* vol. 137, pp. 129–137, 2010.

[24] F. Duck, Physical properties of tissue: a comprehensive reference book, NY: Academic Press, New York, 1990.

[25] F. Liu, J. D. Mih, B. S. Shea, A. T. Kho, A. S. Sharif, A. M. Tager, and D. J. Tschumperlin, “Feedback amplification of fibrosis through matrix stiffening and COX-2 suppression,” *J. Cell. Biol.*, vol. 190, pp. 693–706, 2010.

[26] G. Benedetto, F. Dalmasso and R. Spagnolo, "Surface distribution of crackling sounds," *IEEE Trans. Biomed. Eng.*, vol. 35, pp. 406-412, 1988.

[27] G. R. Wodicka, K. N. Stevens, H. L. Golub, E. G. Cravalho and D. C. Shannon, “A model of acoustic transmission in the respiratory system,” *IEEE Trans. Biomed. Eng.,* vol. 36, pp. 925–34, 1989.

[28] H. Kitaoka, Takaki R and B. Suki, "A three-dimensional model of the human airway tree," *J. Appl. Physiol.,* vol. 87, pp. 2207-2217, 1999.

[29] H. Mansy, R. Balk, W. Warren, T. Royston, Z. Dai, Y. Peng and R. Sandler, "Pneumothorax effects on pulmonary acoustic transmission," *J. Appl. Physiol.,* vol. 119, pp. 250-257, 2015.

[30] H. Pasterkamp, R. Consunji-Araneta, Y. Oh and J. Holbrow, "Chest surface mapping of lung sounds during methacholine challenge," Pediatric Pulmonology, vol. 23, pp. 21-30, 1997.

[31] H. Pasterkamp, S. S. Kraman, and G. R. Wodicka, “State of the Art Advances Beyond the Stethoscope,” *Am. J. Respir. Crit. Care Med.*, vol. 156, no. 3, pp. 974–987, 1997.

[32] Haefeli-Bleuer, B, Weibel, E.R., “Morphometry of the human pulmonary acinus”. *Anat. Rec.*, vol. 220, pp. 401-414, 1988.

[33] J. Fredberg and S. Holford, “Discrete lung sounds: crackles (rales) as stress-relaxation quadrupoles.,” *J. Acoust. Soc. Am.*, vol. 73, pp. 1036–1046, 1983.

[34] Jahani N, Choi S, Choi J, Iyer K, Hoffman E, Lin C-L, “Assessment of Regional Ventilation and Deformation Using 4D-CT Imaging for Healthy Human Lungs during Tidal Breathing”. *J. Appl. Physiol.*. vol. 119, no. 10, pp. 1064-1074, 2015.

[35] K. Horsfield and G. Cumming, "Morphology of the bronchial tree in man," *J. Appl. Physiol.,* vol. 52, pp. 373-83, 1968.

[36] K. Horsfield, W. Kemp and S. Phillips, "An asymmetrical model of the airway of the dog lung," *J. Appl. Physiol.,* vol. 52, pp. 21-26, 1982.

[37] K. Hoyt, T. Kneezel, B. Castaneda and K. Parker, "Quantitative sonoelastography for the in vivo assessment of skeletal muscle viscoelasticity," *Phys. Med. Biol.*, vol. 53, pp. 4063-4080, 2008.

[38] K. Riek, D. Klatt, H. Nuzha, S. Mueller, U. Neumann, I. Sack and J. Braun, "Wide-range dynamic magnetic resonance elastography," *J. Biomech. Eng.*, vol. 44, pp. 1380-1386, 2011.

[39] Knight-Madden, J., and A. Greenough. “Acute pulmonary complications of sickle cell disease,” *Paediatric. Resp. Rev.,* vol. 15, pp. 13–16, 2014.

[40] M. A. Biot, “Theory of Propagation of Elastic Waves in a Fluid-Saturated Porous Solid. I. Low-Frequency Range,” *J. Acoust. Soc. Am.*, vol. 28, pp. 168–78, 1956.

[41] M. A. Biot, “Theory of Propagation of Elastic Waves in a Fluid-Saturated Porous Solid. II. Higher Frequency Range,” *J. Acoust. Soc. Am.*, vol. 28, pp. 179–91, 1956.

[42] M. B. Ozer, S. Acikgoz, T. J. Royston, H. A. Mansy and R. H. Sandler, “Boundary element model for simulating sound propagation and source localization within the lungs” *J. Acoust. Soc. Am.*, vol. 122, pp. 657–71, 2007.

[43] M. Bahoura, “Pattern recognition methods applied to respiratory sounds classification into normal and wheeze classes,” *Comput. Biol. Med.*, vol. 39, no. 9, pp. 824–843, 2009.

[44] M. Kiss, T. Varghese and T. Hall, "Viscoelastic characterization of in vitro canine tissue," *Phys. Med. Biol.*, vol. 49, pp. 4207-4218, 2004.

[45] M. Kompis, H. Pasterkamp and G. R. Wodicka, “Acoustic imaging of the human chest,” *Chest* vol. 120, pp. 1309–1321, 2001.

[46] M. Tawhai, A. Pullan and P. Hunter, "Generation of an anatomically based three-dimensional model of the conducting airways," *Annals of Biomed. Eng.*, vol. 24, pp. 793-802, 2000.

[47] M. Tawhai, P. Hunter, J. Tschirren, J. Reinhardt, G. McLennan and E. Hoffman, "CT-based geometry analysis and finite element models of the human and ovine bronchial tree," *J. Appl. Physiol.,* vol. 97, no. 6, pp. 2310-2321, 2004.

[48] MATLAB, Version 9.0.1 (The MathWorks Inc., Natick, MA, 2016a).

[49] Mekontso Dessap, A., J. F. Deux, A. Habibi, N. Abidi, B. Godeau, S. Adnot, C. Brun-Buisson, A. Rahmouni, F. Galacteros, B. Maitre. “Lung imaging during acute chest syndrome in sickle cell disease: computed tomography patterns and diagnostic accuracy of bedside chest radiograph,” *Thorax*., vol. 69, no. 2, pp. 144-51, 2014.

[50] Morris, C. R. “Asthma management: reinventing the wheel in sickle cell disease,” *Am. J. Hematol.,* vol.84, pp. 234-41, 2009.

[51] P. Forgacs, Lung Sounds. 1978.

[52] P. Piirila and A. R. A. Sovijarvi, “Crackles: Recording, analysis and clinical significance,” *Eur. Respir. J.*, vol. 8, no. 12, pp. 2139–2148, 1995.

[53] Paul, R. N., O. L. Castro, A. Aggarwal, P. A. Oneal. “Acute chest syndrome: sickle cell disease,” *Eur. J. Haematol*., vol. 87, no. 3, pp. 191-207, 2011.

[54] Platt, O. S., D. J. Brambilla, W. F. Rosse, P. F. Milner, O. Castro, M. H. Steinberg, and P. P. Klug. “Mortality in sickle cell disease. Life expectancy and risk factors for early death,” *N. Engl. J. Med*., vol. 330, no. 23, pp. 1639-44, 1994.

[55] Quinn, C. T., Z. R. Rogers, T. L. McCavit, and G. R. Buchanan. “Improved survival of children and adolescents with sickle cell disease,” *Blood,* vol. 115, pp. 3447-3452, 2010.

[56] R. Chan and I. Titze, "Effect of postmortem changes and freezing on the viscoelastic properties of vocal fold tissues," *Ann. Biomed. Eng.*, vol. 31, pp. 482-491, 2003.

[57] R. H. Habib, R. B. Chalker, B. Suki, and A. C. Jackson, “Airway geometry and wall mechanical properties estimated from subglottal input impedance in humans,” *J. Appl. Physiol.,* vol. 77, pp. 441–451, 1994.

[58] R. Habib, B. Suki, J. Bates and A. Jackson, "Serial distribution of airway mechanical properties in dogs: effects of histamine," *J. Appl. Physiol.*, vol. 77, pp. 554-566, 1994.

[59] R. Karch, F. Neumann, M. Neumann and W. Schreiner, "A three-dimensnional model for arterial tree representation, generated by Constrained Constructive Optimization," *Comp. Biol. Med.*, vol. 29, pp. 19-38, 1998.

[60] R. Muthupillai, D. Lomas, P. Rossman, J. Greenleaf, A. Manduca and R. Ehman, "Magnetic resonance elastography by direct visualization of propagating acoustic strain waves," *Science*, vol. 269, pp. 1854-1857, 1995.

[61] R. Paciej, A. Vyshedskiy, J. Shane and R. Murphy, "Transpulmonary speed of sound input into the supraclavicular space," *J. Appl. Physiol.,* vol. 94, pp. 604-611, 2003.

[62] S. A. Taplidou and L. J. Hadjileontiadis, “Wheeze detection based on time-frequency analysis of breath sounds,” *Comput. Biol. Med.*, vol. 37, no. 8, pp. 1073–1083, 2007.

[63] S. Acikgoz, M. B. Ozer, T. J. Royston, H. A. Mansy, and R. H. Sandler, “Experimental and computational models for simulating sound propagation within the lungs,” *ASME J. Vib. Acoust.,* vol. 130, pp. 021010, 2008.

[64] S. Charelston-Villalobos, S. Cortes-Rubiano and R. Gonzalez-Camarena, "Respiratory acoustic thoracic imaging (RATHI): assessing deterministic interpolation techniques," *Med. & Biol. Eng. & Comput.*, vol. 42, pp. 618-626, 2004.

[65] S. Miyawaki, M. Tawhai, E. Hoffman, S. Wenzel, and C.-L. Lin, 2016, “Automatic construction of subject-specific human airway geometry including trifurcations based on a CT-segmented airway skeleton and surface,” *Biomech. Model. Mechanobiol.,* vol. 16, pp. 583–596, 2016.

[66] S. Miyawaki, S. Choi, E. Hoffman, and C.-L. Lin, “A 4DCT imaging-based breathing lung model with relative hysteresis,” *J. Comput. Phys.,* vol. 326, pp. 76–90, 2016.

[67] S. Reichert, R. Gass, C. Brandt, and E. Andrès, “Analysis of respiratory sounds: state of the art.,” *Clin. Med. Circ. Respirat. Pulm. Med.*, vol. 2, pp. 45–58, 2008.

[68] S. Sethi, J. Yin, and P. Anderson, “Lung flute improves symptoms and health status in COPD with chronic bronchitis: A 26 week randomized controlled trial,” *Clin. Transact. Med.* vol. 3, pp. 29, 2014.

[69] S. Yim Yeh and R. Schwartzstein, “Asthma: Pathophysiology and diagnosis,” in Asthma, Health and Society: A Public Health Perspective (Springer, New York, 2010), Chap. 2, pp. 19–42.

[70] Sobota, A., D. A. Graham, M. M. Heeney, E. J. Neufeld. “Corticosteroids for acute chest syndrome in children with sickle cell disease: variation in use and association with length of stay and readmission,” *Am. J. Hematol.* vol. 85, pp. 24–8, 2010.

[71] Strouse, J. J., C. M. Takemoto, J. R. Keefer, G. J. Kato, and J. F. Casella. “Corticosteroids and increased risk of readmission after acute chest syndrome in children with sickle cell disease,” *Pediatr. Blood. Cancer*., vol. 50, pp. 1006–12, 2008.

[72] T. Bergstresser, D. Ofengeim, A. Vyshedskiy, J. Shane and R. Murphy, "Sound transmission in the lung as a function of lung volume," *J. Appl. Physiol.*, vol. 93, pp. 667-674, 2002.

[73] T. Ebihara, N. Venkatesan, R. Tanaka, and M. S. Ludwig, “Changes in extracellular matrix and tissue viscoelasticity in bleomycin-induced lung fibrosis: Temporal aspects,” *Am. J. Respir. Crit. Care Med.,* vol. 162, pp. 1569–1576, 2000.

[74] T. J. Royston, M. B. Ozer, S. Acikgoz, H. A. Mansy and R. H. Sandler, “Advances in Computational Modeling of Sound Propagation in the Lungs and Torso with Diagnostic Applications,” Vibration and Acoustics in Biomedical Applications: Imaging, Characterization and Diagnostics. Chapter 9, pp. 217-248, 2008.

[75] T. J. Royston, X. Zhang, H. A. Mansy and R. H. Sandler, “Modeling sound transmission through the pulmonary system and chest with application to diagnosis of a collapsed lung,” *J. Acoust. Soc. Am.*, vol. 111, pp. 1931–46, 2002.

[76] Taylor, C., F. Carter, J. Poulose, S. Rolle, S. Babu, and S. Crichlow. “Clinical presentation of acute chest syndrome in sickle cell disease,” *Postgrad. Med. J.*, vol. 80, no. 944, pp. 346-9, 2004.

[77] V. Kuperman, “Magnetic resonance imaging: physical principles and applications,” NY: Academic Press, New York, 2000.

[78] V. Vovk, V. T. Grinchenko and V. N. Oleinik, “Modeling the acoustic properties of the chest and measuring breath sounds,” *Acoust. Phys.,* vol. 41, pp. 667–76, 1995.

[79] W. Schreiner , M. Neumann and F. Neumann, "The Branching Angles in computer-generated Optimized Models of Arterial Trees," *J. Gen. Physiol.*, vol. 103, pp. 975-989, 1994.

[80] W. Schreiner, "Computer generation of complex arterial tree models," *J. Biomed. Eng.*, vol. 15, pp. 148-150, 1992.

[81] W. Schreiner, F. Neumann and M. Neumann, "Structural Quantification and Bifurcation Symmetry in Arterial Tree Models generated by Constrained Constructive Optimization," *J. Theor. Biol.*, vol. 180, pp. 161-174, 1995.

[82] Wang, C. Y., Schuermans, D., van Muylem, A., Paiva, M., Noppen, M., Vincken, W., “Bifurcating distributive system using Monte Carlo method”. *Mathl. Comput. Modeling.*, vol. 16, no. 3, pp. 91-98, 1992.

[83] Weatherall, D.J., “The inherited diseases of hemoglobin are an emerging global health burden,” *Blood* vol. 115, no. 22, 4331-6, 2010.

[84] X. Zhang and J. Greenleaf, "Estiamtion of tissue's elasticity with surface wave speed," *J. Acoust. Soc. Am.*, vol. 2007, pp. 2522-2525, 2007.

[85] Y. Fung, Biomechanics: mechanical properties of living tissues, NY: 2nd Ed., Springer-Verlag, New York, 1993.

[86] Y. K. Mariappan, K. J. Glaser, R. D. Hubmayr, A. Manduca, R. L. Ehman, and K. P. McGee, “MR elastography of human lung parenchyma: Technical development, theoretical modeling and in vivo validation,” *J. Magn. Reson. Imag.,* vol. 33, pp. 1351–1361, 2011.

[87] Y. Peng, Z. Dai, H. A. Mansy, B. H. Henry, R. H. Sandler, R. A. Balk, and T. J. Royston, “Sound transmission in porcine thorax through airway insonification,” *Med. Biol. Eng. Comput.*, vol. 54, pp. 675–689, 2015.

[88] Y. Peng, Z. Dai, H. A. Mansy, R. H. Sandler, R. A. Balk, and T. J. Royston, “Sound transmission in the chest under surface excitation: An experimental and computational study with diagnostic applications,” *Med. Biol. Eng. Comput.,* vol. 52, pp. 695–706, 2014.

[89] Y. Yamakoshi, J. Sato and T. Sato, "Ultrasonic imaging of itnernal vibration of soft tissue under forced vibration," *IEEE Trans. Ultrason. Ferroelectr. Freq. Contr.*, vol. 37, pp. 45-53, 1990.

[90] Yushkevich P, Piven J, et al, “User-guided 3D active contour segmentation of anatomical structures: Significantly improved efficiency and reliability,” *Neuroimage*, vol. 31, no. 3, pp. 1116-28, 2006.

[91] Z. Dai, Y. Peng, B. Henry, H. Mansy, R. Sandler and T. Royston, "A comprehensive computational model of sound transmission through the porcine lung," *J. Acoust. Soc. Am.*, vol. 136, pp. 1419-1429, 2014.

[92] Z. Dai, Y. Peng, H. A. Mansy, R. H. Sandler, and T. J. Royston, “Experimental and computational studies of sound transmission in a branching airway network embedded in a compliant viscoelastic medium,” *J. Sound Vib.,* vol. 339, pp. 215–229, 2015.

[93] Z. Dai, Y. Peng, H. Mansy and T. Royston, "Comparison of Poroviscoelastic Models for Sound and Vibration in the Lungs," *J. Vib. Acoust.*, vol. 136, pp. 051012-1 - 051012-11, 2014.

[94] Z. Wang, S. Jean, and T. Bartter, “Lung sound analysis in the diagnosis of obstructive airway disease,” *Respiration*, vol. 77, no. 2, pp. 134–138, 2009.

VITA

NAME: Brian Henry

EDUCATION: University of Illinois at Chicago, Chicago, IL
Doctoral Student of Science in Bioengineering, Graduating Spring 2018

University of Illinois at Chicago, Chicago, IL
Bachelor of Science in Bioengineering, Spring 2011

EXPERIENCE: Research Assistant, Acoustics and Vibrations Laboratory, University of Illinois at Chicago, 2012-2018

Research Assistant, Laboratory for Product and Process Design, University of Illinois at Chicago, 2010-2012

Research Assistant, Department of Pathology, University of Illinois at Chicago, 2009-2010

Teaching Assistant, BIOE 431 – Bioinstrumentation Laboratory, University of Illinois at Chicago, Spring 2014

Teaching Assistant, BIOE 396 – Senior Design 1, University of Illinois at Chicago, Fall 2014

Teaching Assistant, BIOE 396 – Senior Design 2, University of Illinois at Chicago, Spring 2015

Teaching Assistant, BIOE 431 – Bioinstrumentation Laboratory, University of Illinois at Chicago, 2014

Teaching Assistant, BIOE 431 – Bioinstrumentation Laboratory, University of Illinois at Chicago, 2014

HONORS: Recipient of the 2010 Chancellors Student Leadership Award at UIC

1st place ranking at the 2011 Engineering Design Expo

Recipient of the 2016 Graduate Student College Travel Award

PUBLICATIONS: *Archival Journal*

B. Henry and T. Royston, "A multiscale analytical model of bronchial airway acoustics," *J. Acoust. Soc. Am.*, vol. 142, no. 4, pp. 1774-1783, 2017.

B. Henry, G. Yost, R. Molokie and T. Royston, "Early Acoustic Warning for the Onset of Acute Chest Syndrome in Sickle Cell Patients," *ASME,* Accepted for publication, 2018.

B. Henry and T. Royston, "Localization of Adventitious Respiratory Sounds," *J. Acoust. Soc. Am.,* In Review.

Co-authored Archival Journal

I. Gould, T. Marinnan, B. Henry, et al, “Hemodynamics of cerebral micro vasculature,” Computer Aided Chemical Engineering, Elsevier, 2012, Volume 31, Pages 1727-1731

Z. Dai, Y. Peng, B. Henry, H. A. Mansy, and T. J. Royston. “A Comprehensive Computational Model of Sound transmission through the Porcine Lung,” J. Acous. Soc. Am. 136 (3), 1419 - 29 (2014). doi:

10.1121/1.4890647.

Conference Papers and Presentations

2017 IMAG 10th Multiscale Modeling Consortium Meeting, National Institute of Health, Bethesda, MD

Henry, B., Royston, T. (2017). The Multiscale Audible Human Project. 2017 IMAG Conference

2016 International Tissue Elasticity Conference, Fairlee, VT

Henry, B., Royston, T. (2016). The Audible Human Project: Study of Acoustic Transmission with a Fractal Based Model of the Human Airways. 2016 ITEC Conference

2016 Biomedical Engineering Society Annual Meeting, Minneapolis, MN

Henry, B., Royston, T. (2016). The Audible Human Project: Study of Acoustic Transmission with a Fractal Based Model of the Human Airways. 2016 BMES Conference

2016 Student Research Forum, University of Illinois at Chicago, Chicago, Illinois

Henry B, Royston T, (2016). The Audible Human Project: Study of Acoustic Transmission with a Fractal Based Model of the Human Airways. 2016 UIC Research Forum

2014 Society of Photographic Instrumentation Engineers, San Diego, CA

Henry B, Dai Z, Peng Y, Mansy HA, Sandler RH, Royston TJ, "Investigation of Pulmonary Acoustic Simulation: Comparing Airway Model Generation Techniques," in Proceedings of the SPIE Medical Imaging Conference, Paper No. 9038-31 (San Diego, CA, February 16-20, 2014).

2014 SPIE Medical Imaging.

B. Henry, Z. Dai, Y. Peng, H. A. Mansy, R. H. Sandler, T. Royston, "Investigation of pulmonary acoustic simulation: comparing airway model generation techniques," SPIE Proceedings, 2014, Volume 9038, doi:10.1117/12.2043643

2013 Student Research Forum, University of Illinois at Chicago, Chicago, Illinois

Henry, B., Dai, Z., Peng, Y., Royston, T. (2013). An Investigation into the Number of Airway Generations Needed to Accurately Simulate Pulmonary Acoustics. 2013 UIC Research Forum

Affiliated Conferences and Presentations

World Biomechanics Conference 2014, Boston, MA

T. J. Royston, Z. Dai, Y. Peng, S. Kearney, B. Henry, H. A. Mansy, R. A. Balk, R. H. Sandler, "The Audible Human Project: Modeling and Imaging Sound Transmission in the Lungs and How it is Affected by

Injury and Disease," World Biomechanics Conference (Boston, MA, July 6-10, 2014) abstract & presentation.

World Biomechanics Conference 2014, Boston, MA

Y. Peng, Z Dai, B Henry, HA Mansy, RH Sandler, TJ Royston. Modeling sound transmission through the porcine chest. World Biomechanics Conference (Boston, MA, July 6-10, 2014) abstract & poster.

166th Meeting of the Acoustical Society of America 2013, San Francisco, CA

Y. Peng, Z. Dai, B. Henry, H. A. Mansy, T. J. Royston, "A comprehensive computational model of sound transmission through the porcine lung," 166th Meeting of the Acoustical Society of America (San Francisco, CA, December 2 - 6, 2013) abstract.

BMES Annual Meeting 2013, Seattle, WA

Y. Peng, Z. Dai, B. Henry, H. A. Mansy, R. H. Sandler, T. J. Royston, "Modeling and experimental validation of sound transmission in human torso," BMES Annual Meeting (Seattle, WA, Sept. 25 – 28, 2013) poster.

USCAP Meeting 2009, Boston, Massachusetts

Macias V, Henry BM, Hartung GA, Shah JR, NazirT, Balla AK: Transferrin Receptor Expression in a Nested Case-control Prostate

Cancer Cohort. United States Canadian Academy of Pathology 99th Annual Meeting, Boston, Massachusetts, March 20-26, 2010